



저작자표시-비영리-변경금지 2.0 대한민국

이용자는 아래의 조건을 따르는 경우에 한하여 자유롭게

- 이 저작물을 복제, 배포, 전송, 전시, 공연 및 방송할 수 있습니다.

다음과 같은 조건을 따라야 합니다:



저작자표시. 귀하는 원저작자를 표시하여야 합니다.



비영리. 귀하는 이 저작물을 영리 목적으로 이용할 수 없습니다.



변경금지. 귀하는 이 저작물을 개작, 변형 또는 가공할 수 없습니다.

- 귀하는, 이 저작물의 재이용이나 배포의 경우, 이 저작물에 적용된 이용허락조건을 명확하게 나타내어야 합니다.
- 저작권자로부터 별도의 허가를 받으면 이러한 조건들은 적용되지 않습니다.

저작권법에 따른 이용자의 권리는 위의 내용에 의하여 영향을 받지 않습니다.

이것은 [이용허락규약\(Legal Code\)](#)을 이해하기 쉽게 요약한 것입니다.

[Disclaimer](#)

공학박사 학위논문

**Study on Tritium Behaviors in VHTR and  
Forward Osmosis Integration System**

고온가스로의 폐열을 이용한 정삼투 담수화 시스템의  
삼중수소 침투 거동에 대한 연구

2016 년 2 월

서울대학교 대학원  
에너지시스템공학부  
박 민 영

# **Abstract**

## **Study on Tritium Behaviors in VHTR and Forward Osmosis Integration System**

Min Young Park

Department of Energy System Engineering

The Graduate School

Seoul National University

Energy depletion and water scarcity are the two major global issues which are only intensifying due to global population growth. Efforts have been made to tackle the mentioned global issues and as an effective solution to this matter, the integration concept of the Very High Temperature Reactor (VHTR) and Forward Osmosis (FO) desalination is proposed. Through thermodynamic analysis calculations, the suggested VHTR-FO integration system is found to have significantly higher energy utilization rate than the existing nuclear desalination systems.

The VHTR-integrated system has the potential of tritium migration from the VHTR core to the integrated industrial system through permeation in the heat

exchangers. As this is a very serious safety problem, the tritium behavior in the VHTR-integrated system must be analyzed and understood.

In order to understand and analyze tritium behavior in the VHTR-integrated system, the tritium code, Behavior of Tritium Analytic Code (BOTANIC) is developed using a chemical process code, gPROMS. The code involves tritium generation, sorption, leakage, purification, recombination, dissociation, permeation, trapping, release models. It is not only capable of tritium analysis but also chemical process analysis and system dynamics calculation. The developed code is verified using the analytical solutions and the benchmark code in step wise approach.

As the migration mainly occurs through permeation in the heat exchanger, this mechanism is the most important phenomena in understanding tritium behavior. In this study, the printed circuit heat exchanger (PCHE) permeation model is developed which accounts the geometry and thermal distribution across the PCHE wall. The existing permeation model is found to significantly over predict or under predict permeation rate whereas the developed PCHE permeation model is found to accurately calculate permeation rate within  $\pm 20$  %.

There is a lack of permeability data of hydrogen at low temperature region, the integration temperature region of VHTR and FO system. In order to resolve the error accounted with the lack of permeability at low temperature, hydrogen permeation experiment is conducted at low temperature region. Based on the permeability data, the effective permeability is defined and when compared with the permeability data it is found to be in good agreement.

Using the developed BOTANIC code, PCHE permeation model and effective permeability the tritium behavior in the proposed VHTR-FO desalination system

is analyzed. The tritium level in the final water product of VHTR-FO system is found to exceed the regulatory limit an order. This stresses the necessity of tritium mitigation, thus, sensitivity analysis is conducted in order to figure out the effective parameters in reducing tritium level in final product. Based on the sensitivity analysis results, mitigation concepts are suggested and investigated; PHX tritium barrier, PHX material substitution and PHX pre-heat treatment.

**Keywords**

**VHTR, Gas turbine, Forward osmosis desalination, Tritium, Printed Circuit Heat Exchanger, Tritium mitigation, Permeation, Permeability**

**Student Number: 2011-30992**

# List of Contents

<b>Study on Tritium Behaviors in VHTR and Forward Osmosis Integration System</b> .....	<b>i</b>
<b>Abstract</b> .....	<b>ii</b>
<b>List of Contents</b> .....	<b>v</b>
<b>List of Tables</b> .....	<b>viii</b>
<b>List of Figures</b> .....	<b>x</b>
<b>Chapter 1</b> .....	<b>1</b>
<b>Introduction</b> .....	<b>1</b>
1.1 Background and Motivation .....	1
1.1.1 Water Scarcity and Energy Depletion.....	1
1.1.2 Nuclear Desalination Technology.....	2
1.1.3 Tritium Permeation Issue in VHTR .....	4
1.2 Objectives and Scope .....	6
<b>Chapter 2</b> .....	<b>10</b>
<b>Development of Integration concept of VHTR and FO</b> .....	<b>10</b>
2.1 VHTR Power Conversion Systems.....	10
2.1.1 Helium Brayton Cycle .....	11
2.1.2 Supercritical Carbon Dioxide Brayton Cycle.....	12
2.1.3 Waste Heat Conditions for VHTR PCS options .....	13
2.2 Forward Osmosis Desalination .....	14
2.2.1 Overview of Forward osmosis.....	14
2.2.2 Membrane.....	16
2.2.3 Draw solute.....	19
2.2.4 Thermodynamic analysis of FO process .....	21
2.3 Thermodynamic Analysis of the Integrated System .....	24
<b>Chapter 3</b> .....	<b>43</b>
<b>Development and Verification of Behavior of Tritium Analytic Code</b> .....	<b>43</b>
3.1 Tritium Behavior .....	43
3.2 Physical Models .....	44

3.2.1 Conservation Equations .....	44
3.2.2 Tritium Generation.....	44
3.2.3 Tritium Loss .....	46
3.3 Development of BOTANIC .....	50
3.3.1 Code features .....	50
3.3.2 Code Structure .....	52
3.4 Verification of BOTANIC.....	53
3.4.1 Individual model verification .....	53
3.4.2 Total system verification .....	55
<b>Chapter 4 .....</b>	<b>73</b>
<b>Development of Tritium Permeation Model in Printed Circuit Heat Exchanger .....</b>	<b>73</b>
4.1 3-D Tritium Permeation Modelling in PCHE .....	74
4.1.1 Assumptions and Conditions .....	74
4.1.2 Results .....	76
4.2 2-D Numerical Analysis and Parametric Study .....	76
4.2.1 Assumptions and Conditions .....	77
4.2.2 Grid Sensitivity Study.....	77
4.2.3 Parametric Study.....	78
4.2.4 Results.....	79
4.3 Tritium Permeation Model for PCHE .....	82
4.3.1 Shape Factor.....	82
4.3.2 Effective Diffusivity .....	86
4.3.3 Verification of the Developed Model.....	87
<b>Chapter 5 .....</b>	<b>107</b>
<b>Permeability Experiment at Low Temperature.....</b>	<b>107</b>
5.1 Hydrogen Permeation Experiment.....	108
5.1.1 Description of the Hydrogen Permeation Facility (HYPER).....	108
5.1.2 Experimental Procedure.....	108
5.1.3 Uncertainty Analysis.....	110
5.1.4 Effective Permeability.....	111
5.2 Grain Size Effect on Hydrogen Permeation .....	112
5.2.1 Effect of Temperature on Grain Size .....	112
5.2.2 Effect of Grain Size on Permeation .....	113

<b>Chapter 6</b> .....	<b>124</b>
<b>Tritium Analysis of VHTR-FO integrated system</b> .....	<b>124</b>
6.1 Tritium analysis on the proposed VHTR-FO system.....	124
6.2 Sensitivity Study on the VHTR-FO system .....	127
6.2.1 Key parameters .....	127
6.2.2 Results and Discussion.....	127
6.3 Tritium Mitigation Approaches.....	128
6.3.1 Overview .....	128
6.3.2 Evaluation on the suggested mitigation approaches .....	129
<b>Chapter 7</b> .....	<b>144</b>
<b>Summary and Conclusions</b> .....	<b>144</b>
7.1 Summary.....	144
7.2 Recommendations .....	147
<b>Nomenclature</b> .....	<b>149</b>
<b>References</b> .....	<b>155</b>
<b>Appendix A</b> .....	<b>164</b>
<b>BOTANIC Interface</b> .....	<b>164</b>
<b>Appendix B</b> .....	<b>166</b>
<b>Tritium Barrier</b> .....	<b>166</b>
<b>국문 초록</b> .....	<b>172</b>

## List of Tables

Table 1. 1 Nuclear desalination advances.....	8
Table 2. 1 Waste heat conditions for PCS options .....	29
Table 2. 2 Draw solute candidates.....	30
Table 2. 3 Energy data of VHTR helium Brayton and FO integration system.....	30
Table 2. 4 Energy data of VHTR supercritical carbon dioxide Brayton and FO integration system .....	31
Table 3. 1 Comparison of BOTANIC with existing tritium codes.....	57
Table 3. 2 Comparison of BOTANIC with existing tritium codes.....	58
Table 3. 3 Verification case summary.....	59
Table 3. 4 Verification result of ternary fission generation model.....	59
Table 3. 5 Verification result of boron generation model .....	60
Table 3. 6 Verification result of lithium generation model.....	60
Table 3. 7 Verification of helium generation model.....	60
Table 3. 8 Verification result of correlation based permeation model.....	61
Table 3. 9 System verification inputs .....	61
Table 4. 1 Reference geometry dimensions .....	89
Table 4. 2 Conditions of the 3-D COMSOL PCHE permeation model .....	89
Table 4. 3 Grid resolutions used for GCI analysis .....	90
Table 4. 4 Geometric and thermal parameter values for parametric study.....	91
Table 4. 5 Calculated Shape factor 2 values for various v/d and h/d .....	91
Table 5. 1 Previous hydrogen permeation studies.....	115
Table 5. 2 Uncertainties of each parameters .....	115
Table 5. 3 Total uncertainties of permeability data at each temperature .....	116
Table 5. 4 Obtained activation energy and permeability pre-factor.....	116
Table 5. 5 Change in S316L property.....	117
Table 5. 6 Measured grain size after 24 hours of baking at different temperatures .....	117
Table 6. 1 VHTR-FO system base scenario inputs .....	132
Table 6. 2 Heat exchanger design for base scenario .....	133
Table 6. 3 Sensitivity analysis case summary.....	134
Table 6. 4 Results summary of the sensitivity analysis 1 .....	135
Table 6. 5 Results summary of the sensitivity analysis 2 .....	136

Table 6. 6 Tritium reduction factor for S316L coating material .....	137
Table 6. 7 Effect of ceramic heat exchanger (PHX).....	137
Table 6. 8 Comparison of material properties.....	138
Table A. 1 Component models in BOTANIC code.....	165
Table A. 2 Optimization solution compositions.....	171

## List of Figures

Figure 1. 1 Outline of the Study.....	9
Figure 2. 1 Core configurations of PMR 200 .....	32
Figure 2. 2 Schematic of the simulated helium Brayton cycle .....	33
Figure 2. 3 Temperature-entropy diagram for the simulated helium Brayton cycle .....	33
Figure 2. 4 Schematic of the supercritical carbon dioxide Brayton cycle .....	34
Figure 2. 5 Forward Osmosis (FO) and Reverse Osmosis (RO) .....	34
Figure 2. 6 Comparison between RO and FO membranes .....	35
Figure 2. 7 Defined draw solute criteria .....	35
Figure 2. 8 Parametric study on the number of stages (ammonium bicarbonate) ..	36
Figure 2. 9 Comparison on the thermal efficiencies of the three draw solutes.....	36
Figure 2. 10 Schematic of the integration concept of VHTR and forward osmosis desalination system .....	37
Figure 2. 11 Simulated FO-VHTR helium Brayton cycle integrated system on UNISIM.....	38
Figure 2. 12 Simulated FO-VHTR supercritical carbon dioxide integrated system on UNISIM .....	39
Figure 2. 13 Comparison of GORS calculated in FO-helium Brayton system and FO-supercritical carbon dioxide Brayton system.....	40
Figure 2. 14 Comparison of independent and integrated draw solute separation system.....	40
Figure 2. 15 Comparison of GORs of various desalination technologies when integrated with helium Brayton cycle .....	41
Figure 2. 16 Comparison of waste heat utilization rates of various desalination technologies when integrated with helium Brayton cycle.....	41
Figure 2. 17 Comparison of water production of various desalination technologies when integrated with helium Brayton cycle .....	42
Figure 3. 1 Tritium behavior in VHTR system .....	62
Figure 3. 2 Lithium neutron capture reaction mechanism.....	63
Figure 3. 3 Helium neutron capture reaction mechanism.....	63
Figure 3. 4 Boron neutron capture reaction mechanism.....	64
Figure 3. 5 Tritium dissociation and recombination surface mechanisms .....	64
Figure 3. 6 BOTANIC code structure.....	65

Figure 3. 7 BOTANIC verification procedure .....	66
Figure 3. 8 Leakage verification modelling flowsheet on BOTANIC .....	66
Figure 3. 9 Comparison of leakage calculation results of BOTANIC and TPAC..	67
Figure 3. 10 Purification verification modelling flowsheet on BOTANIC .....	67
Figure 3. 11 Comparison of purification calculation result of BOTANIC and analytical solution .....	68
Figure 3. 12 Heat exchanger verification modelling flowsheet on BOTANIC .....	68
Figure 3. 13 Comparison of the computed tritium concentration at the center of the wall .....	69
Figure 3. 14 Tritium concentration across the wall at time 1000 s .....	69
Figure 3. 15 Schematic of the Peach Bottom reactor .....	70
Figure 3. 16 Peach bottom reactor modelling on BOTANIC .....	71
Figure 3. 17 Total system verification result .....	72
Figure 4. 1 Schematic of the PCHE .....	92
Figure 4. 2 PCHE geometry built using CATIA .....	92
Figure 4. 3 Periodic boundaries .....	93
Figure 4. 4 Temperature profile .....	93
Figure 4. 5 Tritium concentration profile .....	94
Figure 4. 6 Tritium permeation route .....	94
Figure 4. 7 Tritium gradient in z, x, and y directions .....	95
Figure 4. 8 Schematic and conditions of the 2-D PCHE model .....	96
Figure 4. 9 Grid size effect on calculation result .....	96
Figure 4. 10 Grid size effect on discretization error .....	97
Figure 4. 11 Geometrical parameters of the PCHE.....	97
Figure 4. 12 Thermal parameters of the PCHE.....	98
Figure 4. 13 Effect of vertical distance (h=0.5) .....	98
Figure 4. 14 Effect of vertical distance (h=1.85) .....	99
Figure 4. 15 Increase of side permeation due to increase of horizontal distance ..	99
Figure 4. 16 Effect of horizontal distance (v=0.5).....	100
Figure 4. 17 Horizontal distance effect on offset .....	100
Figure 4. 18 Effect of horizontal distance (v=1.85) .....	101
Figure 4. 19 Effect of offset (h=0.5) .....	101
Figure 4. 20 Effect of offset (h=1.85).....	102
Figure 4. 21 Result summary of 2-D tritium analysis .....	102
Figure 4. 22 Tritium permeation path.....	103
Figure 4. 23 Elimination of tritium path-2.....	103

Figure 4. 24 Comparison of analytical and numerical solutions ( $S_1$ ).....	104
Figure 4. 25 Fitting of shape factor 2.....	104
Figure 4. 26 Comparison of analytical and numerical solutions ( $S_1$ and $S_2$ ).....	105
Figure 4. 27 Comparison of analytical and numerical solutions (including effective vertical distance).....	105
Figure 4. 28 Final form of the developed PCHE tritium permeation model.....	106
Figure 4. 29 Comparison between the reference solution and the analytical solutions of the existing model and the developed model.....	106
Figure 5. 1 Example of a diffusivity graph.....	118
Figure 5. 2 Overview of HYPER facility.....	118
Figure 5. 3 P&ID of HYPER.....	119
Figure 5. 4 HYPER test section.....	119
Figure 5. 5 Pressure rise rate in the 2 <sup>nd</sup> process volume (0.7t, S316L, 400°C)....	120
Figure 5. 6 Minimum and maximum pressure slopes (0.7t, S316, 200°C ).....	121
Figure 5. 7 Permeability data with error bars.....	122
Figure 5. 8 HYPER permeability data with other permeability data.....	122
Figure 5. 9 Permeability slope transition and effective permeability.....	123
Figure 5. 10 SEM image of electro polished surface of S316L baked at (a) 25 °C (b) 400 °C (c) 1000 °C.....	123
Figure 6. 1 VHTR-FO integration system modelling on BOTANIC.....	139
Figure 6. 2 Tritium concentration in the water product of FO-VHTR.....	139
Figure 6. 3 Tritium pathway in VHTR-FO system (base scenario).....	140
Figure 6. 4 Tritium pathway in VHTR-FO system when using the original permeability (lattice diffusion only).....	140
Figure 6. 5 Effect of sorption area on tritium release rate.....	141
Figure 6. 6 Tritium pathway when sorption area is assumed as 500 m <sup>2</sup> .....	141
Figure 6. 7 Tritium mitigation concepts.....	142
Figure 6. 8 Effect of tritium barrier on tritium concentration in product water...142	
Figure 6. 9 Effect of pre-heat treatment on permeability.....	143
Figure A. 1 BOTANIC code interface.....	164
Figure A. 2 rGO surface morphology, SEM image.....	168
Figure A. 3 rGO side morphology, SEM image.....	168
Figure A. 4 Erbium oxide solutions.....	169
Figure A. 5 Optimization on erbium oxide.....	169
Figure A. 6 Surface morphology of erbium oxide (a) before optimization and (b) after optimization.....	169

Figure A. 7 XRD pattern of erbium oxide coating.....170

# **Chapter 1**

## **Introduction**

### **1.1 Background and Motivation**

#### **1.1.1 Water Scarcity and Energy Depletion**

Energy preservation and water scarcity have now become the main global issues that humanity is facing. According to the recent report, it was found that 1.1 billion people lack access to safe and affordable water for their domestic use (WHO, 2011). Furthermore, currently the dominant energy source, fossil fuel, is a non-renewable energy source with a limited amount of reserves which is running out. And these water shortage and energy depletion are only going to be intensified due to the global population growth, in other words, increasing global demand and pollution.

In order to resolve the global issues, efforts have been made to develop solutions to conserve and preserve water and energy resources. Efforts have been concentrated on researches to improve energy conversion efficiency, discovering other energy sources, development of desalination technologies and enhancement of energy utilization. Progress of these efforts are shown in various fields; discovery of renewable energy sources, improvement in the fossil fuel drilling

technology, combination of cycles, improvement of power conversion cycle efficiency, development of desalination technology, etc.

Combining desalination processes such as Multi Stage Flash (MSF), Multi Effect Distillation (MED) and recently developed Reverse Osmosis (RO) with nuclear power plants have been one of the options to tackle these issues in the recent years. Successful operation experience and active studies on nuclear desalination plants prove the technical feasibility and potential of the process (IAEA, 2007). The feasibility of cogeneration is based on the flexibility of the nuclear power. In other words, using nuclear energy as the energy source for desalination is favored due to the fact that nuclear power can provide both the thermal and electrical energy required by various desalination processes and at the same time, produce additional power in a cost competitive manner. This can be considered as an effective strength but it can also imply loss of potential electricity production as some is taken and used to desalinate seawater instead.

### **1.1.2 Nuclear Desalination Technology**

The concept of integrating desalination technology to nuclear power plant has gained attention due to its cost competitive feature. The feasibility of integrated nuclear desalination plants has been proven with over 150 reactor years of experience in Kazakhstan, India and Japan (IAEA, 2007). The concept of nuclear desalination technology has evolved in terms of energy utilization rate as seen in Table 1.1. Improvement in energy utilization rate was possible due to the concept of integrating VHTR to desalination technology. The concept is effective as it can provide process heat to thermal desalination process without reduction in the

electricity production. This is possible as the VHTR employs a gas turbine cycle. Gas turbine is known for a number of attractive features; low capital cost, compact size, short delivery, high flexibility, fast starting and loading, lower manpower operating needs and better environmental performance (Najjar, 1994). But most importantly it has the cogeneration possibility due to the high quality exhaust gas.

This study introduces a novel conceptual cogeneration system of VHTR and Forward Osmosis (FO) desalination process. The concept is proposed based on the distinctive features of the VHTR and forward osmosis technology. The VHTR produces a relatively high grade waste heat. And forward osmosis desalination concept, which was first suggested in 1965 by Batchelder (Batchelder, 1965) and advanced by McCutcheon et al. (McCutcheon, 2005), uses the natural phenomenon of osmosis. In forward osmosis process the water molecules in the sea water are induced to transport across one side of the membrane to the other by osmotic pressure difference between the sea water and the draw solution. Since the driving force of the FO process depends on the internal property of the solutions the process itself not require any particular temperature or pressure conditions which allows it to require very little energy. This is a fascinating point because other dominant desalination technologies such as multi stage flash, multi effect distillation and reverse osmosis require either high thermal energy or high hydraulic pressure conditions. The only energy intensive part of FO process is the draw solute separation process where draw solute inside the diluted draw solution is separated using an absorption column ( $>60\text{ }^{\circ}\text{C}$ ) (McCutcheon, 2005). And this is where the thermal energy in the exhaust gas from VHTR is used. Additionally, since water scarcity is one of the biggest global issues along with the energy

problem this suggested combined system can be more effective.

The novel integration concept of the two systems, VHTR and forward osmosis desalination system results in an effective cogeneration system. By doing this, useful product, water, can be produced using waste heat which would have been discharged to the environment and potentially caused interruptions in the surrounding ecosystem (Bundela, 2010). Reducing and reusing waste heat have always been an issue, by performing an integration, this issue can be resolved in an effective manner. The concept allows a higher and efficient use of energy. The integrated system carries many advantages based on the distinctive strengths of the two novel technologies; reliable, efficient and relatively clean electricity and water cogeneration system.

### **1.1.3 Tritium Permeation Issue in VHTR**

The novel VHTR-FO integrated system is an effective concept that can produce two useful products; water and energy, efficiently. However there is one potential problem to this concept; tritium. Tritium is a hydrogen isotope with two more neutrons than the typical hydrogen. Due to its structure, it is unstable and thus radioactive. Tritium goes through beta decay and has a half-life of 12.32 years. It typically exists in a hydrogen-tritium (HT) gas form or tritiated water (HTO) form. Tritium is very small and light and has an instinct of easily permeating through solid metals. And this permeability is greatly affected by the temperature. Permeability of tritium increases with increasing temperature and since VHTR operation temperature is relatively high, it is likely that tritium permeation will occur more and faster. Furthermore, since VHTR is integrated to

an industrial process, there is a possibility of tritium permeating through the integration loop and into the industrial process or even into the final product of the industrial process. In other words, due to its high operation temperature and the possibility of the integration to other industrial process, tritium is one of the critical issues associated to the VHTR integration concept in terms of safety, licensing and public acceptance.

Natural occurrence of tritium in the environment is extremely rare. Only  $10^{-16}$  % of the naturally occurring hydrogen is made up of tritium. It goes through beta decay and releases at maximum 18.6 keV of energy during this process. The emitted low energy beta particles can only penetrate about 6.0 mm of air and are unable to penetrate human skin. The low-energy beta particle emitted by tritium has a maximum range in water or tissue of 6 mm, thus, it can be said as non-hazardous externally (Glasstone & Jordan, 1980). However, beta radiation is a type of ionizing radiation which can cause cell damage and further cause cancer or genetic disorder when exposed inside the body. Given its low energy beta emission and the short range in air, tritium poses a health risk only when ingested, inhaled or absorbed through skin. The biological half-life of tritium depends on the form and the method of intake. Only about 0.004 percent of inhaled tritium gas is retained more than a minute or so, the rest is eliminated almost immediately through respiration (Fairlie, 2007). When tritium is ingested in tritiated water form it immediately mixes with the body fluids and has a half-life of 10 days. And as tritiated water act as water in the body, tritium is distributed through all biological fluids within 1 to 2 hours. In other words, tritium is hazardous when ingested in the body. And as a result, regulatory limits have been set for tritium in drinking water. The EPA standard for drinking water is set as  $2 \times 10^{-5}$   $\mu\text{Ci/mL}$  (EPA,

1976b). Thus, tritium must be treated more seriously in the suggested integration system as the product of the VHTR-FO is drinking water.

Therefore, it is crucial to analyze and understand tritium behavior in the VHTR and industrial process integrated to the VHTR. It is especially important to understand the permeation behavior as it is the main route of tritium migration to the downstream processes. Thus in order to perform a complete analysis on tritium behavior in the integration system, following studies are essential; (1) development of a tool for tritium analysis in the VHTR-FO integrated system (2) development of tritium permeation model in the Printed Circuit Heat Exchanger (3) acquisition of tritium permeation data at the integration temperature condition; low temperature condition.

## **1.2 Objectives and Scope**

The main objectives of this study is (1) to develop a novel integration system of VHTR and FO desalination system, (2) to develop a methodology for tritium analysis and (3) to analyze the tritium behavior in the suggested integration system and propose tritium mitigation approaches. The integration concept of VHTR and FO desalination system is suggested and developed by conducting the feasibility study through thermodynamic analysis using UNISIM code and OLI property package. The integration system is simulated and the feasibility is proved by comparing the efficiency of the suggested system with that of the conventional nuclear desalination system. In order to analyze tritium behavior in the VHTR-FO integrated system, which is the one of the critical issues in the VHTR integrated

system, following are developed in this study; (1) tritium analysis code, (2) tritium permeation model in PCHE and (3) modified effective permeability for low temperature region. And using the developed tools, tritium behavior in the VHTR-FO system is analyzed. And according tritium mitigation approaches have been suggested. The overview of the scope is illustrated in Figure 1.1.

The thesis is composed according to the outline of the study. Chapter 2 presents the integration concept of VHTR and FO desalination system, including the feasibility study on the developed integration system. In Chapter 3, the development and verification of the BOTANIC code is described. The development of tritium permeation model in PCHE is covered in Chapter 4. The following chapter, Chapter 5, explains the permeability experiment conducted at low temperature. The tritium analysis on VHTR-FO integrated system, using the developed tritium code, permeation model and the effective permeability, is explained with the mitigation concepts in Chapter 6.

Table 1. 1 Nuclear desalination advances (IAEA, 2007)

<b>Desalination technology</b>	<b>LWR-Multi Stage Flash (MSF)</b>	<b>LWR-Multi Effect Distillation (MED)</b>	<b>LWR-Reverse Osmosis (RO)</b>	<b>VHTR-Multi Stage Flash (MSF)</b>	<b>VHTR-Multi Effect Distillation (MED)</b>	<b>VHTR-Forward Osmosis (FO)</b>
Electricity consumption [kWh/m <sup>3</sup> ]	3.5	1.5	6	3.5	1.5	0.84
Thermal energy consumption [kWh/m <sup>3</sup> ]	25-200	25-200	0	25-200	25-200	26-150
Top brine temperature [°C]	110	65	N/A	110	65	N/A
Energy utilization rate [%]	33.0	33.0	33.0	51.1	76.8	89.6
Disadvantage	Energy intensive (thermal)	Energy intensive (thermal)	Low quality product	Energy intensive (thermal)	Energy intensive (thermal)	Requires post-process: draw solute recovery process

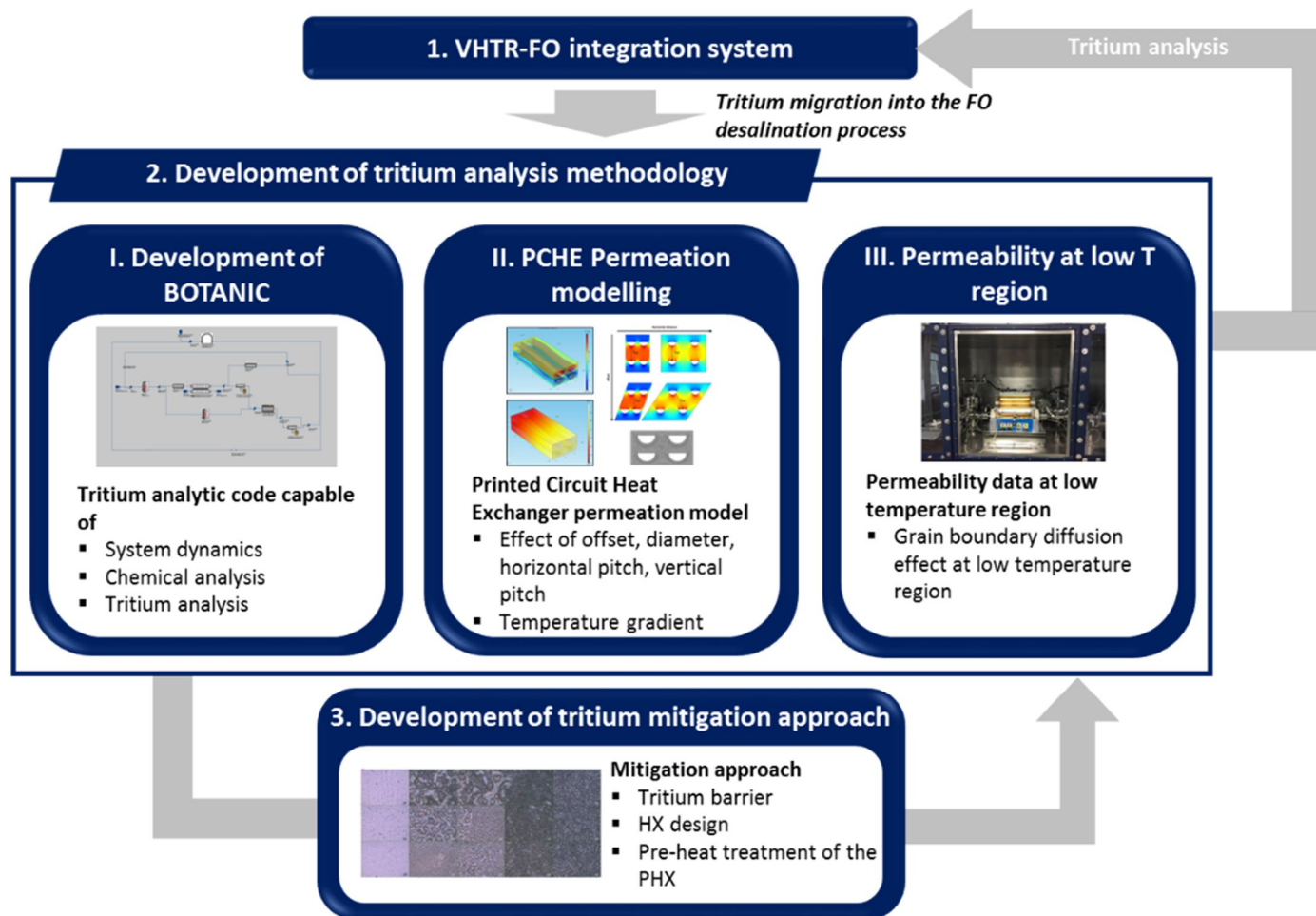


Figure 1. 1 Outline of the Study

## **Chapter 2**

# **Development of Integration concept of VHTR and FO**

### **2.1 VHTR Power Conversion Systems**

The Very High Temperature Reactor (VHTR) is one of the most promising next generation nuclear reactor concepts suggested. VHTR is a graphite moderated, gas-cooled reactor with a once through uranium fuel cycle. It employs a direct or indirect gas Brayton cycle to convert heat into electrical energy. The key virtues of this reactor type are the inherent passive safety features and high efficiency. The high efficiency is achieved by the employment of gas turbine and high temperature operation; 900 °C and 8.5 MPa. The VHTR typically employs a direct or indirect Brayton cycle over the conventional steam Rankine cycle for high thermodynamic efficiency and simplicity. This leads to economical and safety benefits.

In order to estimate the waste heat conditions of the VHTR, the reference design of PMR200 was used. PMR200 is a UO<sub>2</sub> fuelled prismatic VHTR core, one of the candidates developed for the NHDD project in South Korea (Chang, 2007). It has an annular core, composed of 66 fuel columns. Each column is composed of

six fuel blocks stacked axially. The core is enclosed by graphite reflectors. The dimensions of PMR200 fuel block are practically the same as the GT-MHR fuel block (Kodochigov, 2003). The core configuration of PMR200 is depicted in Figure 2.1.

This study considered two potential power conversion systems (PCS) for the VHTR, in which thermal energy is converted to electrical energy with discharging wasted heat; (1) helium Brayton cycle and (2) supercritical carbon dioxide Brayton cycle. The following sections summarize the results for thermodynamic analysis of optimized PCS and waste heat conditions.

### **2.1.1 Helium Brayton Cycle**

In this study, the VHTR helium Brayton cycle in the secondary power conversion system was modelled using UNISIM (UNISIM design, 2010). The tool used, Honeywell's UNISIM Design Suite, is a process modelling software that enables steady-state and dynamic process calculations. The property calculations are done based on the Peng-Robinson equation of state. It is an often recommended property package as it is relatively reliable, efficient, accurate and covers a wide range of conditions (UNISIM design, 2010). Figure 2.2 shows the system configuration and estimated operating conditions for the major flow streams. The cycle, based on a 200 MW thermal reactor using helium as coolant for primary and secondary sides of the VHTR, is calculated to have an optimized efficiency of 42.4 %. The simulated cycle consists of a single stage expansion and 2 stage polytropic compression. The temperature-entropy (T-S) diagram representation of the simulated helium Brayton cycle is depicted in Figure 2.3.

The reactor and Brayton cycle were coupled using an intermediate heat exchanger (IHX). In the primary system, the helium was heated up to 900 °C and compressed up to 7.89 MPa by the primary circulator. Heat in the primary side is exchanged through IHX. The IHX secondary side outlet enters the gas turbine. Outlet of the gas turbine enters a recuperator give off heat to the compressor outlet. The helium is then cooled and compressed sequentially twice each. This sequence of cooling and compressing results in two waste heat streams. The coolant then enters IHX for heat recovery. The helium exits the coolers at 30 °C. Pressure drops of 0.13 MPa for IHX and 0.10 MPa for recuperator were assumed and 0.04 MPa for coolers. The cycle was optimized to maximize its overall plant cycle efficiency by adjusting core inlet temperature, turbine outlet pressure, recuperator outlet temperature, compressor outlet pressure and etc. The efficiency of the power conversion system was calculated by the following equation.

$$\eta_{overall} = \frac{W_{turbine} - W_{compressor}}{Q_{reactor}} \quad (2.1)$$

### 2.1.2 Supercritical Carbon Dioxide Brayton Cycle

Supercritical carbon dioxide Brayton cycle is one of the alternative candidates for the helium Brayton cycle in the VHTR. Due to supercritical properties of the coolant, attractive efficiencies can be achieved at a lower temperature, and this has gained attention. This is possible as the compression work is significantly reduced because of the supercritical properties of the coolant (Feher, 2010) (Dostal, 2004), (Kato, 2002). This feature results in high thermodynamic efficiency under lower operating temperatures.

In this study, the VHTR supercritical carbon dioxide recompression Brayton cycle was modelled using UNISIM for thermodynamic analysis of integrated FO desalination system. Figure 2.4 shows the system conditions calculated for the VHTR supercritical carbon dioxide Brayton cycle. Reactor outlet of 750 °C and reactor power of 200 MWt was given. Maximum pressure in the cycle was 20 MPa (Harvego &McKellar). Polytrophic efficiency of turbine was assumed as 90 %. Pressure drops of 0.02 MPa were assumed for tube and shell side of heat exchanger and 0.02 MPa for cooler. The maximum overall plant efficiency was calculated to be 48.2 % for the given constraint.

### **2.1.3 Waste Heat Conditions for VHTR PCS options**

Based on the modelling in the previous sections, the waste heat conditions for the VHTR PCSs are calculated as shown in Table 2.1. The waste heat conditions and efficiency of a typical nuclear reactor Rankine cycle are displayed in the table as well for comparison. The waste stream energy flow of the Rankine cycle is the normalized value for 200MWt reactor.

As can be seen in Table 2.1, the waste heat stream temperatures in VHTR are notably higher than that of a general PWR. When comparing the waste heat stream conditions of helium and supercritical carbon dioxide cycles, it was discovered that the helium waste heat streams carry higher temperature than supercritical CO<sub>2</sub> heat stream. And as the efficiency is higher in supercritical carbon dioxide Brayton cycle than in helium Brayton cycle, the total amount of energy discharged through waste heat in helium Brayton cycle is larger than that in supercritical carbon dioxide Brayton cycle. The temperature of the waste heat stream produced in the water Rankine cycle is around 69.2 °C, which is too low

for heat recycle. Although this obstacle could have been overcome by turbine bleeding, it has not been covered in this paper.

## **2.2 Forward Osmosis Desalination**

### **2.2.1 Overview of Forward osmosis**

Forward osmosis is an emerging technology that can produce fresh water by desalinating saline water sources. It is a membrane oriented desalination technology just like reverse osmosis, which is one of the dominant desalination technology nowadays. And unlike conventional desalination technologies, these two membrane associated technologies do not require intense thermal energy due to the nature of osmosis. In osmosis, the water molecules are transported across a semi permeable membrane that is impermeable to salt. The transportation is driven by the concentration gradient across the semi-permeable membrane. In forward osmosis, the concentration difference is built using the draw solution that has a significantly higher osmotic pressure than the saline feed water as shown in Figure 2.5. Unlike FO process, the reverse osmosis, currently the leading desalination process uses hydraulic pressure instead of osmotic pressure as a driving force. When the hydraulic pressure difference is larger than the osmotic pressure difference between the saline and pure water, the water molecules are forced out of the saline feed water through the semi-permeable membrane.

This feature of forward osmosis process has gained attention since no significant thermal nor hydraulic energy is required as the process is operated based on the natural phenomenon, osmosis. In other words, the process can be

operated near ambient pressure and temperature. Thus, FO delivers many potential advantages such as less energy consumption, lower fouling tendency, easier fouling removal and higher water recovery (McCutcheon, 2005) compared to reverse osmosis.

In theory, higher water flux, when compared to reverse osmosis, can be achieved according to the water flux equation expressed as

$$J_w = A_w \delta (\Delta\pi) \quad (2.2)$$

for flow across a semi-permeable membrane. Reflection coefficient,  $\delta$ , can be determined by taking the ratio of the experimental water flux and the predicted water flux. It approaches 1.0 for a completely salt rejecting membrane (McCutcheon & Elimelech, 2007). In theory, it is usually assumed as unity. Thus, the water flux,  $J_w$ , is mainly dependent on the water permeability coefficient ( $A_w$ ) and the osmotic pressure difference between the draw solution and feed solution ( $\Delta\pi$ ). Whereas in reverse osmosis water flux equation, osmotic pressure difference is replaced by the hydraulic pressure difference subtracted by the osmotic pressure difference of the saline and draw solutions ( $\Delta P - \Delta\pi$ ). And as it is easier to achieve higher osmotic pressure difference than hydraulic pressure difference, it can be said that higher water flux can be attained in forward osmosis than reverse osmosis.

Despite the advantages of forward osmosis, active development and studies occurred just recently, which is quite a while from the first suggestion in the 1960s. As mentioned earlier the performance of forward osmosis depends on the osmotic pressure difference of the feed and draw solutions ( $\Delta\pi$ ) and the water permeability ( $A_w$ ). Consequently, the studies have been focused on these two aspects; draw solution and membrane development. The osmotic pressure difference between

the draw solution and feed solution ( $\Delta\pi$ ) is the driving force of the osmosis process. Since the osmotic pressure of the saline feed water is more or less constant, it is the osmotic pressure of the draw solution which governs the water flux when the membrane type used in the process is controlled. The water permeability ( $A_w$ ) is a measure of the ease of water transport across the semi-permeable membrane. It is dependent on the membrane characteristics such as membrane thickness, partition coefficient of water into the membrane and diffusivity of water, where water transport across the membrane is governed by the solution diffusion mechanisms (McCutcheon & Elimelech, 2007). Therefore, development of the ideal draw solution and membrane are the two most crucial tasks that need to be resolved in order to commercialize FO in the field of desalination along with other arising issues such as fouling and concentration polarization.

### **2.2.2 Membrane**

In reality, the water flux of FO process is greatly influenced by the membrane structure. To be more explicit, the process is influenced by two kinds of concentration polarization which is caused by membrane structure; internal concentration polarization and external concentration polarization. This is because currently most of the commercially available membranes are designed for pressure driven membrane processes. As the mechanism of the FO process is quite different from that of RO, the development of different type of membrane focusing on slightly different function is indispensable. The difference in the FO and RO membranes mainly lies in the structure as in Figure 2.6. Membrane

designed for pressure driven processes typically contains a very thin dense active layer (less than 1  $\mu\text{m}$ ) which rejects unwanted salt and is supported by a microporous support layer, and this is further supported by a very thick porous fabric layer which mechanically supports the asymmetry membrane layer. The porous fabric layer has to be thick enough to withstand the hydraulic pressure required for the RO operation. Typical thickness of a RO membrane is over 100  $\mu\text{m}$  (NG, 2006). This asymmetric thick porous structure membrane does not cause any crucial problems in pressure driven processes. But in the case of the osmotic pressure driven process, this thick porous layer is responsible for the development of internal concentration polarization which causes reduction of the water flux by more than 80 % (Gray, 2006).

Concentration polarization (CP) is one of the largest challenges in membrane processes. There are two types of CPs; external concentration polarization (ECP) and internal concentration polarization (ICP). External concentration polarization occurs both in pressure driven and osmotic driven processes but unlike internal concentration polarization, it can be mitigated by increasing the flow turbulence or velocity (Gray, 2006). Critical problem lies in the internal concentration polarization. Internal concentration polarization occurs only in osmotically driven membrane processes. It cannot be mitigated by external efforts as it is mainly caused by the porous asymmetric membrane structure.

Many efforts have been made to model the effects of ECP and ICP on water flux in FO process. A more detailed water flux model which accounts the ICP effect, ECP effect and membrane characteristic properties can be shown in equation 2.3 (Shaffer, 2015). The model is expressed using the membrane characteristic properties, the hydrodynamics in the membrane flow cell and

experimentally accessible parameters such as concentrations and osmotic pressures:

$$J_w = A_w \frac{\pi_D \exp\left(-\frac{J_w \cdot S_w}{D_w}\right) - \pi_F \exp\left(-\frac{J_w}{k_w}\right)}{1 + \frac{B_w}{J_w} \left[ \exp\left(-\frac{J_w}{k_w}\right) - \exp\left(-\frac{J_w \cdot S_w}{D_w}\right) \right]} \quad (2.3)$$

where  $k_w$  is the mass transfer coefficient of the feed and  $D_w$  is the bulk diffusion coefficient of the draw salt. The water permeability coefficient,  $A_w$ , and salt permeability coefficient,  $B_w$ , describe the transport across the membrane active layer. The structural parameter,  $S_w$ , quantify the mass transport length scale across the membrane support layer. The support layer structural parameter,  $S_w$ , is defined as below (Alsvik, 2013)

$$S_w = \frac{x_{mem} \cdot \tau}{\varphi} \quad (2.4)$$

where  $x_{mem}$  is the thickness of the support layer,  $\tau$  is the tortuosity and  $\varphi$  is the porosity. To reduce the internal concentration polarization, the structural parameter,  $S_w$ , of the membrane needs to be minimized.

For an osmotically driven membrane process, high water flux and low reverse solute flux are desired. In short, a high water permeability coefficient and a low solute permeability coefficient and structural parameter are required (Alsvik, 2013). Both  $S_w$  and  $A_w$  values are intrinsic membrane properties. The  $S_w$  value is only governed by the membrane thickness of the support layer, tortuosity and porosity. The water permeability is affected by the membrane property and the water viscosity (Lay, 2012). However, the  $B_w$  value is dependent on the type of the draw solution (Boo, 2015). Draw solutes with high mass transfer coefficient induces a higher solute permeability coefficient. Thus, the development of a semi-

permeable membrane that possesses high salt rejection and minimal internal concentration polarization is pivotal together with the appropriate draw solute selection.

### 2.2.3 Draw solute

Discovering an ideal draw solution is the key to the development of forward osmosis technology. Thus, several draw solutes have been proposed; SO<sub>2</sub> (Batchelder, 1965), Al<sub>2</sub>SO<sub>4</sub> (Frank, 1972), nanoparticles (Adham, 2007) and ammonium bicarbonate (McCutcheon, 2005). There are several characteristics that an ideal draw solute should possess; high osmotic pressure, low toxicity, optimum molecular weight, high solubility, easy recovery, high diffusion coefficient, etc (Chekli, 2012). As discussed earlier, key property for a draw solution to possess is the high osmotic pressure. For an ideal dilute solution, the osmotic pressure can be given as

$$\pi = n \left( \frac{C_s}{MW} \right) RT \quad (2.5)$$

based on the theory proposed by Van't Hoff (Van't Hoff, 1887).  $n$  is the number of moles of species formed by the dissociation of solutes in the solution,  $C_s$  is the solute concentration in g L<sup>-1</sup>,  $MW$  is the molecular weight of the solute,  $R$  is the gas constant and  $T$  is the absolute temperature of the solution. From the expression, it can be deduced that the lower the molecular weight of the draw solute the larger the osmotic pressure. And solutes with lower molecular weight usually have higher diffusion coefficient compared to those with larger molecular weight. However, draw solutes with very small molecular weight showed higher

reverse salt diffusion. Basically there is a trade-off between small solute size to minimize ICP and large solute size to decrease reverse draw solute flux. It was found that non-ionic draw solutes with molecular weight less than  $100 \text{ g mol}^{-1}$  tend to permeate through the membrane. And it shows that concentration of the draw solute in the solution has a positive correlation with the osmotic pressure, meaning that high solubility is vital. The draw solute must be non-toxic since only negligible amounts are allowed in the product drinking water. Chemical compatibility with the membrane must also be looked into as the solution may degrade or react with the membrane. Concentration polarization, one of the biggest issues in FO process, is influenced by the diffusion coefficient and viscosity of the draw solution thus, they must be considered as well when deciding the draw solution. Furthermore, it was found that the size exclusion and electrostatic interactions have a substantial role in controlling solute transport across the membrane. It was found that cations such as  $\text{Mg}^{2+}$ ,  $\text{Ca}^{2+}$  and  $\text{Ba}^{2+}$  have lower molar fluxes as they have a relatively larger hydration radii and divalent charge (Wilson & Stewart, 2013). It too must be considered when deciding the draw solution.

In FO process, the main osmosis process operates near ambient pressure and temperature meaning that no intense thermal or hydraulic condition is needed. However, the product of FO process itself is a diluted draw solution. Thus, in order to obtain fresh water as the final product, which is what the consumer expects, another step is required; draw solute recovery process. And this is the major energy consuming part in the whole FO process. This means that reducing the energy usage in draw solute recovery will significantly reduce the cost of FO. Thus, selecting an appropriate draw solute which is safe, highly soluble and at the

same time easily separable, is vital.

## **2.2.4 Thermodynamic analysis of FO process**

### **A. Draw solute candidate**

Discovering the ideal draw solute is crucial as it directly influences the FO process performance and at the same time dictates the energy consumption of the whole process. As mentioned, the fundamental purpose of the draw solute in a FO process is to induce high osmotic pressure when dissolved in the draw solution. The osmotic pressure of the draw solution in FO cell needs to exceed that of the sea water in order to drag the water molecules from the seawater. Consequently the key feature that an ideal draw solute needs to possess is high solubility. Since seawater has an osmotic pressure about 27 atm (McCutcheon, 2007), the draw solute has to be capable of achieving an osmotic pressure above 27 atm when dissolved in the draw solution.

Additionally, an ideal draw solute needs to be non-toxic as the final product of the process is designed for drinking water. And for economic reasons, the draw solute cannot be based on rare-metals or expensive chemicals. And most importantly, the draw solute has to be easily separable. Since the waste heat from the gas turbine system is to be used for the draw solute separation system, the draw solute is required to be separated using heat. In other words, chemicals which have lower boiling point than water are preferred. Appropriate draw solute candidates have been identified through literature survey based on the mentioned criteria as in Figure 2.7.

For this study, ammonium bicarbonate, sulfur dioxide and trimethylamine-

carbon dioxide were selected. Before going into the thermodynamic analysis on the draw solute separation process of each draw solute candidates, physical properties of the draw solutes have been compared. The pH, osmotic pressure and viscosity of the draw solutions and the individual ion diffusivities have been obtained using OLI stream analyzer (OLI systems, 2009). The mutual diffusion coefficients were determined using the below equation (Ghiu, 2002) (Cussler, 1997)

$$D_{mutual} = \frac{\frac{|z^+|}{D^+} + \frac{|z^-|}{D^-}}{|z^+| + |z^-|} \quad (2.6)$$

where  $z^+$  and  $z^-$  are the cation/anion charges and  $D^+$  and  $D^-$  are the individual cation/anion diffusivities. Generally, the mass transfer coefficient increases with increasing diffusivity. And higher mass transfer coefficient tends to increase the solute permeability coefficient. As seen in Table 2.2, the diffusion coefficient of sulfur dioxide is higher than that of the ammonium bicarbonate and TMA-carbon dioxide which shows the possibility of a high solute permeability coefficient,  $B_w$ .

## **B. Evaluation on draw solutes**

The selected three draw solutes, ammonium bicarbonate, sulphur dioxide and trimethylamine-carbon dioxide were further evaluated using UNISIM and OLI property package. The thermal efficiencies of the draw solute candidates were evaluated using a parameter called the gain output ratio (GOR). The GOR is obtained by dividing the enthalpy of vaporization of the steam used in the draw solute recovery system by the specific energy requirement for producing water from the desalination process. It practically means the amount of water produced

per amount of steam used. It is defined as (McGinnis & Elimelech, 2007)

$$GOR = \frac{H_{vapsteam}}{H_{duty}} \quad (2.7)$$

Basically the draw solute candidates were evaluated based on the ease of separation. In order to conduct the evaluation, the separation of the draw solute recovery system of the draw solute candidates were simulated. For comparison, the concentrations of the draw solute candidates were given as 1.0 M which is within the previously defined diluted draw solution osmotic pressure range (McCutcheon, 2005). And the draw solutes were separated using a series of absorption columns.

Before conducting the feasibility study on the integration concept, the draw solute separation system is simulated and the operation conditions are established. Optimum number of stages is found to be four through parametric study as shown in Figure 2.8. However, the increase in efficiency is relatively small compared to the economic cost for an additional stage. Thus, for further study, draw solute separation process is decided to possess 3 stages. A single column was assumed to carry 20 trays and the minimum approach temperatures in heat exchangers were set to be around 5 °C. The pressure drop of the reboiler and the top tray in the absorption column was set as 0.001 MPa. Furthermore, the draw solute level in the product water was set as the limit listed in Table 2.2. Since no maximum drinking water contaminant levels are established for the three draw solute candidates the assumed limits listed below which are set using a conservative standard or case study are used for the analysis.

Using the selected parameters the simulation of the draw solute recovery system for the three draw solute candidates have been conducted. The thermal

energy was inserted in the first column and recycled throughout the other two stages. The operation temperatures of each absorption columns were decided as 120.0 °C, 93.3 °C, 66.7 °C and 40 °C. Heat in the first column was assumed to be 30 MWt. Comparison between the draw solute candidates have been made as shown in Figure 2.9. As seen in the graph, sulfur dioxide shows the highest thermal efficiency among the three draw solute candidates. Ammonium bicarbonate shows the second best thermal efficiency and trimethylamine-carbon dioxide show relatively poor thermal efficiency compared to the other two draw solutes. In terms of thermal efficiency, it can be said that sulfur dioxide is the best draw solute. However, the FO performance of ammonium bicarbonate has been studied extensively by many research groups whereas sulfur dioxide was suggested by Batchelder and has not been favored due to poor water flux and salt rejection. Thus, in terms of realistic perspective ammonium bicarbonate will be a more promising draw solute. Thus, further integration analysis will be conducted on the ammonium bicarbonate.

## **2.3 Thermodynamic Analysis of the Integrated System**

The integration concept of the VHTR and the forward osmosis seawater desalination process is quite explicit. The waste heat from the VHTR power conversion system is used in the draw solute recovery system. The basic concept can be seen in Figure 2.10. Since draw solute recovery system of the whole FO process is the most energy demanding part, by integrating the waste heat from the gas turbine system most of the energy requirement in the FO process is covered.

After simulating both the PCSs and the draw solute recovery system, the thermodynamic coupling of the FO process and the power conversion systems is carried out. The integration is carried out with VHTR helium and supercritical carbon dioxide Brayton cycle. Water Rankine cycle is neglected due to its low waste heat temperature.

The integration of the two systems will be explained in more detail. Figure 2.11 shows the integrated system of forward osmosis and helium Brayton cycle in UNISIM. The waste heat streams are divided into several streams according to the temperature conditions. As the absorber column in 1st stage operates at 120 °C, the portion of waste heat stream which carries a temperature of 125 °C or higher is connected to the first stage column using a heat exchanger. And since the second stage column operates at 90 °C, the portion of waste heat stream which carries a temperature of 95 °C or higher, together with the heat stream extracted from the first stage concentrated draw solute gas stream, is injected in to the second stage column. The same procedure is conducted for the third stage. Addition to this, the water product streams are used to heat up the feed streams in each stage in order to enhance thermal efficiency.

Figure 2.12 displays the schematic of the supercritical carbon dioxide Brayton cycle and FO integration system in UNISIM. Similar thermodynamic coupling process occurs as in Figure 2.11. Some differences can be observed due to the different waste heat stream conditions. As the waste heat stream is discharged at 115.7 °C in the supercritical carbon dioxide Brayton cycle, the operating temperatures of the columns are slightly altered. And since only single waste heat stream exists, the integration seems much simpler.

The calculation results of both integration systems are shown in Tables 2.3 and

2.4. Parametric study on the diluted draw solution concentrations (0.5 M ~ 1.5 M) for both integration systems have been conducted. And as can be seen in the Tables 2.3 and 2.4, the GOR and Equivalent work values show similar trends as it did in the independent draw solute recovery system. The increase in diluted draw solution concentration causes decrease in GORs and increase in equivalent work values. In other words, the system is more efficient when lower concentrations of draw solutions are entered as feed.

The GOR comparison of the two integration systems can be seen in Figure 2.13. The GOR of the supercritical carbon dioxide Brayton cycle and forward osmosis integrated system is clearly lower than that of the helium Brayton cycle and forward osmosis integrated system. This is due to the different waste heat stream conditions of both cycles. The supercritical carbon dioxide Brayton cycle waste heat stream has a temperature of 115.7 °C whereas the helium Brayton cycle waste heat streams have temperatures of 152.2 °C and 120.5 °C. Lower temperature waste heat results in lower heat recycle and thus, lower GORs.

In Figure 2.14, the GORs of the integrated draw solute separation system with helium Brayton cycle and the independent draw solute separation system have been compared. The GOR values for draw solution concentration ranging from 0.5 M to 1.5 M have been compared. As can be seen in the bar graph, the GOR values drop near a value of 6 between the integrated and independent draw solute separation systems. This can be explained by the less energy recycle. In the independent draw solute recovery system, heat introduced in the system is all injected in the first column and recycled throughout the stages. Whereas in the draw solute recovery system within the integrated system, the heat introduced to the system is divided according to the temperature they carry and injected to each

column accordingly. This results in less energy recycle and as a result, lower GORs.

The helium Brayton cycle and FO integrated system calculations were used for comparison with other technologies; MED and MSF. The typical plant values were used for the comparison. In this study, the MED with a top brine temperature (TBT) of 70 °C was referred and MSF with a top brine temperature of 120 °C was referred (Morin, 1993). As shown in Figure 2.15, the thermal efficiency of MSF range around 8 to 12 and MED from 6 to 12 (IAEA, 2000) (Morin, 1993). These values do not differ greatly when compared to the FO GOR which ranges from 9.0 to 13.8. The maximum and minimum GOR values of FO-VHTR system are higher than that of GORs of the two conventional technologies. And this value can be further improved if the lower diluted draw solution concentration can be achieved. While the GOR values between the three technologies are comparable the waste heat utilization rate calculated based on the TBTs of the technologies differ significantly.

For the waste heat utilization rate and the water production calculations, the maximum GOR of 12 for both MSF and MED was used and middle GOR value, 10.8, for FO system was assumed for conservative assumption. Even so, as can be seen in the Figure 2.16, the waste heat utilization of MSF is only 12.6 % while that of FO is 81.5 %. This is due to the flexibility of the draw solute recovery system of FO process. And although the technologies have similar GORs, due to the great difference in the waste heat utilization rates between them the water productions of the 3 technologies result as shown in Figure 2.17. When coupled to the same capacity VHTR plant, the water production is largest for FO. It is more than 5 times larger than that of MSF and nearly 20 % larger than that of MED.

Thus, when utilizing the waste heat from VHTR, FO can be a more efficient desalination technology than MED and MSF.

Therefore it can be concluded that the suggested integration concept of VHTR and FO desalination system is an effective cogeneration system with significantly higher energy utilization rate which resulted in 5 times higher water utilization rate compared to the conventional desalination and VHTR integrated system. This is possible due to the high grade waste heat from the VHTR and flexible FO draw solute recovery system. Thus, the novel VHTR-FO system suggested in this study is a very promising and strong system concept which has a number of advantages over conventional technologies.

Table 2. 1 Waste heat conditions for PCS options

<b>Power Conversion System</b>	<b>Number of waste heat streams</b>	<b>1<sup>st</sup> waste heat stream temperature (°C)</b>	<b>1<sup>st</sup> waste heat stream pressure (kPa)</b>	<b>2<sup>nd</sup> waste heat stream temperature (°C)</b>	<b>2<sup>nd</sup> waste heat stream pressure (kPa)</b>	<b>Waste stream energy flow (MW)</b>	<b>Waste heat energy / Reactor total energy (%)</b>
Helium Brayton cycle	2	152	2653	120.5	4704	115	57.6
Supercritical CO <sub>2</sub> Brayton Cycle	1	116	8732	-	-	94	47.4
Water Rankine Cycle (IAEA, 2011)	1	63	5.08	-	-	130	64.9

Table 2. 2 Draw solute candidates

Draw solute candidate	Ammonium bicarbonate	Sulfur dioxide	Trimethylamine-carbon dioxide (Boo, 2015)
Molar concentration (M)	1.0	1.0	1.0
Osmotic pressure (atm)	40.0	27.8	48.8
Molecular weight of the ions (g/mol)	NH <sub>4</sub> <sup>+</sup> : 18.0 HCO <sub>3</sub> <sup>-</sup> : 61.0	H <sup>+</sup> : 1.0 HSO <sub>3</sub> <sup>-</sup> : 81.0	NH(CH <sub>3</sub> ) <sub>3</sub> <sup>+</sup> : 60.0 HCO <sub>3</sub> <sup>-</sup> : 61.0
pH	7.50	0.96	7.75
Mutual diffusion coefficient (m <sup>2</sup> /s)	1.49 x 10 <sup>-9</sup>	1.92 x 10 <sup>-9</sup>	1.24 x 10 <sup>-9</sup>
Diffusivity (m <sup>2</sup> /s)	NH <sub>4</sub> <sup>+</sup> : 1.96 x 10 <sup>-9</sup> HCO <sub>3</sub> <sup>-</sup> : 1.21 x 10 <sup>-9</sup>	H <sup>+</sup> : 7.80 x 10 <sup>-9</sup> HSO <sub>3</sub> <sup>-</sup> : 1.09 x 10 <sup>-9</sup>	NH(CH <sub>3</sub> ) <sub>3</sub> <sup>+</sup> : 1.45 x 10 <sup>-9</sup> HCO <sub>3</sub> <sup>-</sup> : 1.09 x 10 <sup>-9</sup>
Limit (ppm)	1.5 (CDW, 2013)	1.0	1.5
Solubility (g/100mL)	21.6	94.0	miscible

Table 2. 3 Energy data of VHTR helium Brayton and FO integration system

Draw Solution Concentration (M)	Heat Duty (MJ/m <sup>3</sup> )	Gain Output Ratio	Equivalent Work (kWh/m <sup>3</sup> )
0.5	183	13.8	0.020
1.0	245	10.7	0.025
1.5	280	9.0	0.036

Table 2. 4 Energy data of VHTR supercritical carbon dioxide Brayton and FO integration system

<b>Draw Solution Concentration (M)</b>	<b>Heat Duty (MJ/m<sup>3</sup>)</b>	<b>Gain Output Ratio</b>	<b>Equivalent Work (kWh/m<sup>3</sup>)</b>
0.5	231	10.8	0.022
1.0	309	8.1	0.026
1.5	391	6.4	0.027

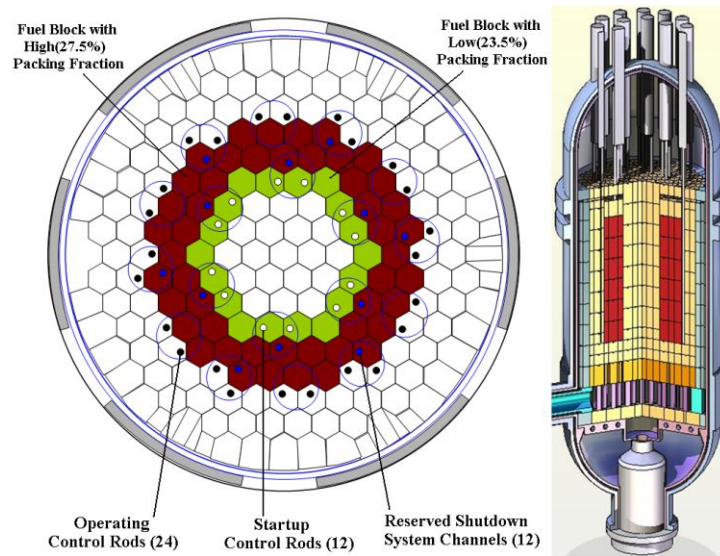


Figure 2. 1 Core configurations of PMR 200 (Jo, 2008)

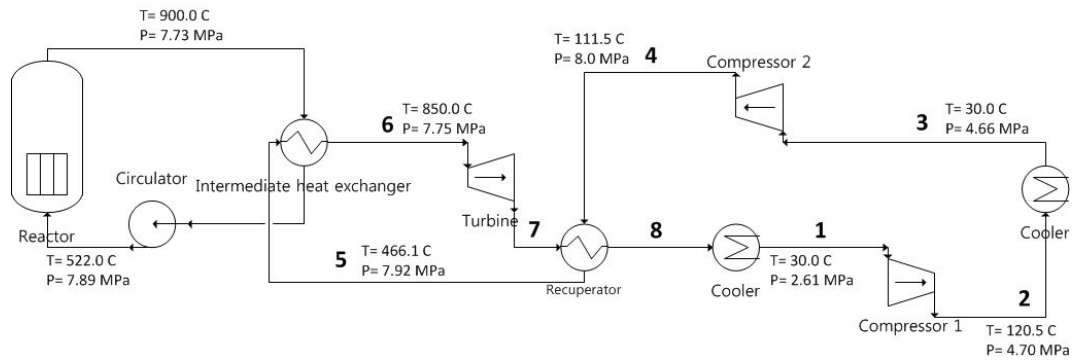


Figure 2. 2 Schematic of the simulated helium Brayton cycle

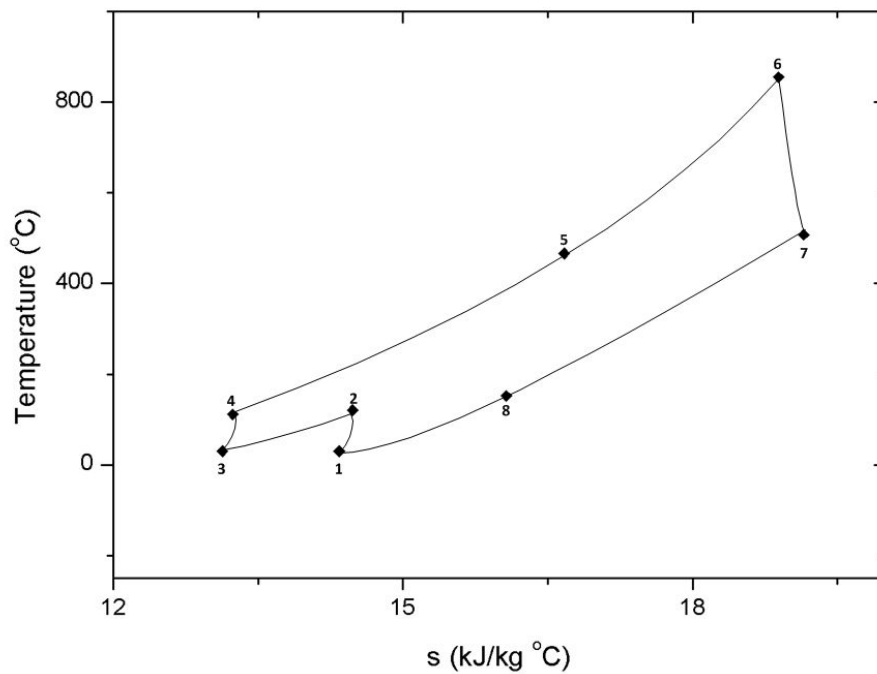


Figure 2. 3 Temperature-entropy diagram for the simulated helium Brayton cycle

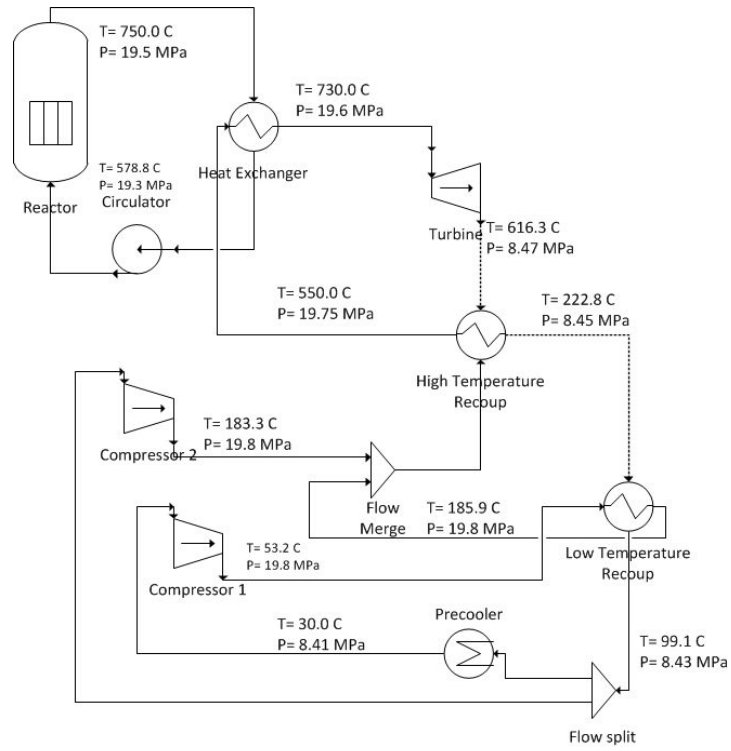


Figure 2. 4 Schematic of the supercritical carbon dioxide Brayton cycle

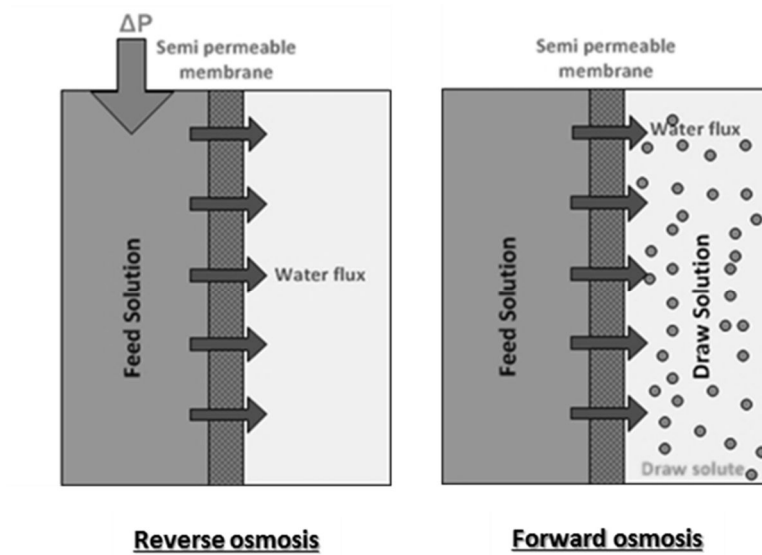


Figure 2. 5 Forward Osmosis (FO) and Reverse Osmosis (RO)

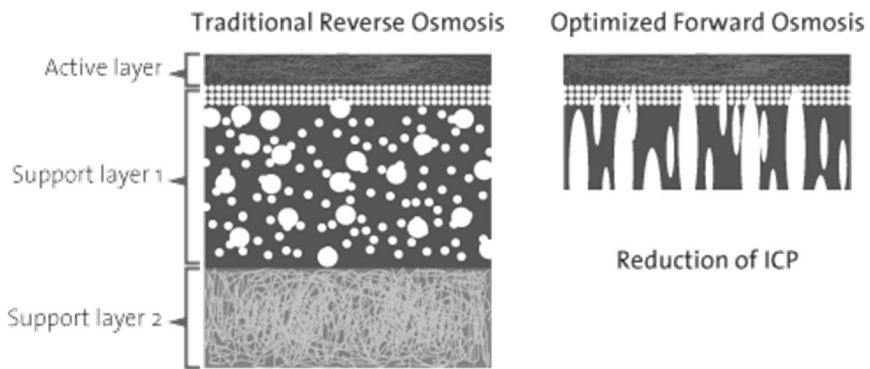


Figure 2. 6 Comparison between RO and FO membranes (Bluetec, 2016)

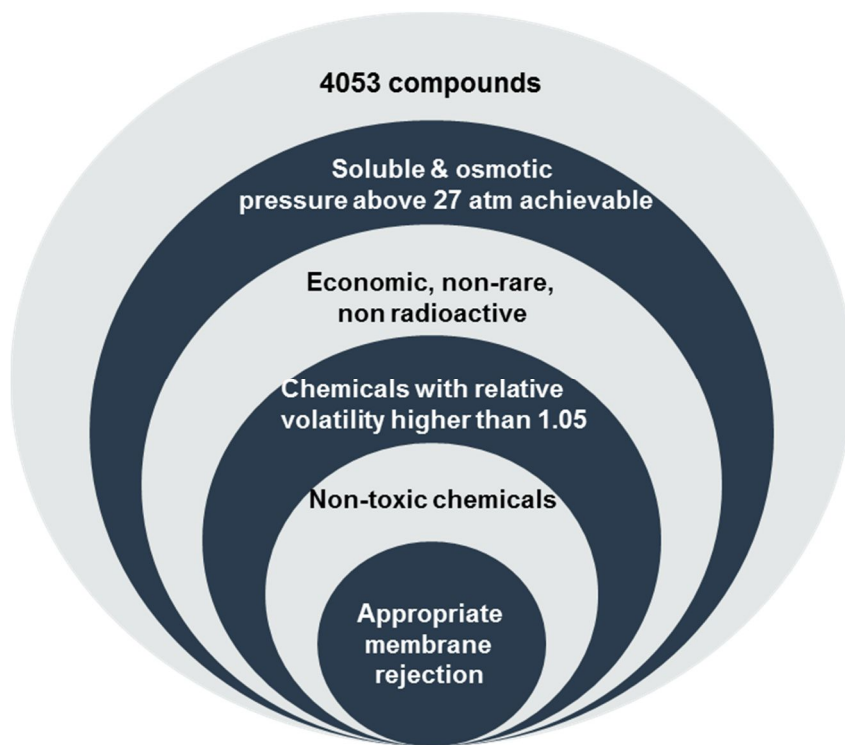


Figure 2. 7 Defined draw solute criteria

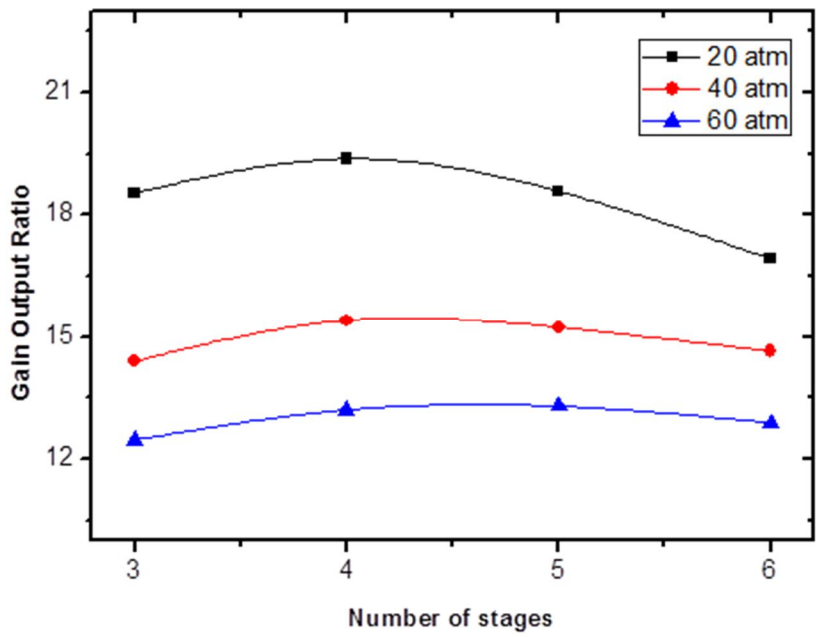


Figure 2. 8 Parametric study on the number of stages (ammonium bicarbonate)

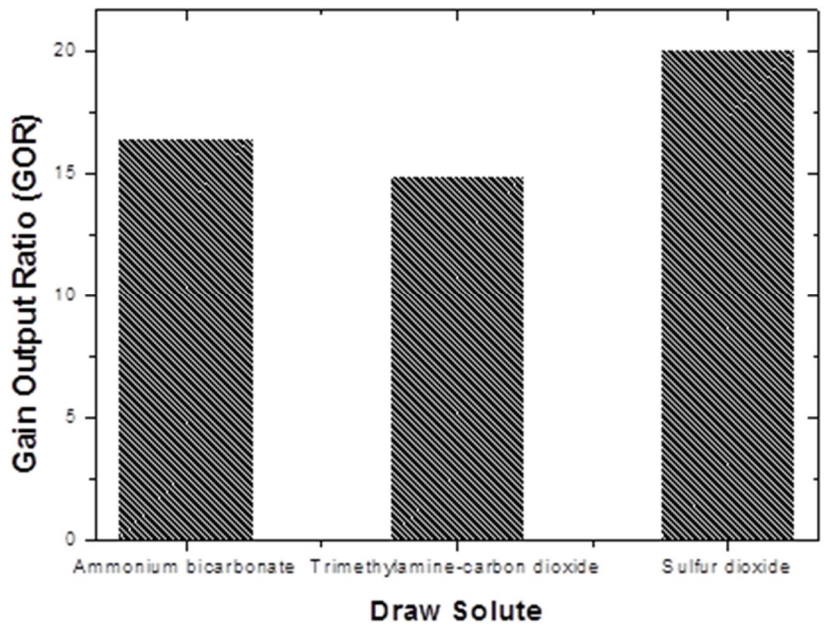


Figure 2. 9 Comparison on the thermal efficiencies of the three draw solutes

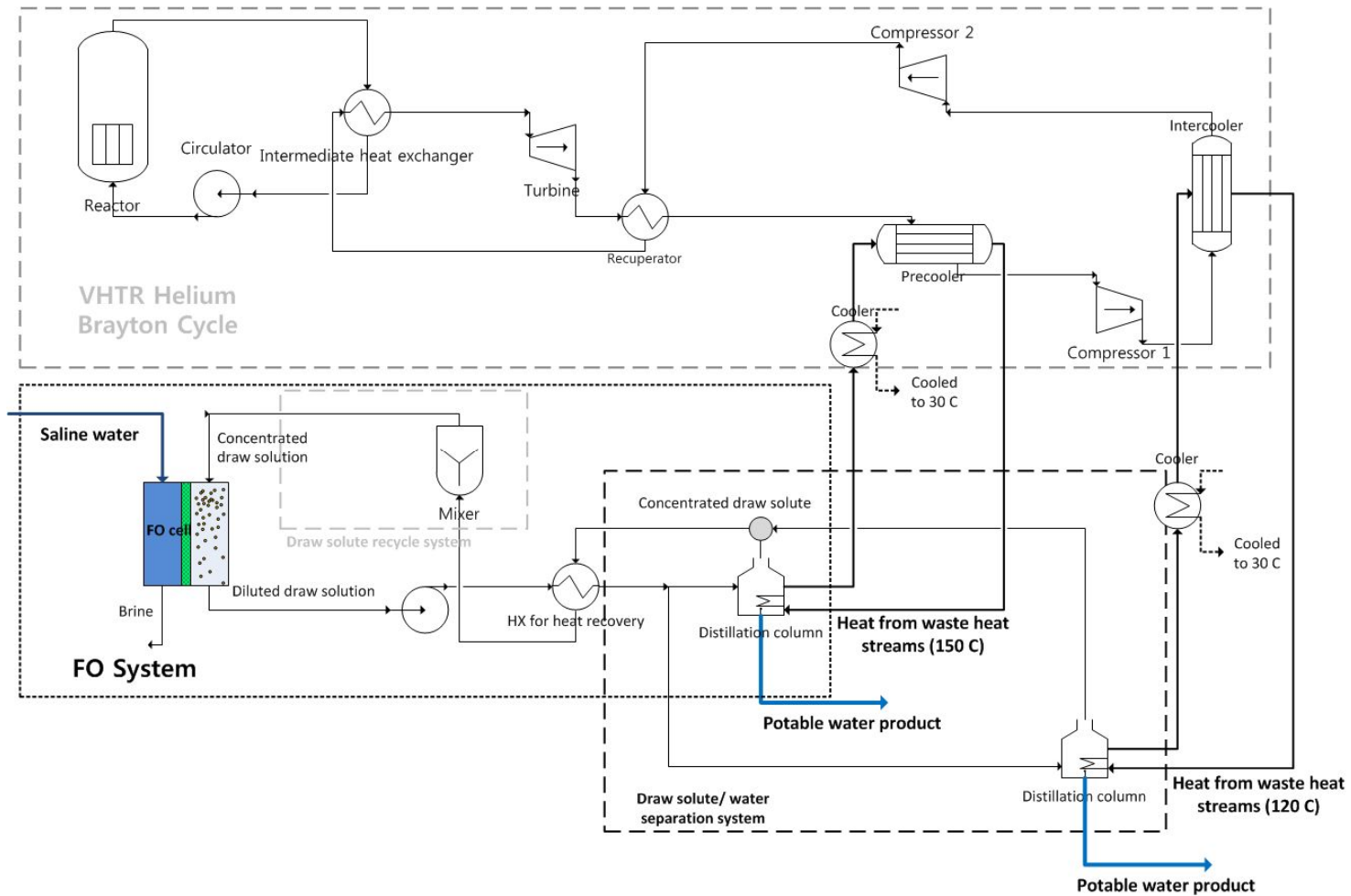


Figure 2. 10 Schematic of the integration concept of VHTR and forward osmosis desalination system (Park & Kim, 2014)

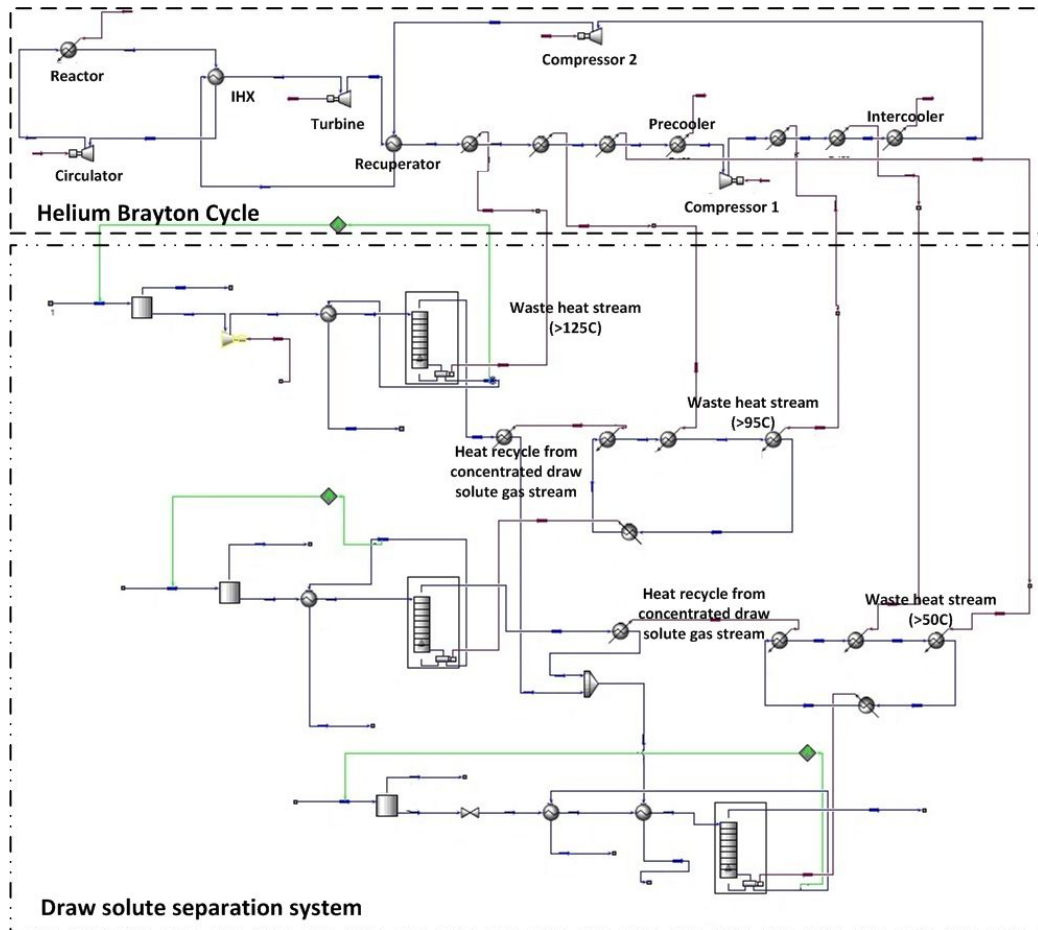


Figure 2. 11 Simulated FO-VHTR helium Brayton cycle integrated system on UNISIM

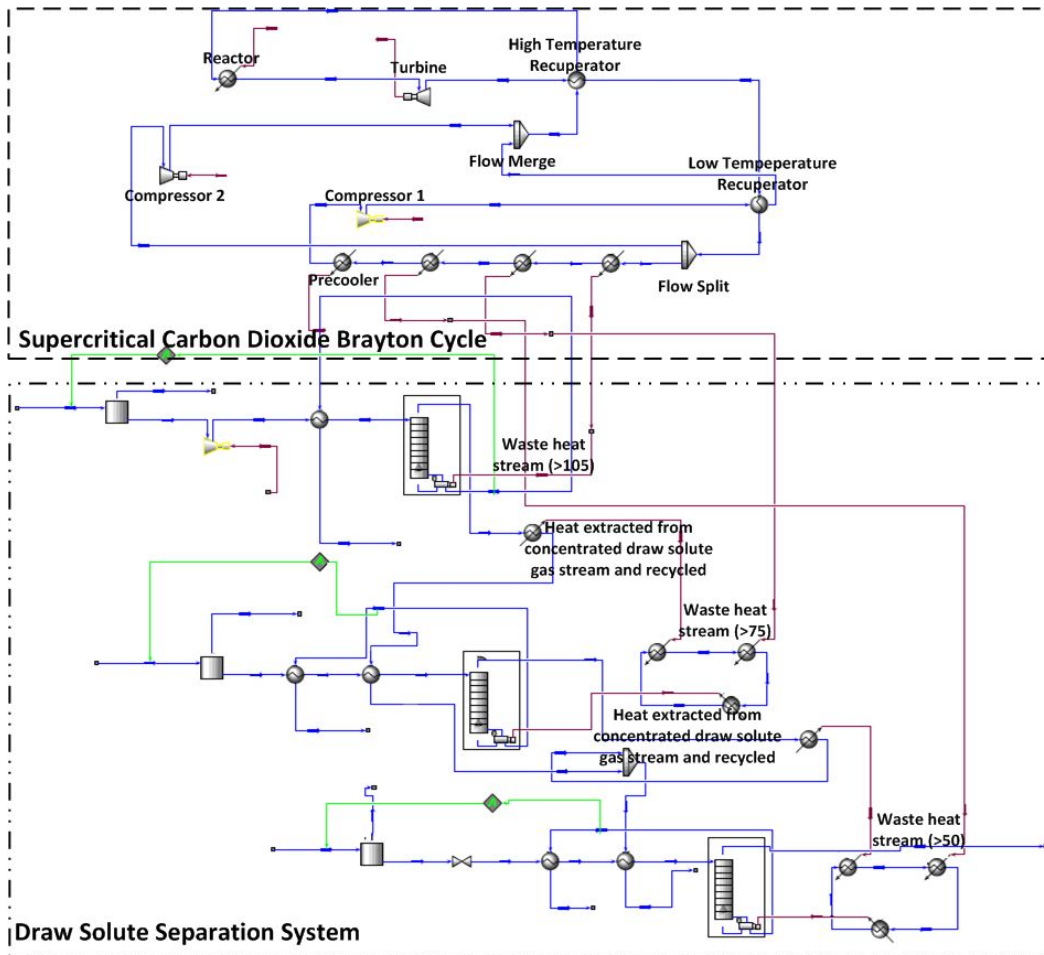


Figure 2. 12 Simulated FO-VHTR supercritical carbon dioxide integrated system on UNISIM

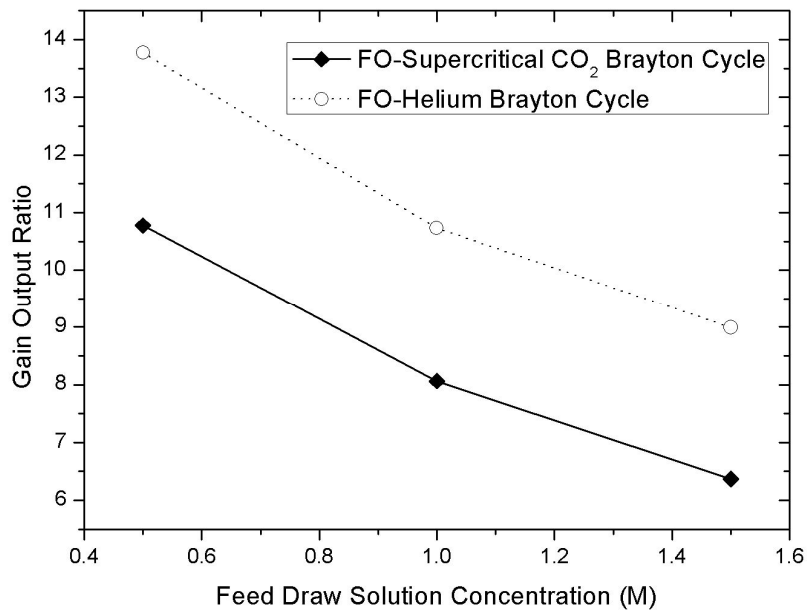


Figure 2. 13 Comparison of GORS calculated in FO-helium Brayton system and FO-supercritical carbon dioxide Brayton system

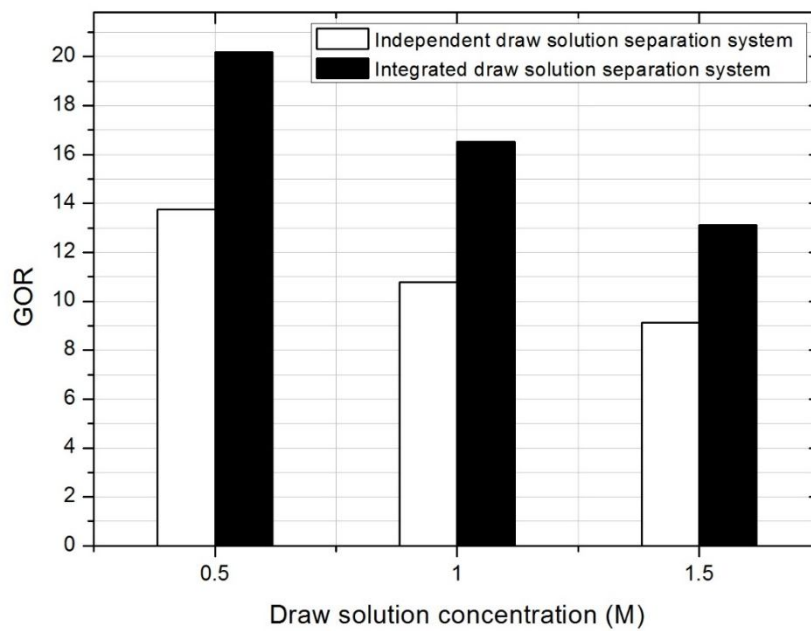


Figure 2. 14 Comparison of independent and integrated draw solute separation system

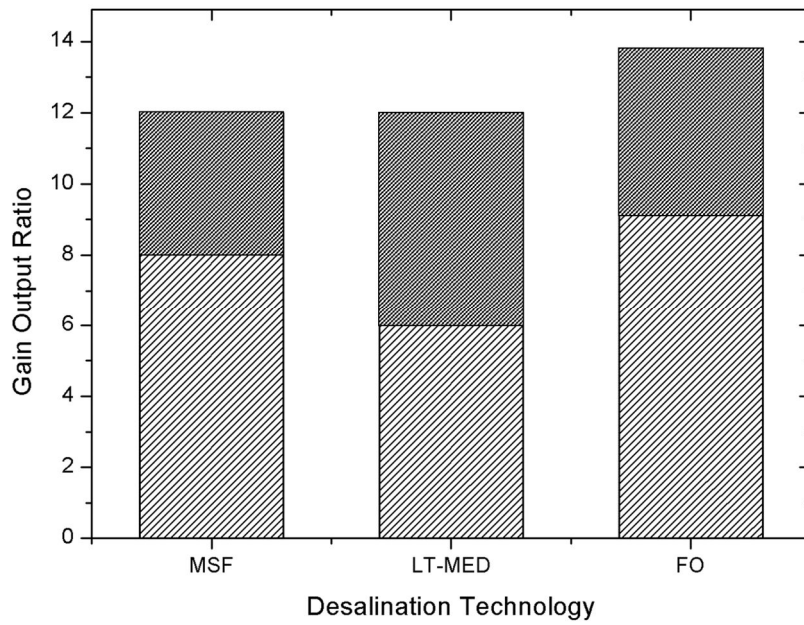


Figure 2. 15 Comparison of GORs of various desalination technologies when integrated with helium Brayton cycle

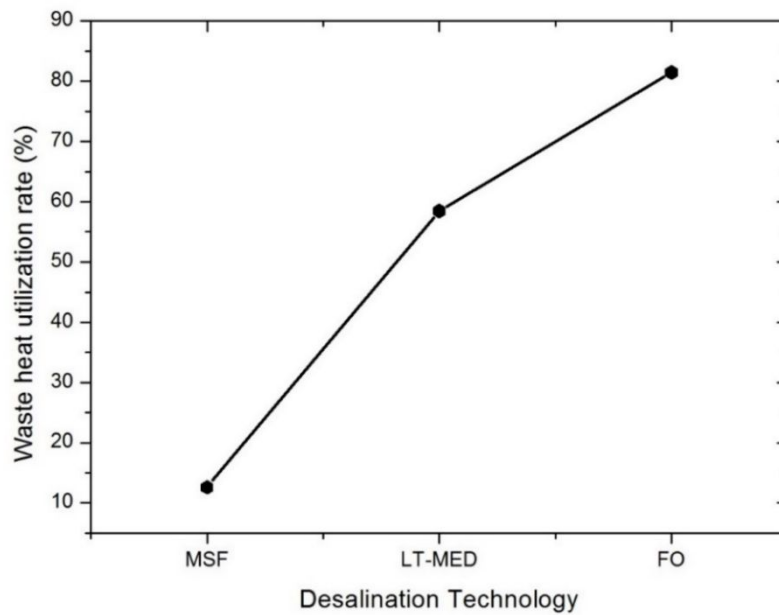


Figure 2. 16 Comparison of waste heat utilization rates of various desalination technologies when integrated with helium Brayton cycle

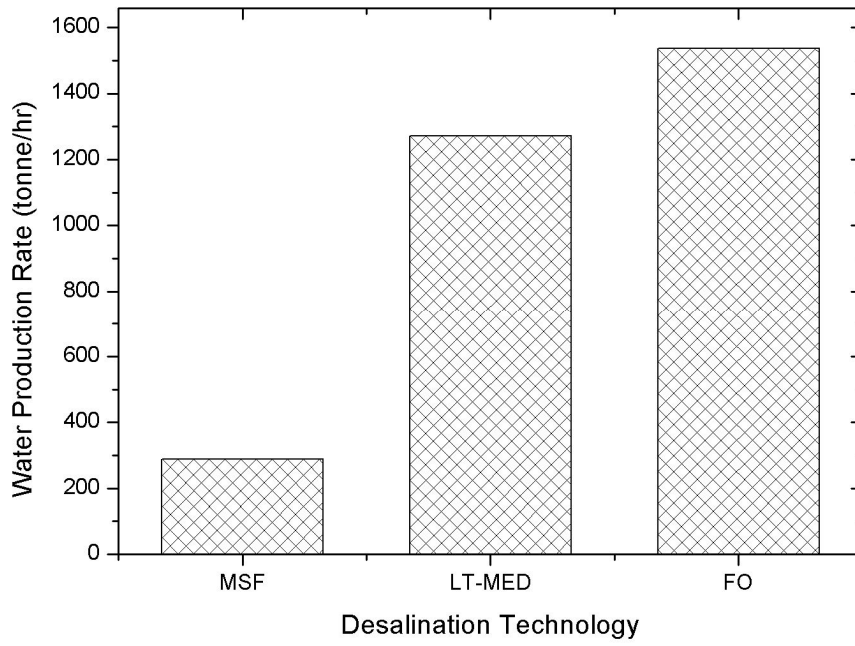


Figure 2. 17 Comparison of water production of various desalination technologies when integrated with helium Brayton cycle

## Chapter 3

# Development and Verification of Behavior of Tritium Analytic Code

### 3.1 Tritium Behavior

As can be seen in Figure 3.1, tritium is involved in various phenomena in the VHTR integrated system. Tritium is generated and lost through various processes. The processes include tritium production, sorption, leakage, purification and permeation. In VHTR, tritium is mainly produced as a byproduct in ternary fission reaction. Tritium is also generated in neutron capture reactions with the core and coolant materials such as  ${}^6\text{Li}$ ,  ${}^3\text{He}$ ,  ${}^{10}\text{B}$  and  ${}^7\text{Li}$ . Most of the tritium generated in the core is retained or sorbed in the reactor core and some are released into the coolant. Some of the tritium in the system is removed through purification, portion of tritium is leaked out of the system and some permeate into secondary and even to the integration loop. As seen here, tritium produced in the core can migrate down into the secondary system, into the industrial process and into the final product of that process through permeation in the heat exchanger. Therefore, understanding and predicting tritium behaviour, migration of tritium to downstream processes is important in terms of safety, licensing and public

acceptance. In order to analyse the associated tritium phenomena in the VHTR integrated system, Behaviour of Tritium Analytic Code (BOTANIC), a tritium code is developed in this study.

## 3.2 Physical Models

### 3.2.1 Conservation Equations

One of the distinctive features of the BOTANIC code is its capability to analyse system dynamics. This is possible as the code solves mass and energy conservation equations. In order to solve the transport of the species in the system basic conservation equations are solved as shown below. Generation or loss of each species is reflected using the source terms;  $S_m$  and  $S_e$ . And the mass flowrate,  $F$ , is given as an input.

$$\frac{dM_{T,i}}{dt} = (F \cdot x_{in,i} - F \cdot x_{out,i} + S_{m,i}) \quad (3.1)$$

$$\frac{dU}{dt} = (F \cdot h_{in} - F \cdot h_{out} + Q + S_e) \quad (3.2)$$

### 3.2.2 Tritium Generation

As mentioned, tritium is generated through various reactions in the reactor core. The main tritium birth mechanism is ternary fission of the fuel (uranium-233, uranium-235, plutonium-239 and plutonium-241) in the core. Tritium is also produced in neutron capture reactions in the core. Tritium production can be

calculated using the following equations (Ohashi & Sherman, 2007).

*Ternary fission*

$$\frac{d(N_{T(Ter)})}{dt} = Fi \cdot W \cdot Y - \lambda \cdot N_{T(Ter)} \quad (3.3)$$

*Birth from Lithium-6*

$$\frac{d(N_{Li6})}{dt} = -\varphi_{th} \cdot \sigma_{Li6T} \cdot N_{Li6} \quad (3.4)$$

$$\frac{d(N_{T(Li6)})}{dt} = \varphi_{th} \cdot \sigma_{Li6T} \cdot N_{Li6} - \lambda \cdot N_{T(Li6)} \quad (3.5)$$

*Birth from Helium-3*

$$\frac{d(N_{He3})}{dt} = f \cdot N_{He3}^{\circ} - f \cdot N_{He3} - \varphi_{He} \cdot \sigma_{He3T} \cdot N_{He3} \quad (3.6)$$

$$\frac{d(N_{T(He3)})}{dt} = \varphi_{He} \cdot \sigma_{He3T} \cdot N_{He3} - \lambda \cdot N_{T(He3)} \quad (3.7)$$

$$\varphi_{He} = \frac{M_{core}}{M_{total}} \cdot \varphi_{th} \quad (3.8)$$

*Birth from Boron-10*

$$\frac{d(N_{B10})}{dt} = -(\varphi_{th} \cdot \sigma_{B10Li7} + \varphi_f \cdot \sigma_{B10T}) \cdot N_{B10} \quad (3.9)$$

$$\frac{d(N_{Li7(B10)})}{dt} = \varphi_{th} \cdot \sigma_{B10Li7} \cdot N_{B10} - \varphi_f \cdot \sigma_{Li7T} \cdot N_{Li7(B10)} \quad (3.10)$$

$$\frac{d(N_{T(B10)})}{dt} = \varphi_f \cdot \sigma_{Li7T} \cdot N_{Li7(B10)} + \varphi_f \cdot \sigma_{B10T} \cdot N_{B10} - \lambda \cdot N_{T(B10)} \quad (3.11)$$

*Birth from Lithium-7*

$$\frac{d(N_{Li7})}{dt} = -\varphi_f \cdot \sigma_{Li7H3} \cdot N_{Li7} \quad (3.12)$$

$$\frac{d(N_{T(Li7)})}{dt} = \varphi_f \cdot \sigma_{Li7T} \cdot N_{Li7} - \lambda \cdot N_{T(Li7)} \quad (3.13)$$

Lithium-6 and lithium-7 are impurities in the core graphite structure; sleeve, spine, reflector and fuel matrix. Basically, the thermal neutron from the core react with the lithium-6 in the graphite structure. Some of the tritium atoms produced in the neutron reaction are captured within the solid structure and some diffuse through the solid structure. Once the tritium atom reaches the surface of the structure it tends to bind with hydrogen and gets released into the helium coolant. The reaction mechanisms of lithium-7, boron-10 and helium-3 are similar to that of the lithium-6 neutron capture reaction as seen in Figure 3.2-3.4. The main difference lies in the location of the reaction occurrence and the release mechanism. Helium-3 neutron reaction occurs within the coolant as the helium isotope is located inside the coolant. And since the reaction occurs within the coolant the generated tritium directly binds with the hydrogen in the coolant to form HT gas and distributes inside the system.

### 3.2.3 Tritium Loss

#### A. Tritium Leakage

In the VHTR, leakage of coolant occurs through defects or micro-gaps between components such as pipe, flanges, etc. As there is a certain concentration of tritium present in the coolant, tritium is lost with the bulk coolant. The leak rate,

$S_{leak}$  of chemical  $i$ , is calculated using equation 3.14.  $M_T$  represents the total mass holdup of the node,  $L_R$  is the leakage rate. And  $x_i$  is the mass fraction of chemical  $i$ , in this case tritium, in the node.

$$S_{leak,i} = M_T \cdot L_R \cdot x_i \quad (3.14)$$

### **B. Tritium Purification**

Most of the tritium in primary and secondary loops is removed in the purification system. The removal rate of tritium through purification is expressed in equation 3.15. Where  $F_{PF}$  is the mass flow rate to the purification system and  $\eta_{PF,i}$  is the fractional purification efficiency of tritium in the purification system. The purification efficiency of tritium typically exceeds 95 %.

$$S_{PF,i} = F_{PF} \cdot \eta_{PF,i} \cdot x_i \quad (3.15)$$

### **C. Tritium Sorption**

Tritium behaviour in the reactor component such as generation, diffusion and release are accompanied by adsorption in graphite materials (Hong, 2015). Gas cooled reactor types consist of large quantities of graphite as it utilizes graphite as moderator and reflector. Many studies have been conducted on the reaction of tritium and graphite, and it was reported that adsorption and desorption reactions have influence on the tritium release rate in VHTR systems (Gainey, 1976). The release rate were found dependent on temperature and not on the physical form of the graphite (Fachinger, 2008). It was also reported that the adsorption occurs only on the edge of the graphite crystal but not inside graphite (Redmond & Walker,

1960).

The sorption reaction is a complex reaction with many uncertain variables such as impurities in coolant, contamination of graphite, porosity of graphite, etc. Currently, not much research on the tritium adsorption reactions in VHTR system has been conducted. And in most tritium codes, the sorption reaction is analysed using a very simplified Temkin isotherm model where temperature effect is not considered or the B. F. Myers model where temperature effect and the partial pressure effect are considered. In BOTANIC code, the Myers model is implemented for the tritium sorption analysis. As the Myers sorption model is an equilibrium model additional differential equation with newly defined parameter  $M_{sorp}$  is implemented as well in order to calculate sorption rate.

*B.F. Myers sorption model (General atomics, 2006)*

$$A_s = \frac{C_{1,s} \cdot (1 + f_s \cdot C_{2,s} \cdot C_H) \cdot P_{H_2}}{1 + \exp(C_{3,s} \cdot (T - T_0))} \quad (3.16)$$

$$C_H = 1 + \exp[C_{3,s} \cdot (T - 1423)]^{-1} \quad (3.17)$$

$$M_{eq_s} = A_s \cdot \theta_s \cdot M_{graphite} \cdot C_{sorp} \quad (3.18)$$

$$\frac{dM_s}{dt} = (M_{eq_s} - M_s) = S_s \quad (3.19)$$

#### **D. Tritium Permeation**

Permeation is the core tritium transport mechanism in most of the nuclear reactor systems. Permeation phenomena has been noted as the most important activity in previous studies (Kim, 2010). Since permeation is the key mechanism

in tritium analysis, the BOTANIC code adopts a detailed permeation model unlike other existing tritium analysis codes in addition to the simple correlation based permeation model. For convenience BOTANIC provides a variety of permeation models including the simple correlation based permeation model, diffusion based equilibrium permeation model and non-equilibrium permeation model.

Tritium permeation mechanism is a quite complex process. It involves a complicated reaction mechanism on the surface of the metal and also within the solid structure. On the solid surface recombination and dissociation mechanisms occur as shown in figure 3.5. And within the solid structure trapping, release and diffusion govern the atomic movement.

The simple correlation based permeation model basically ignores these mechanisms and is built based on Sievert's law. Most of the existing tritium analysis codes including THYTAN adopts correlation based permeation equation 3.20 (Ohashi & Sherman, 2007).

$$S_{permeation,i} = M_i \cdot D \cdot \frac{A}{L} \cdot (\sqrt{P \cdot y_i} - \sqrt{P_o \cdot y_{i,o}}) \quad (3.20)$$

However, considering the importance of the phenomena, a more detailed model which considers the surface mechanisms and the mechanisms inside the structure is adopted in the BOTANIC code; diffusion based equilibrium model and non-equilibrium model. The distinction between the equilibrium model and non-equilibrium model is the surface mechanism assumption. If the dissociation rate and recombination rate are assumed identical, the equilibrium model is used. When the rates are considered separately, the non-equilibrium model applies.

The movement across the solid structure is calculated using equation 3.21. The model includes the diffusion equation and the trapping and release equations. The solid surface concentration is calculated using either equilibrium or non-

equilibrium models. When equilibrium situation is assumed the surface concentration is calculated using the Sievert's law in equation 3.22. In the case of non-equilibrium situation, the surface concentration is calculated using equation 3.23. The model considers the atomic flux to the surface and the diffusion rate from the surface (Longhurst, 2004).

*Movement across solid structure*

$$\frac{dC_T}{dt} = -\nabla C_T - \left\{ \frac{a_i C_i^e}{N} \cdot C_T - (a_r + \lambda) \cdot C_T' \right\} \quad (3.21)$$

*Equilibrium surface model*

$$C_T^2 = K_s \cdot P_T \quad (3.22)$$

*Non-equilibrium surface model*

$$\sum_j a_m \left( K_{d_m} P_m - \sum_{i,j} K_{r_m} C_T^2 \right) + DC_T = 0 \quad (3.23)$$

## 3.3 Development of BOTANIC

### 3.3.1 Code features

The necessity of understanding tritium behavior in the VHTR application system has been stressed in the previous chapters. Naturally, a number of tritium codes have been developed including, TMAP, THYTAN, TPAC, etc. However, the existing tritium codes specialize on specific functions. To put in other words, they are capable of performing single function whereas for a complete analysis of

VHTR systems several functions are needed such as chemical process analysis, tritium analysis, system dynamics calculation, etc. The fundamental purpose of this code is to analyze tritium behaviors in VHTR application systems. The comparison of the BOTANIC code and the existing codes have been made as shown in Table 3.1 and 3.2.

The BOTANIC code is developed based on the chemical process code called gPROMS (PSE Limited, 2012). gPROMS is a platform for modeling process industries. It provides modelling interface, user interface creation and Process Model Library. The Process Model Library is composed of commonly used components such as pipe, pump, heat exchanger, etc. The BOTANIC code is developed by implementing necessary tritium models in the associated component models. As the BOTANIC code is developed based on the chemical process code it is capable of analyzing chemical process, process modelling and multi-dimensional tritium analysis.

One of the most distinctive characteristics of BOTANIC is that it does not use a diluted assumption. Diluted assumption is an assumption used when one assumes that tritium level is extremely low, low enough to neglect the effect of tritium generation or loss in the overall physical property. Most of the existing tritium codes use the diluted assumption which results in limitation in the analysis; only low level tritium concentration cases can be analyzed. As BOTANIC reflects the effect of tritium generated or lost in the total system properties, the mentioned limitation does not exist.

Another notable feature of BOTANIC is that it can solve both the lumped and multi-dimensional model. BOTANIC provides complex components such as heat exchanger and reactor as distributed model while other simple components in

lumped model. By composing BOTANIC in an efficient manner, the user can achieve a short calculation time and accurate calculation result at the same time.

Lastly, BOTANIC solves mass and energy conservation equations. It is briefly mentioned that BOTANIC is capable of analyzing system dynamics. This is only possible as it solves the mass and energy conservation equations. The code has the capability to calculate properties such as temperature, mass and physical properties only because it solves the conservation equations. In the conventional tritium codes, only mass conservation equation regarding tritium was solved thus, additional calculations had to be conducted in order to gain the necessary system properties.

### **3.3.2 Code Structure**

The component models in BOTANIC code solve mass and energy conservation equations. And the associated tritium models are implemented and connected to the component models using the source terms. The code structure can be seen in Figure 3.6. As seen in figure, variables such as temperature, pressure and mole fractions are calculated using the mass and energy equations and passed on to the tritium models where tritium generation or loss is solved. The calculated generation or loss of tritium is then reflected back in the mass and energy equations. In the case of BOTANIC code, flow rate is given as the boundary condition. Calculated information is then transferred to the next adjacent component.

## 3.4 Verification of BOTANIC

To achieve code reliability, the BOTANIC code is verified using the analytical solutions. As the BOTANIC code has an Object Oriented Programming (OOP) structure, the code is verified in three step approach as seen in the figure 3.7. Firstly, the physical models are verified using the analytical solutions. Then the components containing the model equations are verified using the benchmark codes and the analytical solutions. Finally, once the physical models and the component models are verified, the system model verification is conducted using the benchmark code calculation results using the Peach Bottom core 2 operation data. The verification calculation cases are summarized in Table 3.3.

### 3.4.1 Individual model verification

Tritium birth models are verified using the Peach Bottom Core 2 operation data. The operation conditions from the Peach Bottom Core 2 are used and the models are verified by comparing the calculation results with the analytical solution and computed solutions of THYTAN. The calculation time is set as 1,550 days (Wichner & Dyer, 1979), the operation time of Peach Bottom Core 2.

Calculation results of BOTANIC show very good agreement with analytical solution as seen in Table 3.4 and 3.5. In the ternary fission model verification case the reported value, analytical solution and the calculation result of BOTANIC are identical as  $4.43 \times 10^{13}$  Bq. And in the case of the  $^{10}\text{B}$  model, the BOTANIC calculation result is identical to that of the analytical solution;  $3.19 \times 10^{12}$  Bq. Verification results of  $^6\text{Li}$  model show very good agreement with the analytical

solution as shown in Table 3.6. The helium model verification results show very good agreement with one of the benchmark code called Tritium Permeation Analyses Code (Oh & Kim, 2009) as seen in Table 3.7.

The BOTANIC tritium leakage model is verified using the benchmark code TPAC. Figure 3.8 illustrates the flowsheet modelling of the leakage verification case. A very simple case where leakage occurs from the primary loop to the containment is used for verification. The containment vessel temperature is given as 323 K and the tritium concentration in the primary loop is assumed to be  $1.98 \times 10^3$  ppb under the reported average temperature of 809 K and 23 atm in the primary coolant (Wichner & Dyer, 1979). The initial tritium concentration in the containment building is assumed to be 0. The leak rate from the primary loop to the coolant and the leak rate from the containment to the atmosphere is assumed as  $4.15 \times 10^{-4}$  1/h. The calculated tritium levels in the containment component using TPAC and BOTANIC are compared in figure 3.9. And as seen in the figure the calculation results show very good agreement with each other.

Purification model is verified using a simple case. The purification system inventory is assumed as  $1 \text{ m}^3$  and the purification efficiency of HT is set as 90 %. The helium flow rate to the purification system is  $1.0 \times 10^{-3} \text{ m}^3/\text{s}$ . And the initial mass fraction of HT is given as  $1.0 \times 10^{-9}$  (Wichner & Dyer, 1979). The flowsheet modelling of purification verification case is as presented in figure 3.10. And as can be seen in figure 3.11, the purification calculation result show very good agreement with the analytical solution.

The simple correlation permeation model is verified using the analytic solution. For the verification process, the heat exchanger component model is used. The heat exchanger verification modelling flowsheet can be observed in

Figure 3.12. The permeation rate calculated using BOTANIC code and the analytical solution are calculated to be identical as seen in Table 3.8.

The Benchmark codes do not provide the multidimensional permeation model and the detailed permeation model. Thus, the multidimensional equilibrium model and the non-equilibrium model is verified using the multi-physics code, COMSOL. Firstly, the surface model is verified. Surface concentration is calculated using the Sievert's law as  $0.009487 \text{ mol m}^{-3}$  in both BOTANIC and COMSOL when the equilibrium constant is assumed as 0.003, pressure 100,000 Pa and mass fraction 0.0001. The wall thickness is given as 2 m and the wall length as 4 m. Wall temperature is calculated using a linear equation and the diffusivity is calculated using the Arrhenius equation. Diffusivity activation energy is given as  $3.74 \times 10^4 \text{ J mol}^{-1}$ . And the jump constant is assumed as  $4.7 \times 10^{-10} \text{ m}$ , trapping energy as 490 J. Calculation results of BOTANIC and COMSOL is shown in figure 3.13 and 3.14. Figure 3.13 is the concentration of tritium at the center of the wall. Figure 3.14 is the tritium distribution across the solid structure at 1000 s. As seen in the figure the calculation results seem to be in good agreement.

### **3.4.2 Total system verification**

The total system verification is conducted based on the Peach Bottom Core 2, operation data (Wichner and Dyer, 1979). Peach Bottom is the first installation of a HTGR in the US. The schematic of the Peach Bottom Reactor can be observed in Figure 3.15. The reactor is simplified and modelled using BOTANIC code as shown in Figure 3.16. The inputs based on the Peach Bottom Core 2 operation

data are listed in Table 3.9. For the verification, minimum scenario, where 310 Ci of tritium is assumed to be released from the reactor core for 1550 days and maximum scenario, where 1203 Ci of tritium is assumed to be released from the reactor core, are simulated. The verification results are displayed in Figure 3.17. Comparisons of tritium concentration in Peach Bottom reactor between the observed concentration and computed solutions of BOTANIC and THYTAN are made. The computed solutions of BOTANIC and analytical solutions of the benchmark code, THYTAN are in good agreement as can be seen in the figure. However, the computed solutions show notable difference compared to the observed tritium concentrations. This is due to the uncertain parameters from the Peach Bottom reactor. The reference operation data lack important information such as graphite surface area, initial grade of graphite, sorption rate etc. Most of the reactor inputs are logically deduced by the researchers. And the release rate from the reactor is simply assumed. Complex mechanisms such as adsorption, absorption, desorption, trapping, etc are not included in the analysis. The difference of the computed result and observed values mainly lie in the lack of information and the neglect of the complex mechanism in the reactor core.

Table 3. 1 Comparison of BOTANIC with existing tritium codes

		<b>TRITGO: 1972 (ORNL)</b>	<b>TMAP 7: 2004 (INL)</b>	<b>TBEC: 2007 (KAIST)</b>	<b>THYTAN: 2007 (JAEA)</b>	<b>TPAC: 2009 (INL)</b>	<b>BOTANIC: 2015 (SNU)</b>
<b>Programming Language</b>		FORTRAN 77 (Text)	FORTRAN (Text)	C (Text)	FORTRAN 90 (Text)	MATLAB (GUI)	gPROMS (GUI)
<b>Process condition, etc.</b>		User input (from other code)			O		
<b>Lumped or distributed Models</b>	<b>Tritium Transport</b>	Lumped (diluted assumption)	Lumped (diluted assumption)	X	Lumped (diluted assumption)	Lumped (diluted assumption)	Lumped (no diluted assumption)
<b>Governing equations</b>	<b>Mass Conservation</b>	X			Both available (lumped/distributed)		
	<b>Energy Conservation</b>	X	Limited (distributed in solid wall)	Limited (distributed in solid wall)	X	X	Lumped and distributed model
<b>Chemical Process Analysis</b>		X	Limited	X	X	X	O
<b>Process optimization</b>		X			O		
<b>Separate Loop</b>		Finite	Infinite	Infinite	Fixed	Infinite	Infinite
<b>Solver</b>		Fixed			Fixed or Variable		Fixed
<b>Application</b>		VHTR Only	Flexible	VHTR Only	VHTR Only	VHTR Only	Flexible

Table 3. 2 Comparison of BOTANIC with existing tritium codes

		<b>TRITGO: 1972 (ORNL)</b>	<b>TMAP 7: 2004 (INL)</b>	<b>TBEC: 2007 (KAIST)</b>	<b>THYTAN: 2007 (JAEA)</b>	<b>TPAC: 2009 (INL)</b>	<b>BOTANIC: 2015 (SNU)</b>
<b>Tritium Generation</b>	<b>Ternary Fission</b>	O	X	O	O	O	O
	<b>Li impurities</b>	O	X	O	O	O	O
	<b>He in coolant</b>	O	X	O	O	O	O
	<b>B in control rod</b>	O	X	O	O	O	O
<b>Tritium Release and Transport in Core</b>		Release fraction	Diffusion model	Diffusion model	Release fraction	Release fraction	Release fraction
<b>Leakage, Purification and Chemisorptions</b>	<b>Leakage</b>	O	X	X	O	O	O
	<b>Purification</b>	O	X	X	O	O	O
	<b>Chemisorptions</b>	O	O	X	X	X	O
<b>Tritium Permeation</b>		Correlation (simplified)	Equilibrium and non- equilibrium models	Fick's law and Sievert's law (distributed model)	Correlation (simplified)	Correlation (simplified)	Equilibrium and non- equilibrium models
<b>Heat Exchanger Model</b>	<b>Temperature Distribution</b>	X	O	X	X	O	O
	<b>Permeation Geometry</b>	Shell-and-Tube Only			Both Shell-and-Tube and PCHE		

Table 3. 3 Verification case summary

Category	Case	Method
Submodel	Mass/Energy Conservation	-
	Tritium Birth (from Ternary, $^6\text{Li}$ , $^7\text{Li}$ , $^{10}\text{B}$ , $^3\text{He}$ )	analytic solution, benchmark code
	Leakage Model	analytic solution
	Purification Model	
	Permeation Model (Correlation Type)	
	Distributed Tritium Transport Model in Solid	benchmark code
Component Model	Pipe/Heater/Cooler Component	analytic solution
	Reactor Component	
	Purification System	
	Heat Exchanger Component	
	Containment Component	
System Model	Peach Bottom Core-2	benchmark code

Table 3. 4 Verification result of ternary fission generation model

Reported Value - Peach Bottom (Wichner and Dyer 1979)		Analytical Solution	Computed Solution from THYTAN (Ohashi and Sherman 2007)	BOTANIC
(Ci)	(Bq)	(Bq)	(Bq)	(Bq)
1,210	$4.43 \times 10^{13}$	$4.43 \times 10^{13}$	$4.42 \times 10^{13}$	$4.437 \times 10^{13}$

Table 3. 5 Verification result of boron generation model

Reported Value (Wichner and Dyer 1979)		Analytical Solution	THYTAN (Ohashi and Sherman 2007)	BOTANIC
(Ci)	(Bq)	(Bq)	(Bq)	(Bq)
85.7	$3.14 \times 10^{12}$	$3.19 \times 10^{12}$	$3.18 \times 10^{12}$	$3.19 \times 10^{12}$

Table 3. 6 Verification result of lithium generation model

Graphite Component	Reported Value (Wichner and Dyer 1979)		Analytical Solution	THYTAN (Ohashi and Sherman 2007)	BOTANIC
	(Ci)	(Bq)	(Bq)	(Bq)	(Bq)
Sleeve	14.0	$5.13 \times 10^{11}$	$5.12 \times 10^{11}$	$5.12 \times 10^{11}$	$5.12 \times 10^{11}$
Spine	1.0	$3.66 \times 10^{10}$	$3.78 \times 10^{10}$	$3.78 \times 10^{10}$	$3.78 \times 10^{10}$
Removal radial reflector	16.4	$6.01 \times 10^{11}$	$5.76 \times 10^{11}$	$5.75 \times 10^{11}$	$5.53 \times 10^{11}$
Permanent radial reflector	18.8	$6.89 \times 10^{11}$	$6.72 \times 10^{11}$	$6.69 \times 10^{11}$	$5.69 \times 10^{11}$
Axial reflector	9.2	$3.37 \times 10^{11}$	$3.42 \times 10^{11}$	$3.42 \times 10^{11}$	$3.42 \times 10^{11}$
Fuel matrix	13.1	$4.80 \times 10^{11}$	$5.68 \times 10^{11}$	$5.68 \times 10^{11}$	$5.67 \times 10^{11}$

Table 3. 7 Verification of helium generation model

Region	Reported Value (Wichner and Dyer 1979)	THYTAN	TPAC	BOTANIC
	(Bq)	(Bq)	(Bq)	(Bq)
Coolant		8.78E+11	1.10E+12	$1.10 \times 10^{12}$
Sleeve Graphite	1.98E+11	1.26E+11	1.58E+11	$1.58 \times 10^{11}$
Removal Radial Reflector	4.95E+11	3.09E+11	3.87E+11	$3.87 \times 10^{11}$
Permanent Radial Reflector	5.68E+11	5.24E+11	5.33E+11	$5.33 \times 10^{11}$
Axial Reflector	1.14E+11	8.86E+10	8.98E+10	$8.98 \times 10^{10}$

Table 3. 8 Verification result of correlation based permeation model

Parameters	Unit	Analytic	BOTANIC
K (Permeability)	$\text{m}^3 \text{m}^{-1} \text{Pa}^{-0.5} \text{s}^{-1}$	1.59E-17	1.58E-17
Permeation rate	m3(STP)/s	9.48E-13	9.31E-13
Permeation rate	kg/s	1.27E-13	1.25E-13

Table 3. 9 System verification inputs (Ohashi & Sherman, 2007)

Variable	Values	
System volume [ $\text{m}^3$ ]	232	
System average temperature [K]	809	
System average pressure [atm]	23	
Total tritium release for 1550 days [Ci]	Maximum scenario : 1203 Minimum scenario 310	
Economizer conditions	Area [ $\text{m}^2$ ]	212
	Outer diameter [m]	6.35E-3
	Inner diameter [m]	4.775E-3
	Inlet temperature [K]	513
	Outlet temperature[K]	593
Evaporator conditions	Area [ $\text{m}^2$ ]	474
	Outer diameter [m]	9.525E-3
	Inner diameter [m]	7.305E-3
	Inlet temperature [K]	593
	Outlet temperature[K]	618
Super heater conditions	Area [ $\text{m}^2$ ]	275
	Outer diameter [m]	9.525E-3
	Inner diameter [m]	6.350E-3
	Inlet temperature [K]	693
	Outlet temperature[K]	853
Concentric duct conditions	Length [m]	7.64
	Outer diameter [m]	0.8064
	Inner diameter [m]	0.7430
Purification system conditions	Efficiency (%)	100
	Mass flow rate 1 [kg/h]	4.54
	Mass flow rate 2 [kg/h]	90.7

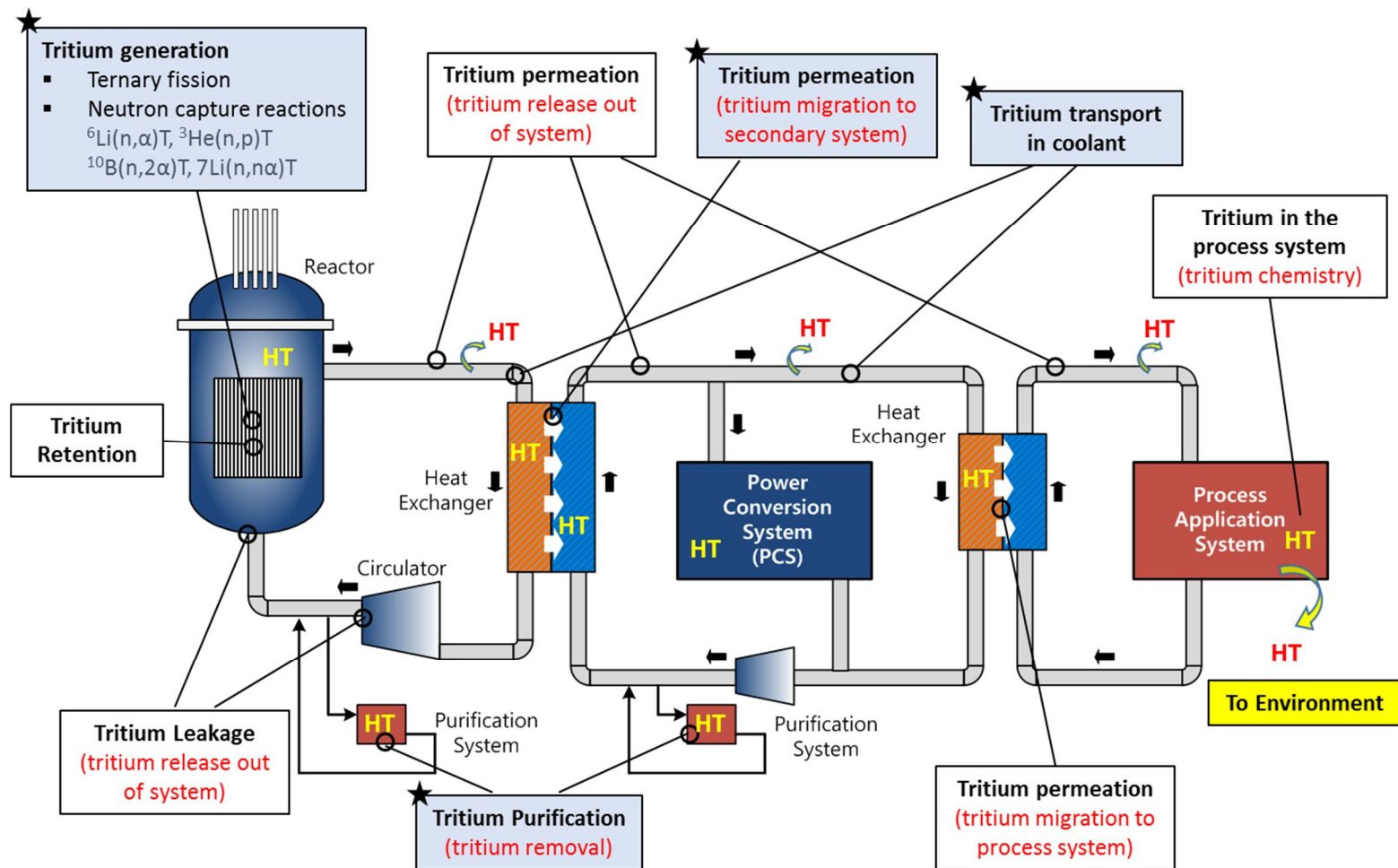


Figure 3. 1 Tritium behavior in VHTR system

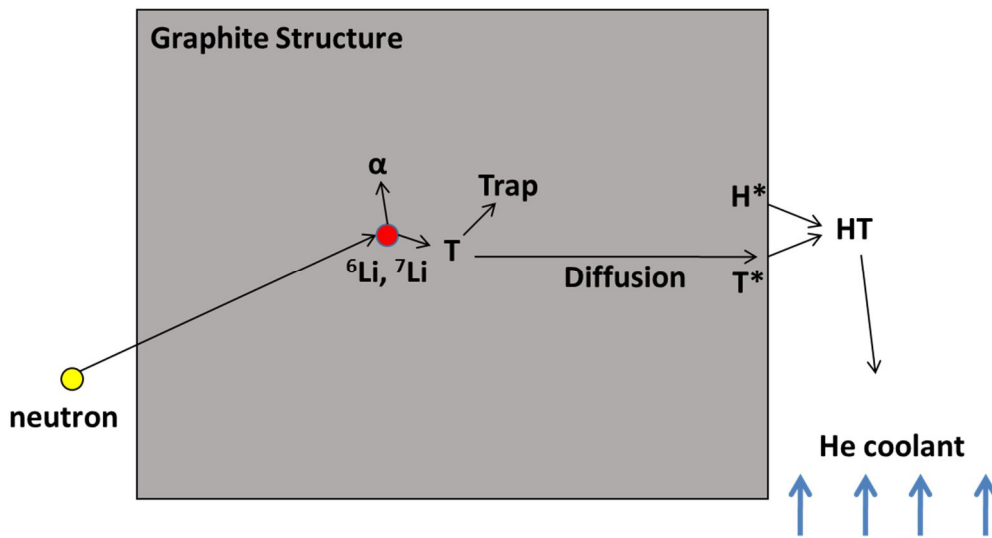


Figure 3. 2 Lithium neutron capture reaction mechanism

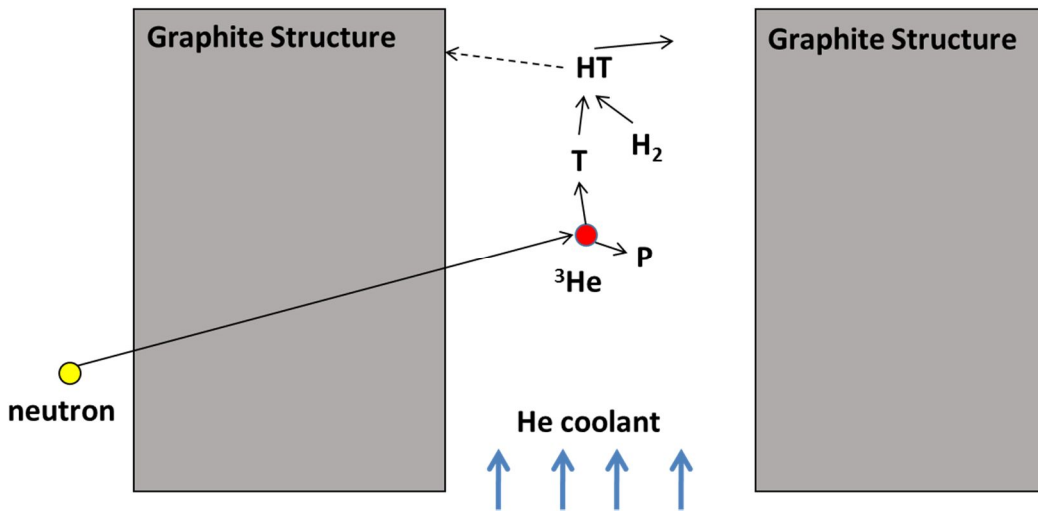


Figure 3. 3 Helium neutron capture reaction mechanism

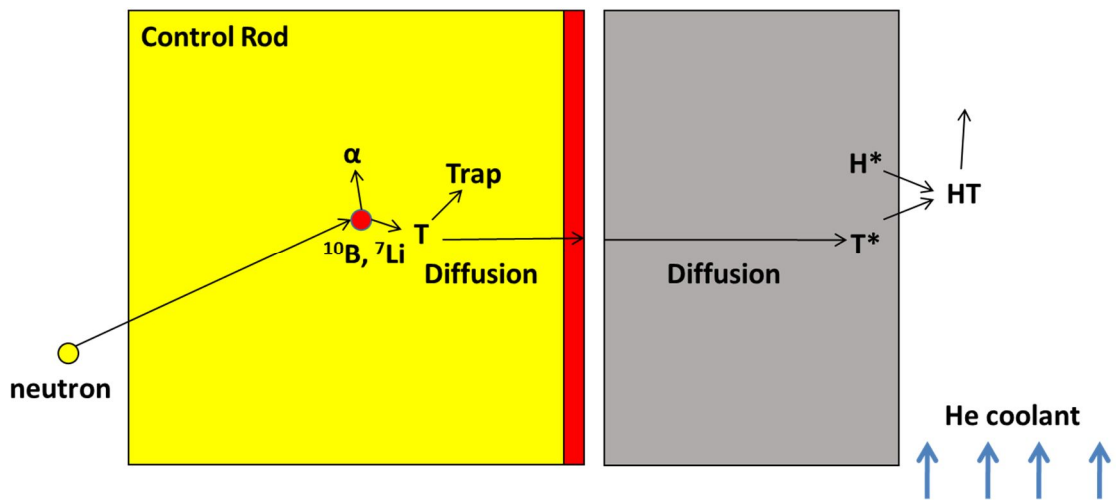


Figure 3. 4 Boron neutron capture reaction mechanism

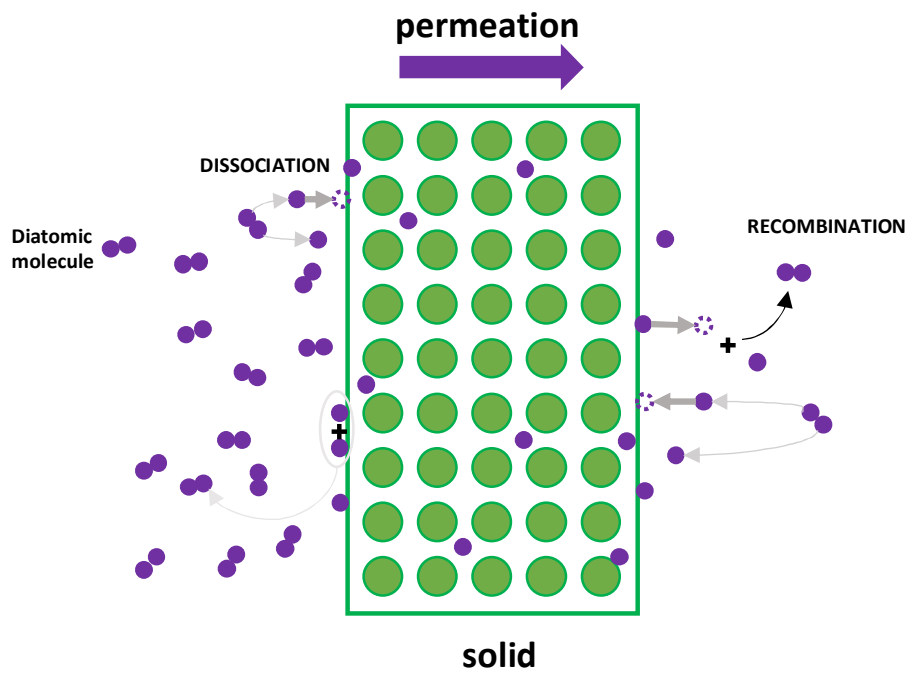


Figure 3. 5 Tritium dissociation and recombination surface mechanisms

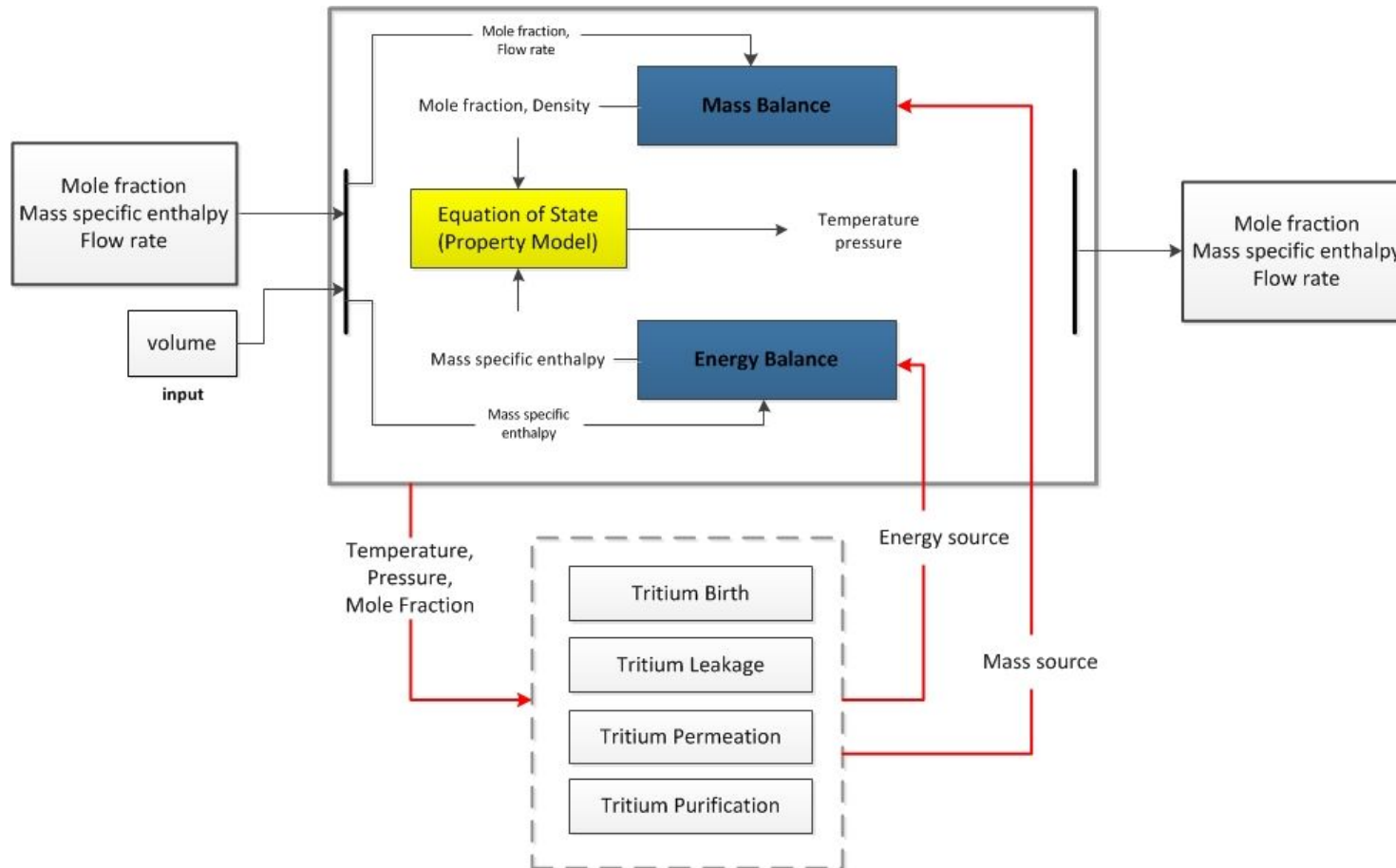


Figure 3. 6 BOTANIC code structure

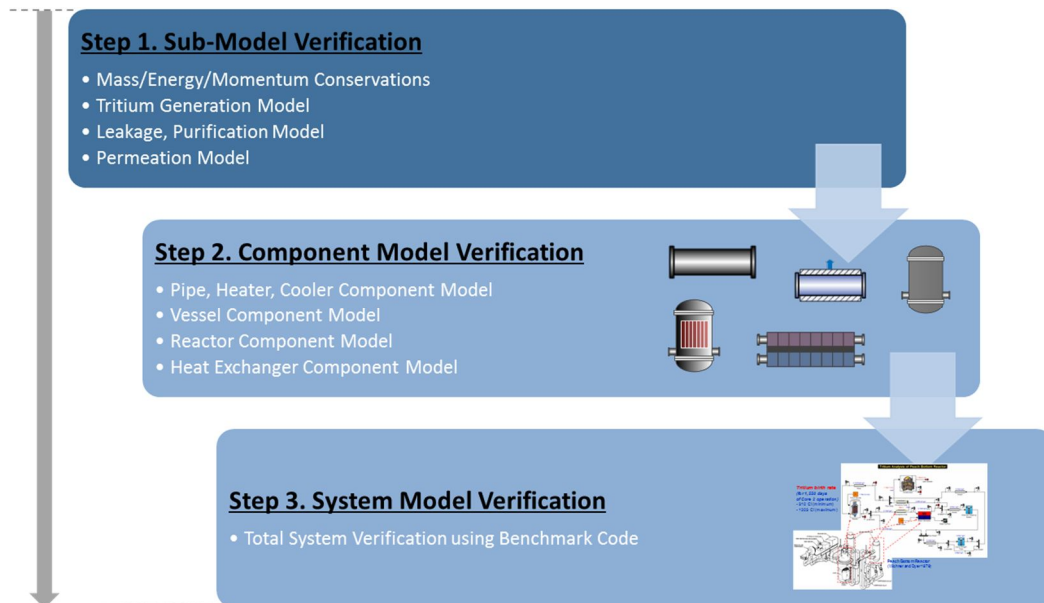


Figure 3. 7 BOTANIC verification procedure

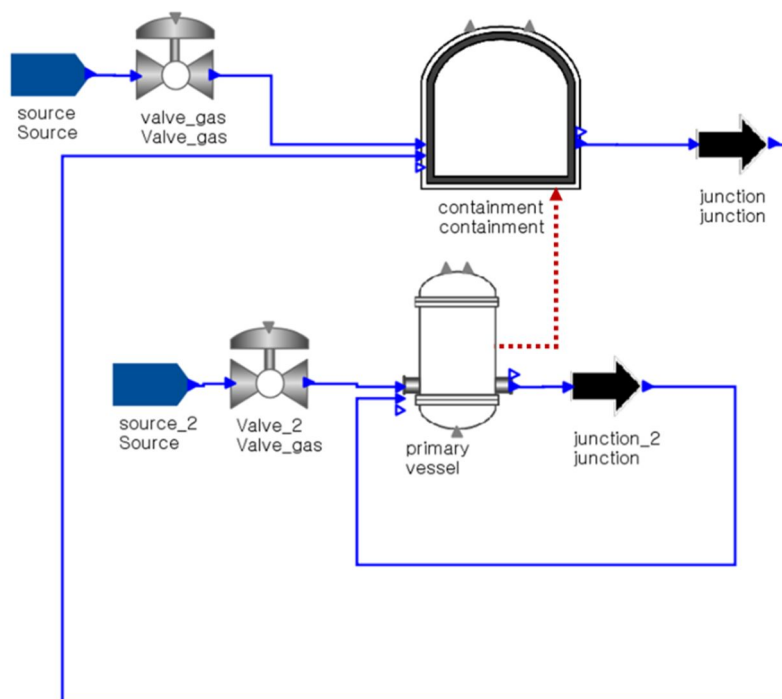


Figure 3. 8 Leakage verification modelling flowsheet on BOTANIC

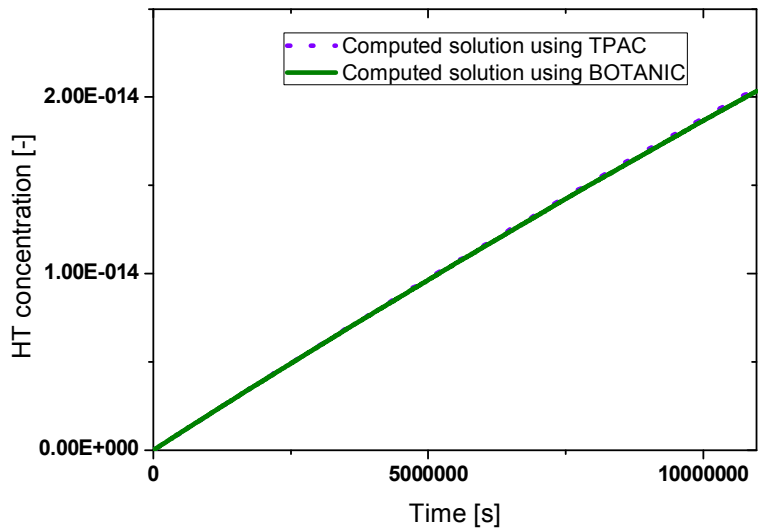


Figure 3. 9 Comparison of leakage calculation results of BOTANIC and TPAC

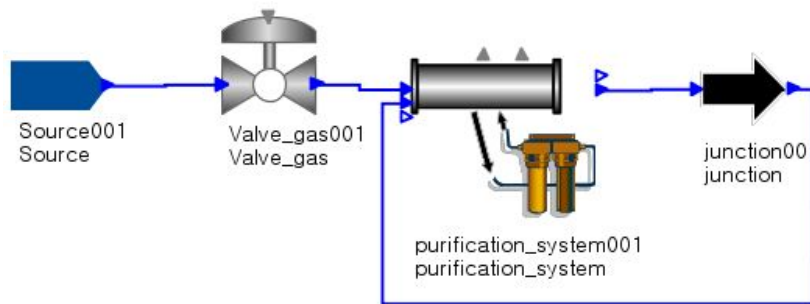


Figure 3. 10 Purification verification modelling flowsheet on BOTANIC

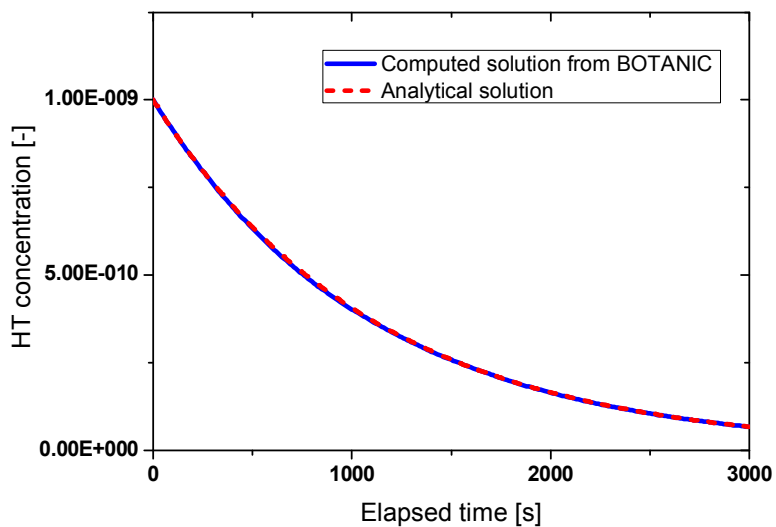


Figure 3. 11 Comparison of purification calculation result of BOTANIC and analytical solution

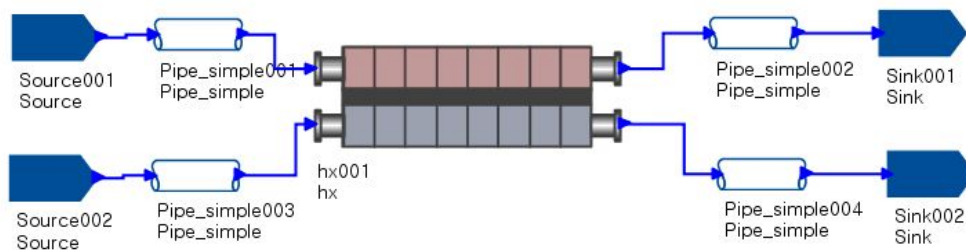


Figure 3. 12 Heat exchanger verification modelling flowsheet on BOTANIC

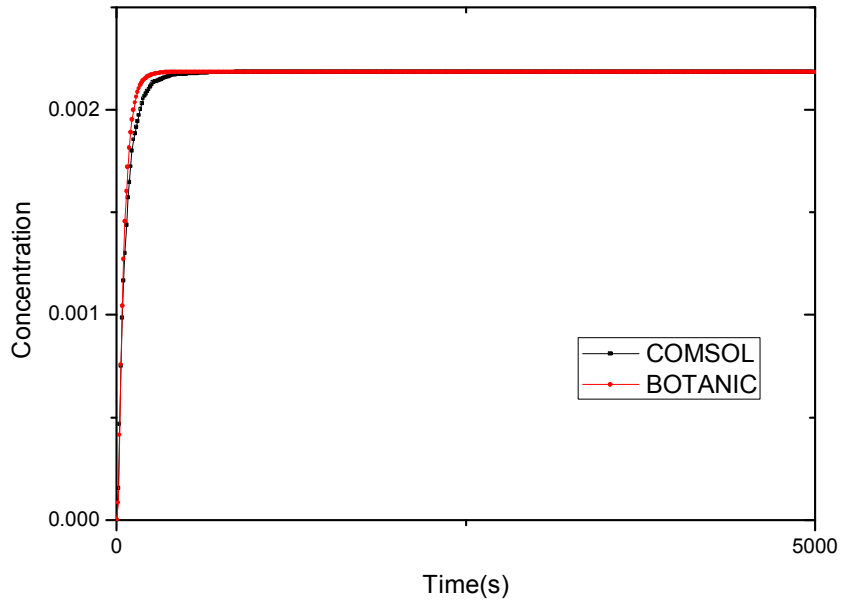


Figure 3. 13 Comparison of the computed tritium concentration at the center of the wall

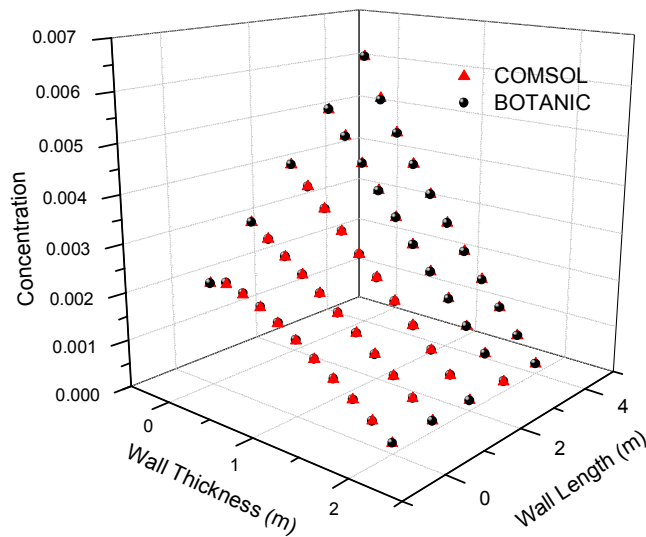


Figure 3. 14 Tritium concentration across the wall at time 1000 s

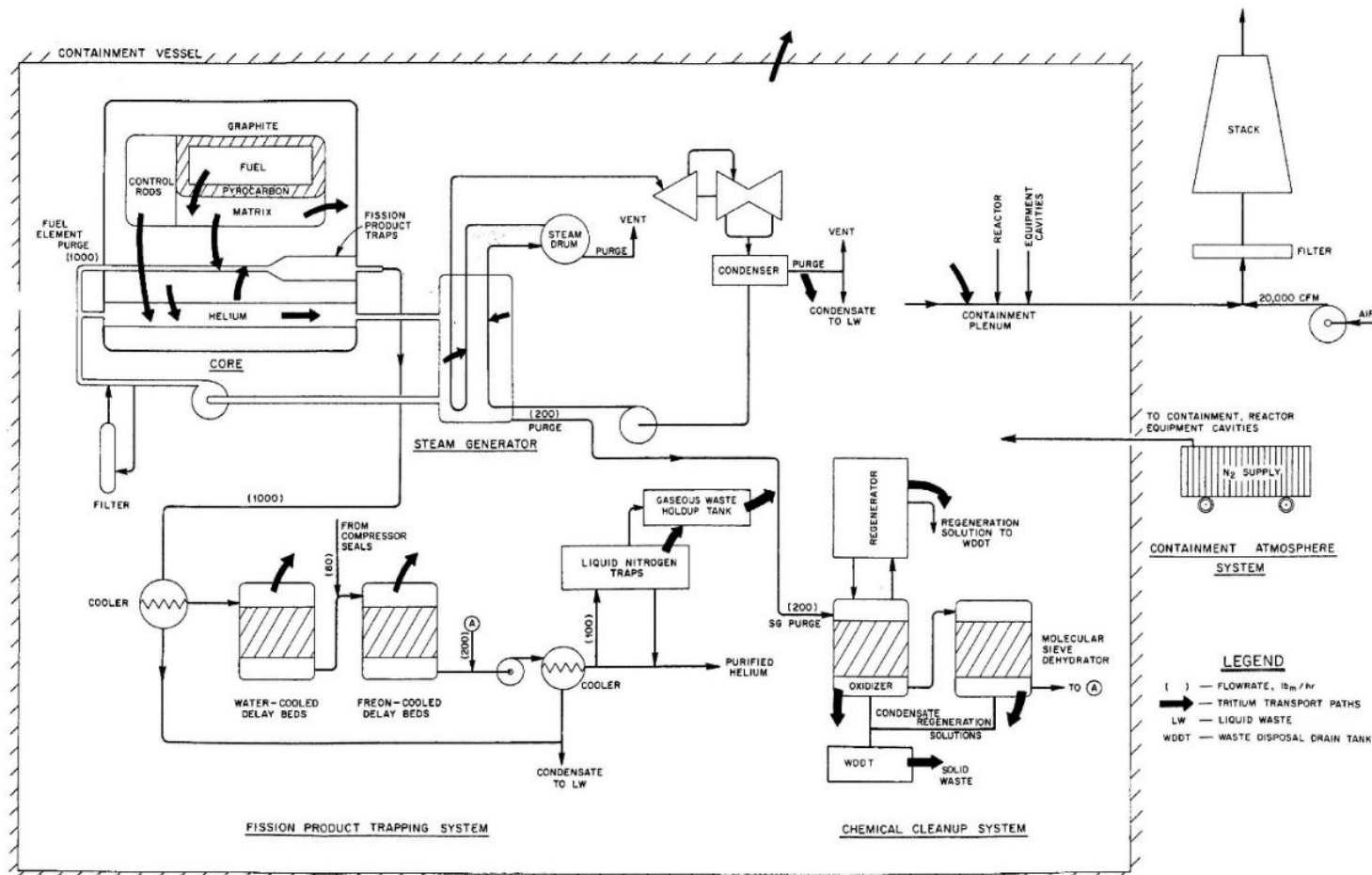


Figure 3. 15 Schematic of the Peach Bottom reactor (Wichner & Dyer, 1979)

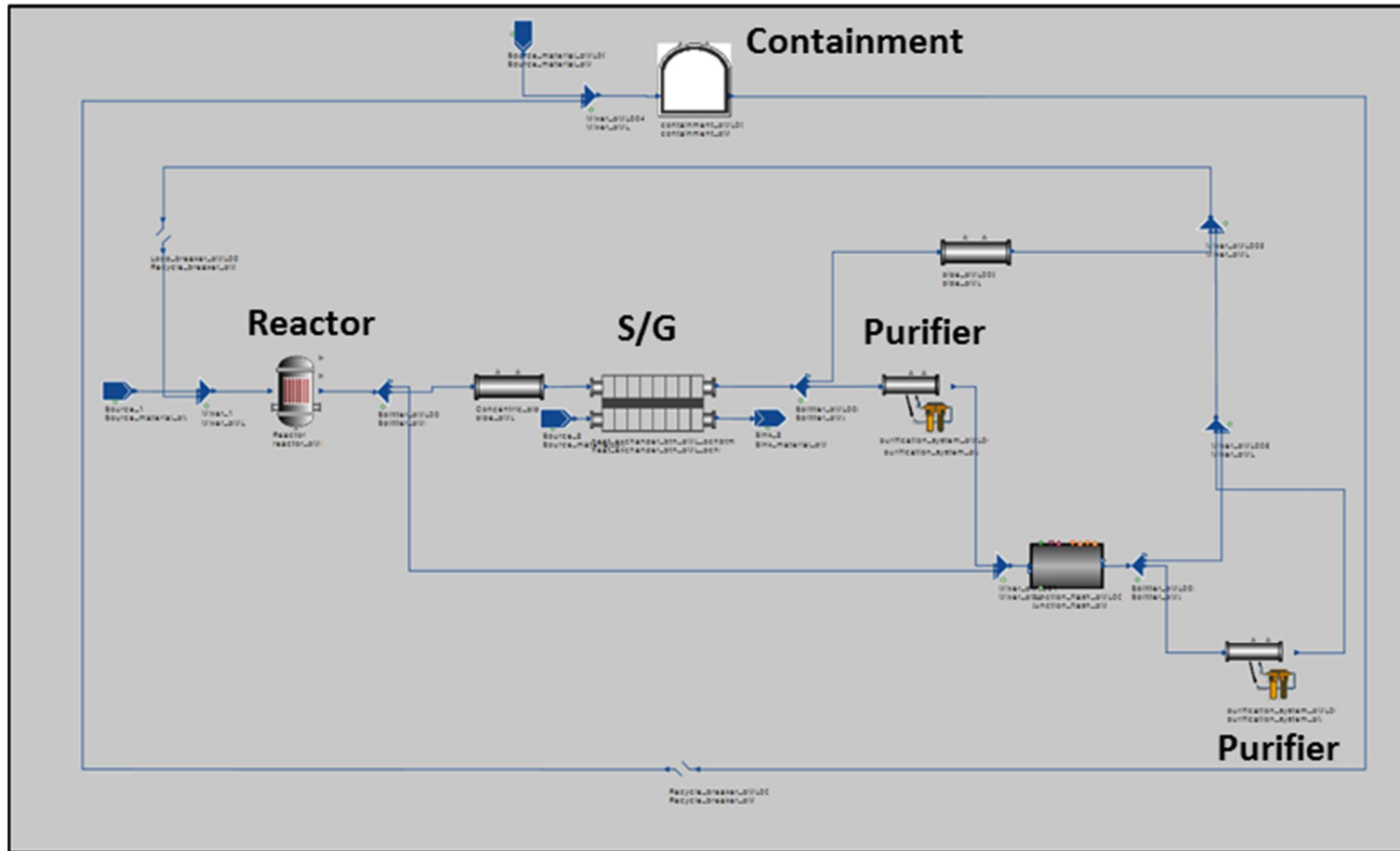


Figure 3. 16 Peach bottom reactor modelling on BOTANIC

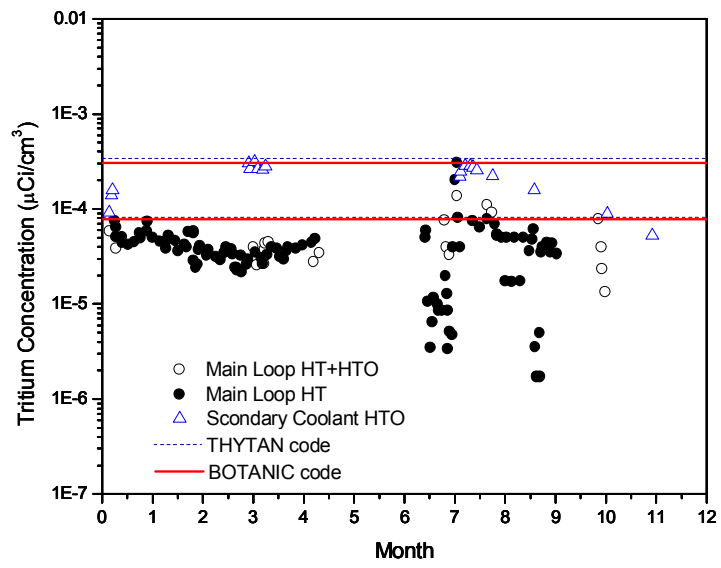


Figure 3. 17 Total system verification result (Ohashi & Sherman, 2007)

## **Chapter 4**

# **Development of Tritium Permeation Model in Printed Circuit Heat Exchanger**

As described in the tritium pathway flowsheet, tritium permeation in the heat exchanger is the main route of tritium to downstream processes. Recent studies show that the most important parameter in predicting tritium behavior in the VHTR system is permeation in the heat exchangers (Kim, 2010). This key phenomena is greatly affected by the temperature and the geometry of the solid structure. VHTR employs printed circuit heat exchanger (PCHE), which possesses a distinctive structure compared to the conventional heat exchangers. PCHE, one of the compact plate type heat exchangers is built by flat metal plates which consist chemically etched semicircle fluid flow channels. The flat metal plates are stacked by diffusion bonding as shown in the figure 4.1. This complex geometry and temperature distribution of the PCHE cause difficulties in predicting tritium permeation behavior. However, existing tritium codes assume uniform wall thickness and utilize the average temperature between hot and cold channels for permeation calculation which can cause errors. In order to perform accurate tritium permeation analysis, a permeation model which accounts PCHE structure and temperature distribution is vital.

## 4.1 3-D Tritium Permeation Modelling in PCHE

### 4.1.1 Assumptions and Conditions

In order to develop a permeation model for tritium movement in PCHE, the tritium permeation in the PCHE is simulated using COMSOL multi-physics code. A simplified 4 channel 3 dimensional PCHE geometry was constructed using CATIA as shown in the figure 4.2. The dimensions of the PCHE was assumed as described in Table 4.1 (Kim & No, 2012). Periodic boundary conditions were assumed as illustrated in the figure 4.3.

In total 447,729 tetrahedral and triangular meshes were built. The average element quality is maintained above 0.7 and the maximum element size for the solid domain and the fluid domain are 1.8E-4 m and 9.85E-4 m, respectively. In order to minimize the mesh associated error, the boundaries are constructed in a denser manner.

For the simulation following assumptions are made; (1) steady-state, (2) helium as coolant, (3) structured steel as the solids structure, (4) tritium surface concentration follows the Sievert's law, (5) tritium concentration of the cold channel assumed as zero, (6) no pressure drop along the channel, (7) counter-current flow and (8) constant mass flowrate.

Following physical models are solved in each domain. For the fluid domain, mass, momentum and energy conservation equations are solved.

*Mass continuity equation*

$$\frac{d\rho}{dt} + \nabla \cdot (\rho u) = 0 \quad (4.1)$$

*Navier stokes equation*

$$\rho \frac{du}{dt} = \rho (u \cdot \nabla) u = \nabla \cdot \left[ -PI + \mu \left( \nabla u + (\nabla u)^T - \frac{2}{3} \mu (\nabla \cdot u) I \right) \right] + F_s \quad (4.2)$$

*Heat equation*

$$\rho C_p \frac{dT}{dt} + \rho C_p u \nabla T = \nabla \cdot (h \nabla T) + Q \quad (4.3)$$

For the solid domain, conduction equation and tritium diffusion model are solved.

*Heat conduction equation*

$$\rho C_p \frac{dT}{dt} = \nabla \cdot (k \nabla T) \quad (4.4)$$

*Diffusion equation*

$$\frac{dC}{dt} + \nabla \cdot (-D \nabla C) + \beta \cdot \nabla C = 0 \quad (4.5)$$

$$D = D_0 \exp \frac{E_{a,D}}{RT} \quad (4.6)$$

And as mentioned, the tritium concentration at the channel surface is calculated using the Sievert's law.

*Sievert's law*

$$C_T = K_s P_m^{1/2} \quad (4.7)$$

$$K_s = S_0 \exp \frac{E_{a,K}}{kT} \quad (4.8)$$

And the detailed conditions applied in the 3-D PCHE tritium permeation simulation model are listed in Table 4.2. Periodic boundary conditions are applied in both heat and diffusion equations.

#### **4.1.2 Results**

As shown in Figures 4.4 and 4.5, the temperature changes in the solid domain are not significant due to the small thermal resistance whereas the concentration changes in the solid domain is significant due to the large diffusion resistance. The permeation route of tritium from hot to cold channel can be seen in Figure 4.6. By the look of the figure, one can intuitively understand that the tritium permeation is influenced by the dimension of the PCHE channels. The route is clearly affected by the diameter of the channel and the vertical distance between the channels.

The dominant tritium permeation path is investigated further. The tritium concentration gradients in x, y and z directions are plotted as shown in the figure 4.7. As seen in the figure, the tritium gradient in the y direction is negligible when compared the tritium gradient in the x and z directions, meaning that there is practically zero tritium diffusion in the y direction. Therefore, from this simulation it was concluded that the tritium permeation along the flow direction, y direction, can be ignored. Based on the conclusion, the model is simplified into 2-dimension.

## **4.2 2-D Numerical Analysis and Parametric Study**

### 4.2.1 Assumptions and Conditions

Based on the 3-D calculation result, the model is simplified in the 2-D permeation model. The fluid domain is reflected as the boundary condition as shown in the Figure 4.8. And for the solid domain, heat conduction equation and the diffusion equation are solved.

*Conduction equation*

$$0 = \nabla \cdot (k \nabla T) \quad (4.9)$$

*Diffusion equation*

$$\nabla \cdot (-D \nabla C) = 0 \quad (4.10)$$

$$D = D_0 \exp \frac{E_{a,D}}{RT} \quad (4.11)$$

The tritium concentration at the surface is given as the boundary conditions. Tritium concentration at the hot channel surface is assumed as  $0.01 \text{ mol m}^{-3}$  and the tritium concentration at the cold channel surface is assumed as 0. Identical diffusivity constants and temperature conditions of the 3-D model is applied for the 2-D model.

### 4.2.2 Grid Sensitivity Study

For reliability, grid sensitivity analysis is conducted using the Grid Convergence Index (GCI) method (Roache, 1997). As seen in Table 4.3, 5 mesh resolutions are used for the GCI analysis. Triangular mesh is utilized and the

number and size of the mesh in each resolutions are listed in the table. In the GCI analysis, 3 sets of grid resolutions are required to determine the values of key variables; p and q.

$$p = \left[ \frac{1}{\ln(r_{21})} \right] \cdot \left[ \ln \left| \frac{\varepsilon_{32}}{\varepsilon_{21}} \right| \right] + q(p) \quad (4.12)$$

$$q(p) = \ln \left( \frac{r_{21}^p - s}{r_{32}^p - s} \right) \quad (4.13)$$

Using the key variables the GCI values are calculated using the following equation.

$$GCI_{fine}^{21} = \frac{Fs \cdot e_a^{21}}{r_{21}^p - 1} \quad (4.14)$$

As seen in the Figure 4.9, the simulated value of tritium concentration at the center (0, 0) shows good convergence as the grid size decreases. And as seen in Figure 4.10, the GCI is significantly reduced down to 0.2 % as the grid size decreases below 0.06 mm<sup>2</sup>. Since the calculation time difference for different grid size resolutions in 2D permeation model is very small, the highest mesh resolution is used for further analysis. Thus, the discretization error from the mesh can be assumed acceptable, around 0.12 %.

### 4.2.3 Parametric Study

The geometric parameters that govern the geometry of the PCHE and the

thermal parameters that govern the thermal distribution across the PCHE structure are identified; diameter ( $d$ ), horizontal distance ( $h$ ), vertical distance ( $v$ ), offset distance ( $o$ ), average temperature ( $T_m$ ) and the temperature difference ( $\Delta T$ ) between the hot and cold channels. The parameters are illustrated in Figure 4.11 and 4.12. For simplicity and scale purpose, the horizontal, vertical distance are normalized by dividing the parameters by the diameter of the channel. The offset distance is normalized by dividing it with the sum of diameter and horizontal distance. Finally, parametric study on the selected parameters are conducted as shown in Table 4.4. In total 116,000 calculations are conducted using COMSOL code.

#### **4.2.4 Results**

In order to clearly see the geometry effect on permeation rate, the calculation results where no temperature difference between the channels exist are investigated.

##### **A. Effect of Vertical Distance**

From the calculation results it was shown that the main tritium transport route is in vertical direction. Therefore, the permeation rate is greatly influenced by the vertical distance. The permeation rate decreases as the vertical distance increases due to the increase in travel distance. The effect of vertical distance is indicated in figure 4.13. When horizontal distance is small, the offset parameter has no influence on the permeation rate. In other words, for small horizontal distance cases, the vertical distance governs the permeation rate. And for large horizontal

distance, greater offset effect can be observed as seen in Figure 4.14. This can be explained by the increase in travel distance as the offset effect applied on the permeation path is proportional to the horizontal distance. The offset distance increases proportionally with the horizontal distance. Thus, for large horizontal distance cases, offset effect is larger. However, even for large horizontal distance cases, the offset effect is negligible for large vertical distance cases as seen in the figure.

### **B. Effect of Horizontal Distance**

For small vertical distance, most of the tritium is permeated in the vertical direction. Permeation through the side pathway is relatively small. However, as the horizontal distance increases permeation through side pathway increases as seen in the Figure 4.15. The change in permeation rate due to increase in side pathway varies depending on the offset parameters as shown in Figure 4.16. For relatively small offset parameters, 0 and 0.1, permeation rate reaches a certain value which is the maximum permeation value as the horizontal distance increases. Meaning that when there is negligible offsets, the permeation rate increases with increasing temperature due to the increase in side pathway permeation until horizontal distance is too large that its increase does not affect the side pathway permeation. And for intermediate offsets, 0.2 to 0.7, the permeation rate reaches the maximum permeation rate and decreases afterwards as the horizontal distance increases. This can be explained by the effect of side pathway permeation and travel distance. Effect of tritium permeation through side pathway dominates in relatively low horizontal distances and the offset effect dominates in the large horizontal distances. This is because offset effect is proportional to horizontal

distance. This effect is visually illustrated in Figure 4.17. Naturally, for large offsets, 0.8 to 0.9, permeation rate decreases as the horizontal distance increases as the offset effect dominates. For large vertical distance, the permeation rate increases with increasing horizontal distance due to the increase in tritium permeation through side pathways. And the offset effects are vaguely expressed as seen in Figure 4.18. Once again the vertical distance between the channels is found to be the most influential geometrical parameter in tritium permeation.

### **C. Effect of Offset**

As seen in the figure 4.19, offset parameter possesses very small influence on the permeation rate for small horizontal distance. The permeation rate is dominated by the vertical distance effect. As mentioned earlier, the offset effect is proportional to the horizontal distance. And for large horizontal distance, the offset effect can be observed for small and intermediate offsets as seen in Figure 4.20. However, for large vertical distance the offset effect is hardly noted.

To summarize, tritium permeation increases as the vertical distance decreases and the horizontal distance increases. The increase in vertical distance increases the travel distance and the increase in horizontal distance increases the side pathway permeation. For small horizontal distance, only vertical distance affects the tritium permeation rate. And for large horizontal and vertical distance both horizontal and vertical distances affect tritium permeation. The offset effect is proportional to horizontal distance and is dominant for large horizontal distance and small vertical distance cases. The summarized result is displayed in Figure 4.21.

## 4.3 Tritium Permeation Model for PCHE

As described in the previous section, the geometry of the PCHE and the temperature distribution have significant influence on tritium permeation. Thus, a permeation model which reflects the geometry and temperature distribution of the PCHE is vital. The permeation model which accounts both geometric effect and thermal effects is developed. The geometric effect is designed to be reflected in the shape factor and the thermal effect is designed to be reflected in the diffusivity. From the numerical analysis results, it is found that the tritium permeation path between the PCHE channels can be divided into two paths as shown in Figure 4.22. This study proposes to develop a tritium permeation model in which permeation resistance through the two paths are connected in parallel. The direct vertical tritium permeation path will be noted as path-1 and the tritium permeation path through sideway will be noted as path-2.

### 4.3.1 Shape Factor

#### A. Permeation model for path-1

Ideally, the effect of tritium permeation in path-2 can be eliminated as the horizontal distance decreases. For extremely small horizontal distance, only path-1 tritium permeation exists as can be seen in the Figure 4.23. And for path-1, when assuming no offset exists, only vertical distance influences the tritium permeation rate. The shape factor  $S_1$  is defined as follows.

$$S_1 = \frac{A_{eff,1}}{L_{eff,1}} \quad (4.15)$$

where  $A_{eff,1}$  represents the effective permeation surface area and  $L_{eff,1}$  represents the effective length between the hot and cold channels. The effective area is simply defined as  $2d$ , where  $d$  represents the diameter. This seems reasonable as the surface area of the channel increases proportionally to the channel diameter. Furthermore, one can easily predict that the effective length between the two channels must be equal or larger than the shortest distance between the channels,  $v$ , and smaller than the largest distance between the channels,  $v+0.5d$ . Thus the effective length is defined as  $L_{eff,1} = v + a \cdot d$  and the value of alpha ( $a$ ) is calculated using the numerical solutions of COMSOL.  $a$  is calculated to be 0.058. Thus, the Shape factor-1 is defined as follows.

$$S_1 = \frac{2d}{v + 0.058 \cdot d} \quad (4.16)$$

For verification the newly defined Shape factor-1, the analytical solutions calculated using shape factor-1 are compared with the reference numerical solutions as shown in the Figure 4.24. As seen in the figure, the analytical solutions using the newly developed shape factor show very good agreement with the reference numerical solutions. Whereas the analytical solutions calculated using the existing permeation model show notable error.

### **B. Permeation model for path-2**

For large horizontal cases, tritium permeation through side pathway exists, thus influences the total permeation rate. According to the numerical analysis

results, offset effect is found negligible for large horizontal distance and vertical distance. And the results showed that the permeation rate through path-2 was affected by both horizontal distance and vertical distance. Thus, shape factor for permeation path-2 when there is no offset is developed in terms of horizontal distance and vertical distance.

From the schematic of the PCHE channels one can assume that the effective permeation area of path-2 is proportional to horizontal distance. Thus, the effective permeation area is assumed as follows;  $A_{eff,2} \sim h$ . And the effective length between the channel is designed to satisfy following conditions.

1. When horizontal distance reaches 0, the effective length reaches vertical distance.
2. When vertical distance reaches 0, the effective length is proportional to horizontal distance.
3. When vertical distance and horizontal distance increases the effective length increases.
4. Effective length is a distance parameter, thus, distance dimension is preferred.

Based on the described conditions, the effective length,  $L_{eff,2} \sim (v^n + C_2 \cdot h^n)^{\frac{1}{n}}$ , is proposed. Thus, the shape factor 2 is suggested as follows.

$$S_2 = \frac{A_{eff,2}}{L_{eff,2}} = C_1 \cdot \frac{h}{(v^n + C_2 \cdot h^n)^{1/n}} \quad (4.17)$$

And from the numerical calculation results, the shape factor-2 is calculated for various normalized vertical distance and normalized horizontal distance as shown

in the Table 4.5. Furthermore, the coefficients of the suggested shape factor-2 are obtained iteratively using the obtained numerical values of shape factor 2 as shown in the figure 4.25. The proposed model shows good agreement with the numerical data for  $C_1 = 1.7$ ,  $C_2 = 1.2$  and  $n = 1.6$ .

The proposed shape factor 1 and shape factor 2 are verified by comparing the analytical solutions calculated using the developed shape factors with the reference numerical solutions. As seen in the figure 4.26, the proposed model show good agreement with the reference numerical solutions, whereas the analytical solutions calculated using the existing permeation model show significant difference from the numerical solutions.

*Proposed model*

$$R = S_1 \cdot D \cdot \Delta C + S_2 \cdot D \cdot \Delta C \quad (4.18)$$

*Existing model*

$$R = S \cdot D \cdot \Delta C \quad (4.19)$$

$$S = \frac{d + 0.5\pi d}{v + 0.25d} \quad (4.20)$$

### **C. Effective vertical distance**

In the previous sections, the offset effect are neglected. Offset influences the travel distance of tritium. In other words, the offset affects the effective length between the channels. In order to reflect the offset effect, effective vertical distance is newly defined and used in shape factor 1 and 2. The effective vertical distance is to satisfy following conditions.

1. The effective vertical distance must converge to vertical distance, when

offset parameter reaches 0.

2. The offset effect is proportional to horizontal distance. As the horizontal distance reaches 0 the offset effect must reach 0.
3. Vertical distance is a length parameter, thus, length dimension, meter, is preferred.

Based on the listed conditions, the effective vertical distance is newly suggested as follows. Using the numerical calculation result, the coefficients are obtained through iterations;  $C_3 = 1.2$  and  $n_2 = 3$ .

$$v_{eff} = \left( v^{n_2} + (C_3 \cdot o_{nor} \cdot h)^{n_2} \right)^{1/n_2} \quad (4.21)$$

Finally the developed model is verified using the reference numerical solutions. The analytical solutions calculated using the shape factor 1 and 2 together with effective vertical distance are compared with the COMSOL reference numerical solutions as shown in Figure 4.27. The model agrees well and thus, it can be concluded that the developed model is verified. And as can be seen in the figure, the existing permeation model underestimates the permeation rate significantly.

### 4.3.2 Effective Diffusivity

The thermal effect significantly influences the diffusivity in tritium permeation. In order to consider the thermal effect, an effective diffusivity concept has been applied. Since the effective diffusivity is developed for a slab

(Park, 2015), a correction factor is applied to be used in the PCHE geometry. The correction factor is obtained by fitting the reference numerical solutions.

*Effective diffusivity for plate*

$$D_{eff,plate} = D_0 \exp\left(\frac{-E_{a,D}}{RT_{eff}}\right) \quad (4.22)$$

*Effective temperature*

$$T_{eff} = x_{eff} \cdot T_1 + (1 - x_{eff}) \cdot T_2 \quad (4.23)$$

$$x_{eff} = 0.5 + (C_{1,D} + C_2 \cdot E_{a,D} + C_{3,D} \cdot T_m + C_{4,D} \cdot E_{a,D} \cdot T_m) \cdot \Delta T \quad (4.24)$$

*Effective diffusivity for PCHE*

$$D_{eff,PCHE} = \frac{1}{2.3^{\frac{\Delta T}{\Delta T + 0.1}}} \cdot D_{eff,plate} \quad (4.25)$$

### 4.3.3 Verification of the Developed Model

The final model for tritium permeation in PCHE has the capability to consider the geometrical effect and thermal effect. The geometrical effect is reflected in the shape factors and the thermal effect is reflected in the diffusivity. The final form of the PCHE permeation model is shown in Figure 4.28.

Finally, the analytical solutions of the existing permeation model and the developed PCHE model have been compared with the reference numerical solutions. As seen in the Figure 4.29, the existing model greatly under predicts the permeation rate when there is no temperature difference between the channels and over predicts when temperature gradient is present. Whereas the analytical

solutions of the newly proposed PCHE model agree well with the reference numerical data, within  $\pm 20\%$ .

Table 4. 1 Reference geometry dimensions (Kim, 2009)

<b>Geometrical parameter</b>	<b>Value</b>
Diameter	1.51 mm
Pitch length	24.6 mm
Horizontal distance between channels	1.11 mm
Vertical distance between channels	0.706 mm
Pitch angle	15°
Hydraulic diameter	0.922 mm

Table 4. 2 Conditions of the 3-D COMSOL PCHE permeation model

<b>Parameter</b>	<b>Conditions</b>
Hot channel inlet temperature	1000 K
Cold channel inlet temperature	300 K
Pressure	1 atm
Hot/cold channel velocity	1 m/s
Permeation Coefficient	$1.38 \times 10^{-7} \cdot e^{\left(\frac{-57500}{8.314 \cdot T}\right)}$
Tritium concentration in hot channels	0.01 mol/m <sup>3</sup>
Tritium concentration in cold channels	0 mol/m <sup>3</sup>
Initial tritium concentration in the solid	0
Material (solid domain)	Steel
Material (fluid domain)	Helium

Table 4. 3 Grid resolutions used for GCI analysis

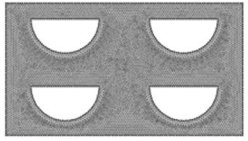
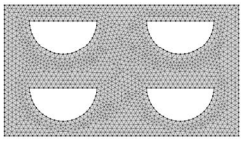
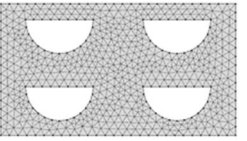
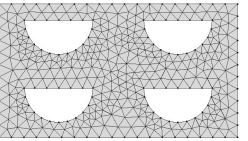
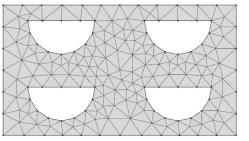
					
<b>Mesh</b>	Extremely fine	Extra fine	Finer	Fine	Coarse
<b>Mesh area</b>	11.72 mm <sup>2</sup>				
<b>Number of mesh</b>	12712	3248	1052	634	271
<b>Mesh size</b>	0.0304	0.0602	0.1057	0.1361	0.2056

Table 4. 4 Geometric and thermal parameter values for parametric study

$h_{nor} = \frac{h}{d}$	$v_{nor} = \frac{v}{d}$	$o_{nor} = \frac{o}{d+h}$	$a$	$dT/T1$
0.5	0.5	0.0	0	0
0.65	0.65	0.1	30	0.05
0.8	0.8	0.2	60	0.1
0.95	0.95	0.3	90	0.15
1.1	1.1	0.4	120	0.2
1.25	1.25	0.5	450	0.25
1.4	1.4	0.6	480	0.3
1.55	1.55	0.7	510	0.35
1.7	1.7	0.8	540	0.4
1.85	1.85	0.9	570	0.45
-	-	-	-	0.5
-	-	-	-	0.55

Table 4. 5 Calculated Shape factor 2 values for various v/d and h/d

$\begin{matrix} v/d \\ h/d \end{matrix}$	0.5	0.65	0.8	0.95	1.1	1.25	1.4	1.55	1.7	1.85
0.001	0	0	0	0	0	0	0	0	0	0
0.5	0.998	0.878	0.781	0.702	0.635	0.579	0.530	0.490	0.455	0.424
0.65	1.151	1.032	0.931	0.846	0.775	0.713	0.657	0.610	0.568	0.531
0.8	1.254	1.143	1.045	0.961	0.887	0.823	0.765	0.714	0.669	0.627
0.95	1.320	1.220	1.130	1.049	0.977	0.913	0.855	0.806	0.756	0.712
1.1	1.361	1.272	1.191	1.115	1.048	0.985	0.929	0.878	0.830	0.786
1.25	1.388	1.308	1.233	1.165	1.102	1.043	0.989	0.939	0.893	0.849
1.4	1.402	1.331	1.264	1.201	1.143	1.088	1.037	0.989	0.944	0.903
1.55	1.410	1.345	1.283	1.226	1.173	1.123	1.075	1.030	0.987	0.947
1.7	1.417	1.356	1.300	1.247	1.198	1.152	1.107	1.064	1.023	0.985
1.85	1.417	1.359	1.307	1.259	1.214	1.171	1.130	1.090	1.052	1.015

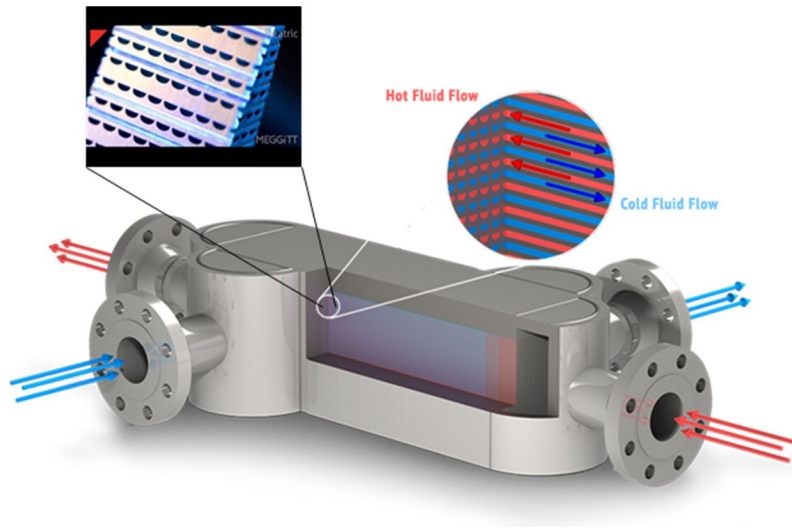


Figure 4. 1 Schematic of the PCHE (Vacuum Process Engineering, 2016)

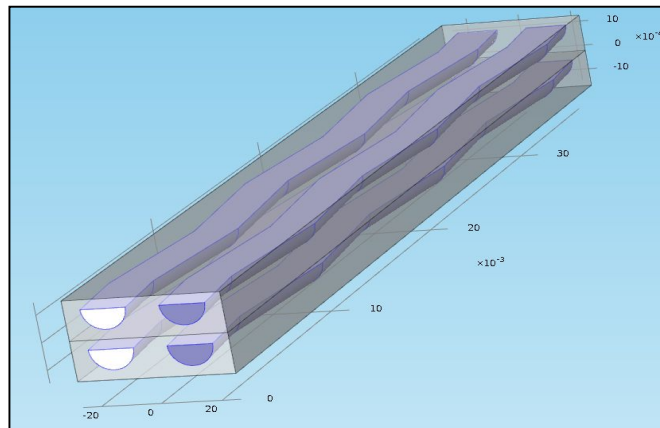


Figure 4. 2 PCHE geometry built using CATIA

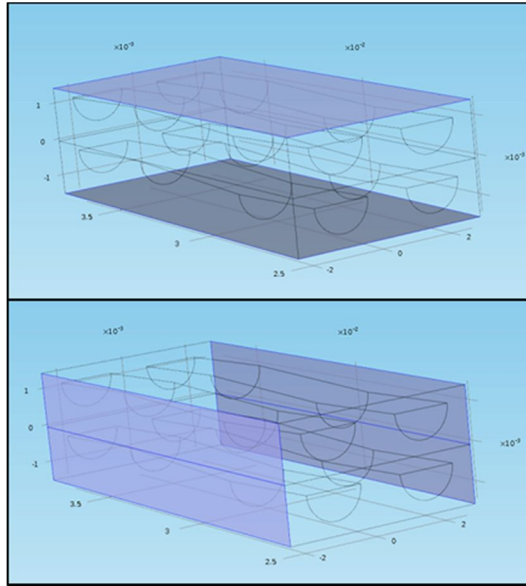


Figure 4. 3 Periodic boundaries

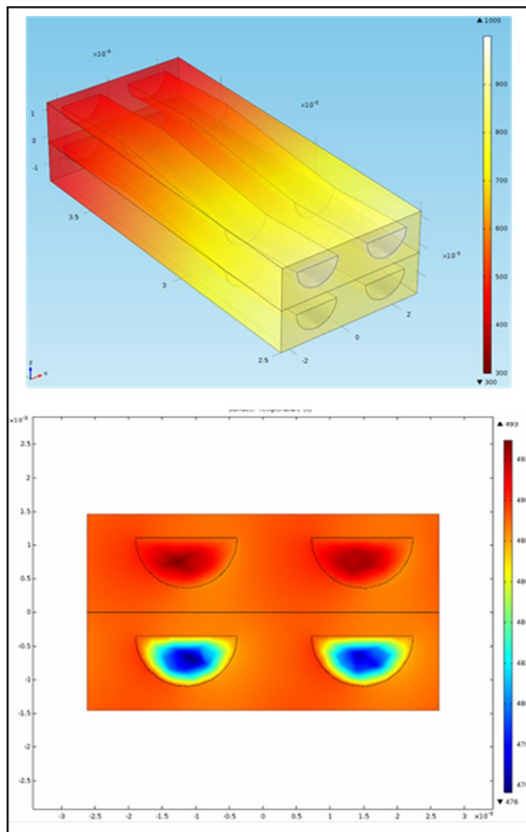


Figure 4. 4 Temperature profile

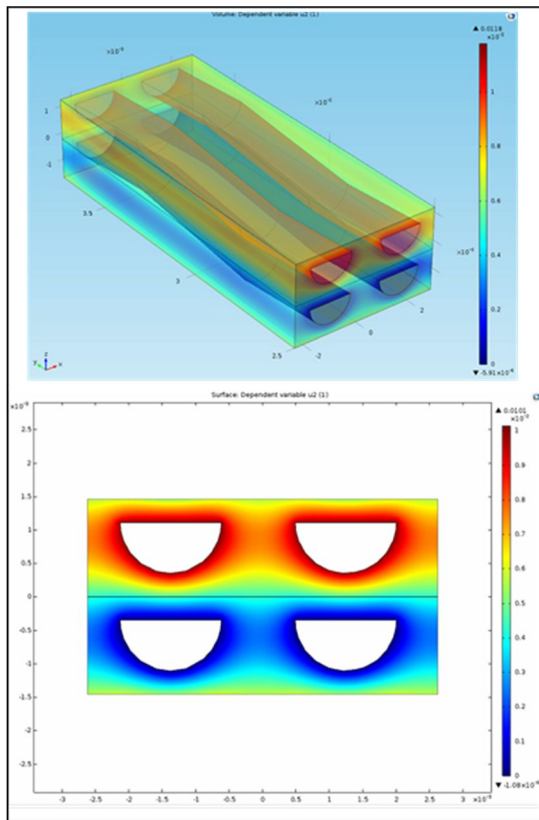


Figure 4. 5 Tritium concentration profile

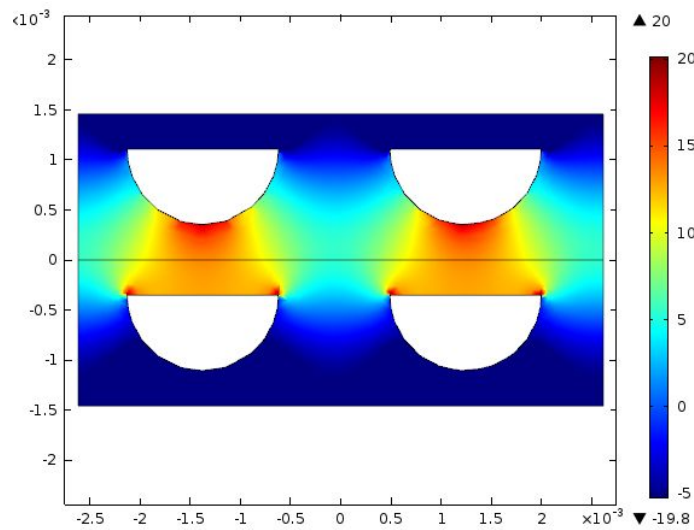
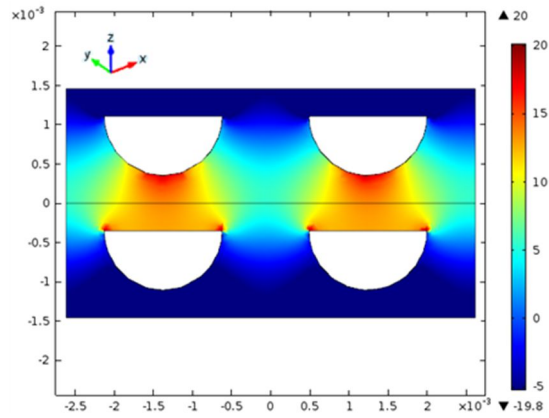
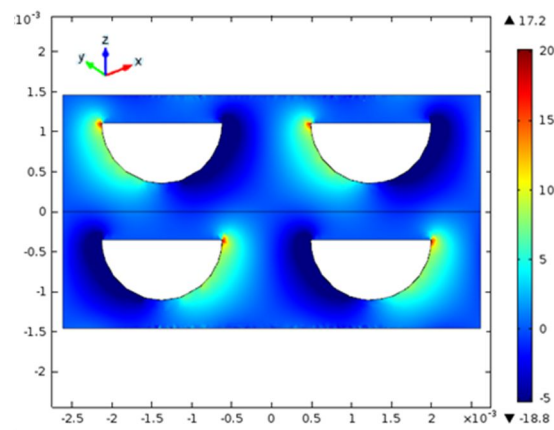


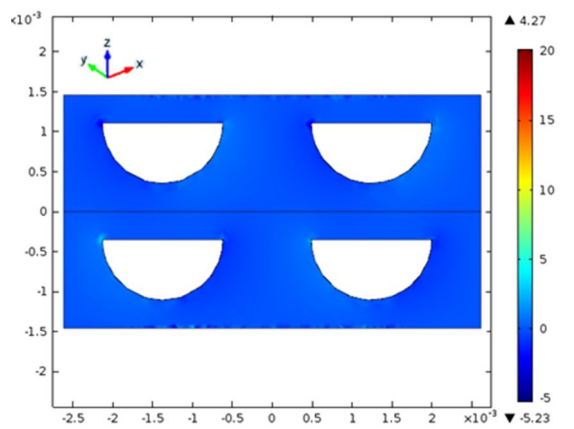
Figure 4. 6 Tritium permeation route



1. Gradient in z direction



2. Gradient in x direction



3. Gradient in y direction

Figure 4. 7 Tritium gradient in z, x, and y directions

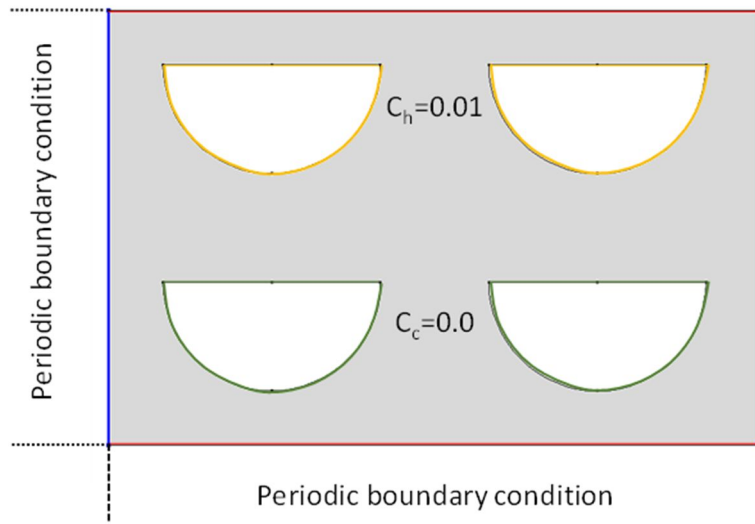


Figure 4. 8 Schematic and conditions of the 2-D PCHE model

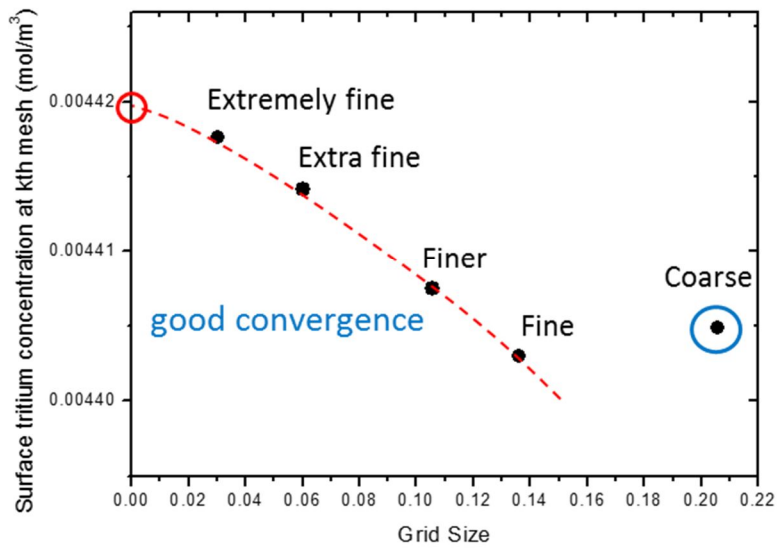


Figure 4. 9 Grid size effect on calculation result

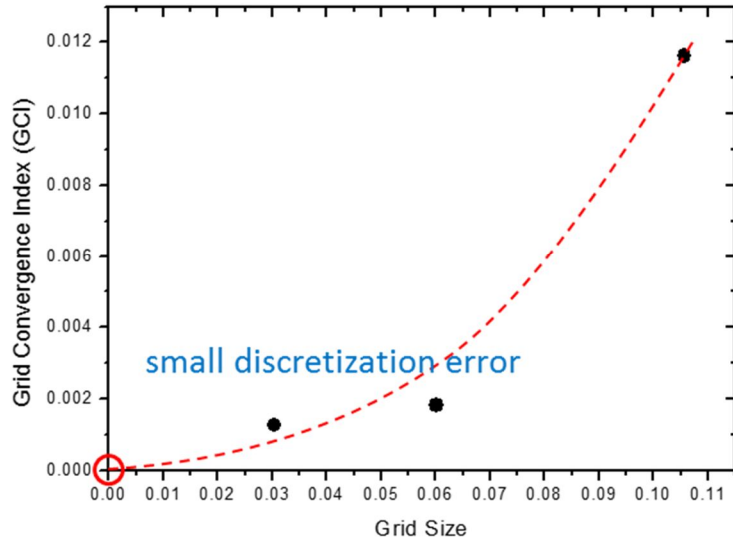


Figure 4. 10 Grid size effect on discretization error

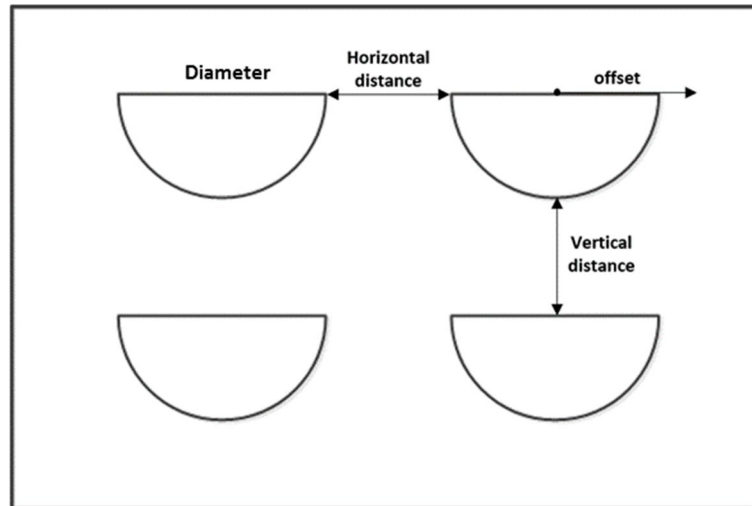


Figure 4. 11 Geometrical parameters of the PCHE

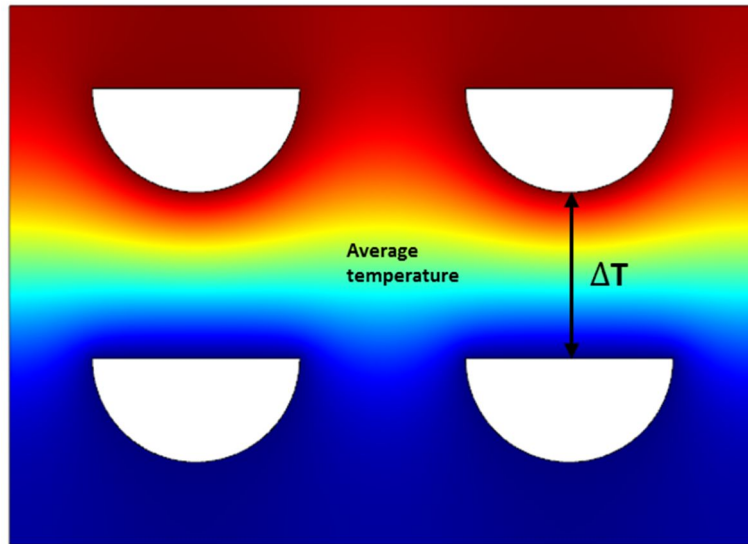


Figure 4. 12 Thermal parameters of the PCHE

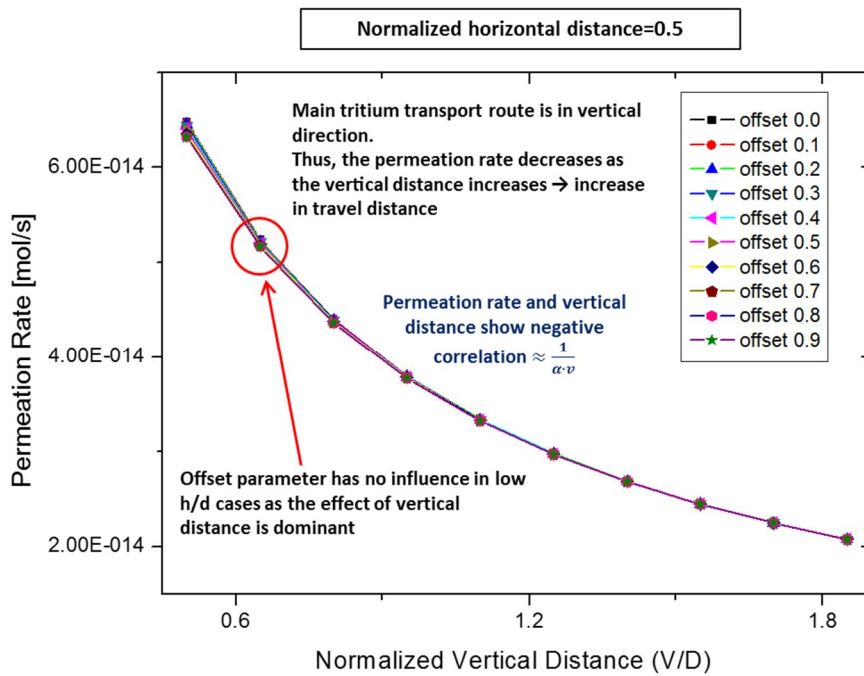


Figure 4. 13 Effect of vertical distance (h=0.5)

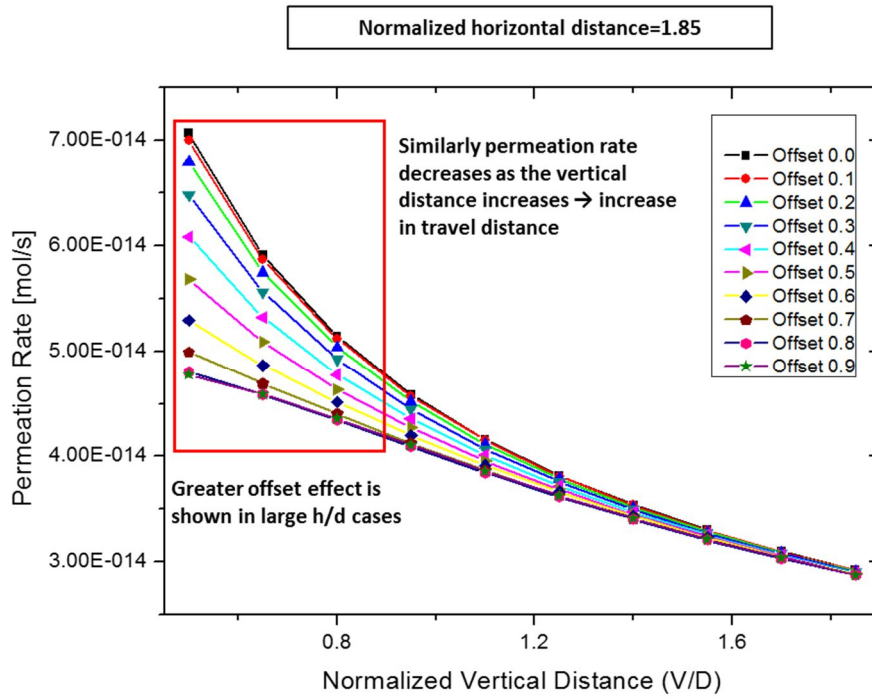


Figure 4. 14 Effect of vertical distance ( $h=1.85$ )

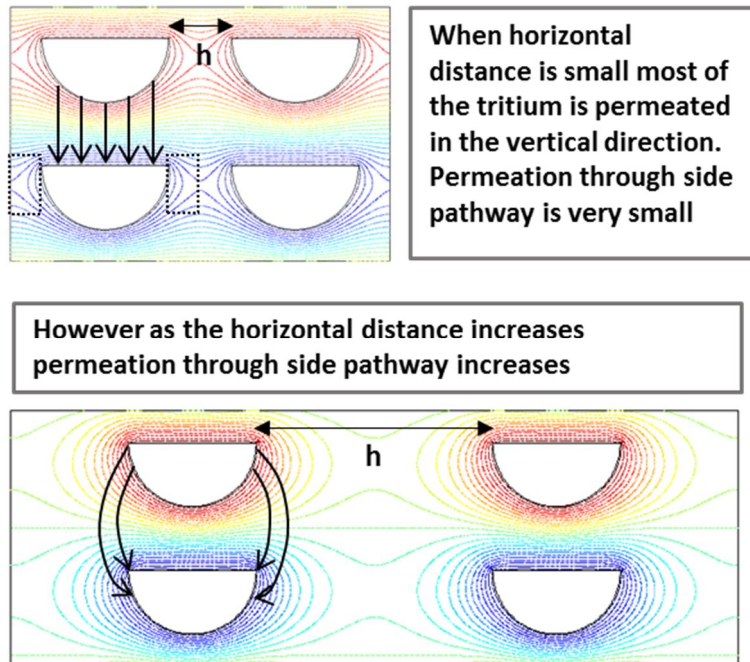


Figure 4. 15 Increase of side permeation due to increase of horizontal distance

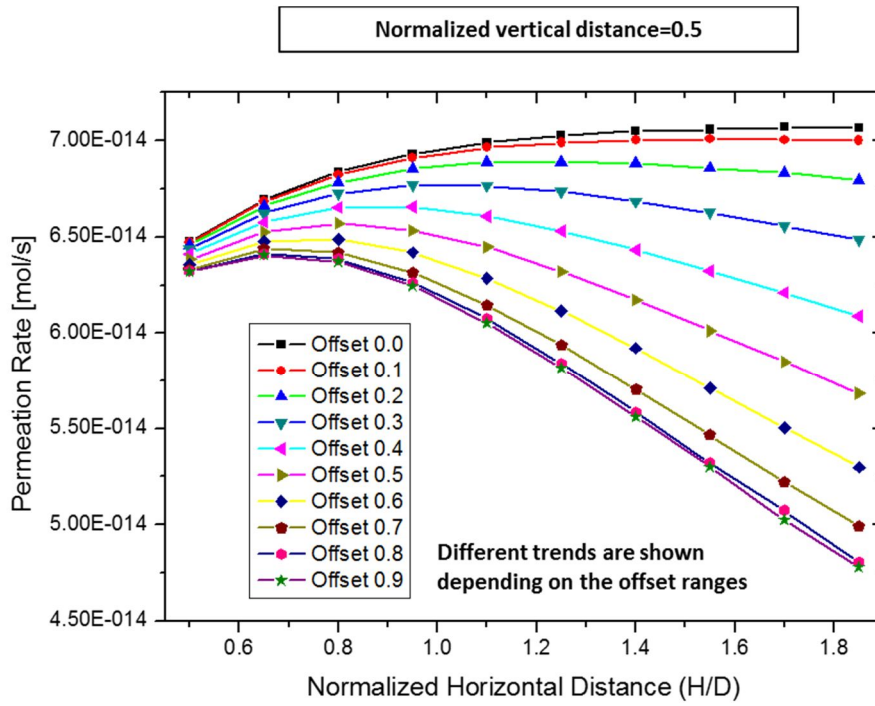


Figure 4. 16 Effect of horizontal distance ( $v=0.5$ )

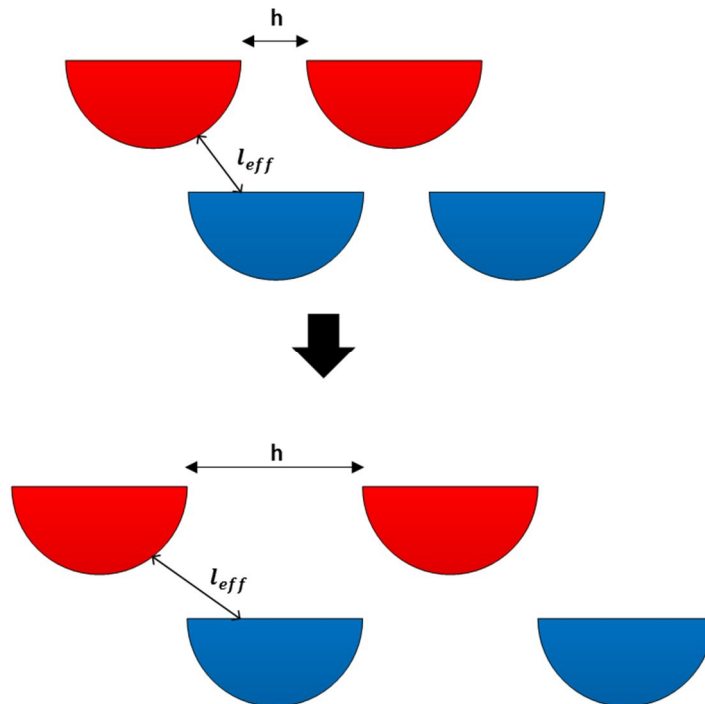


Figure 4. 17 Horizontal distance effect on offset

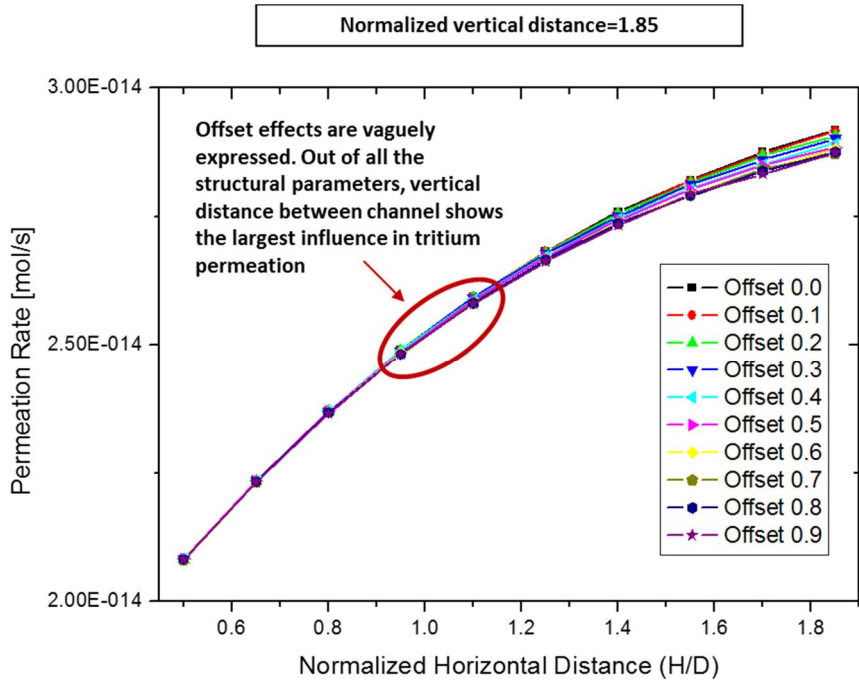


Figure 4. 18 Effect of horizontal distance ( $v=1.85$ )

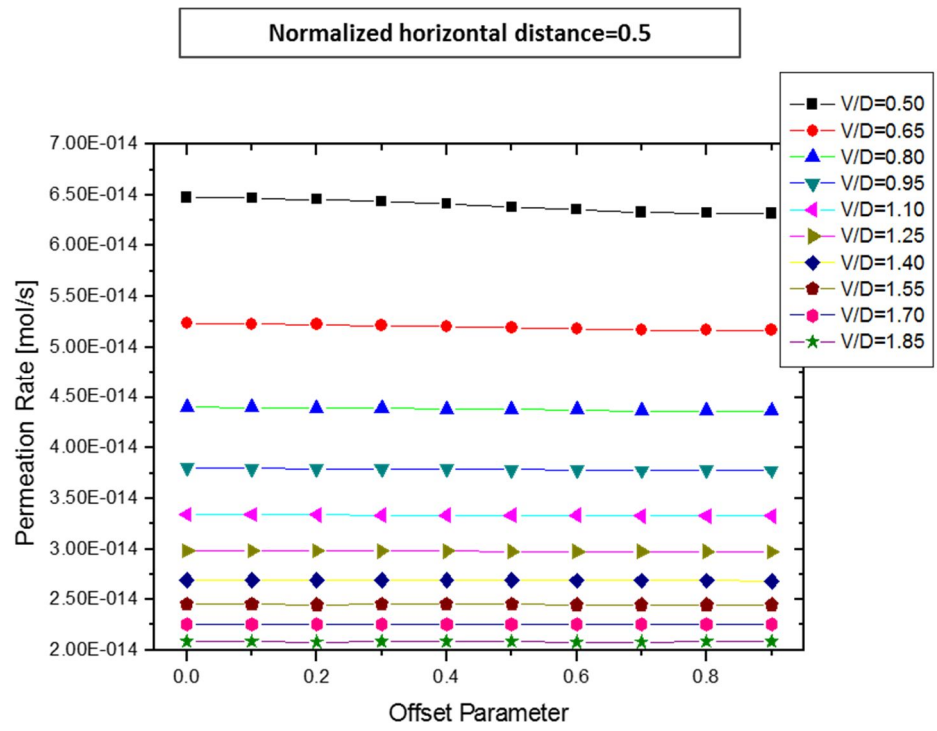


Figure 4. 19 Effect of offset ( $h=0.5$ )

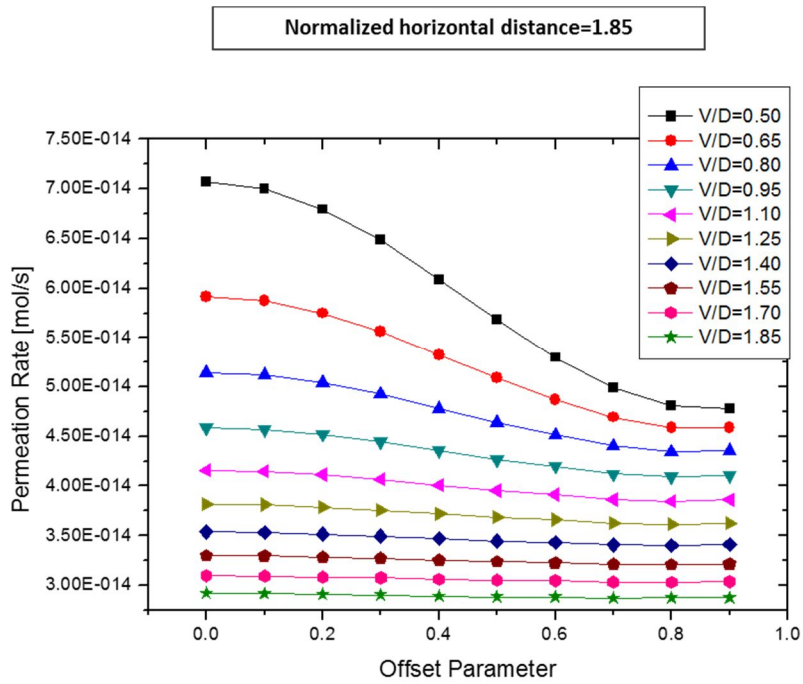


Figure 4. 20 Effect of offset (h=1.85)

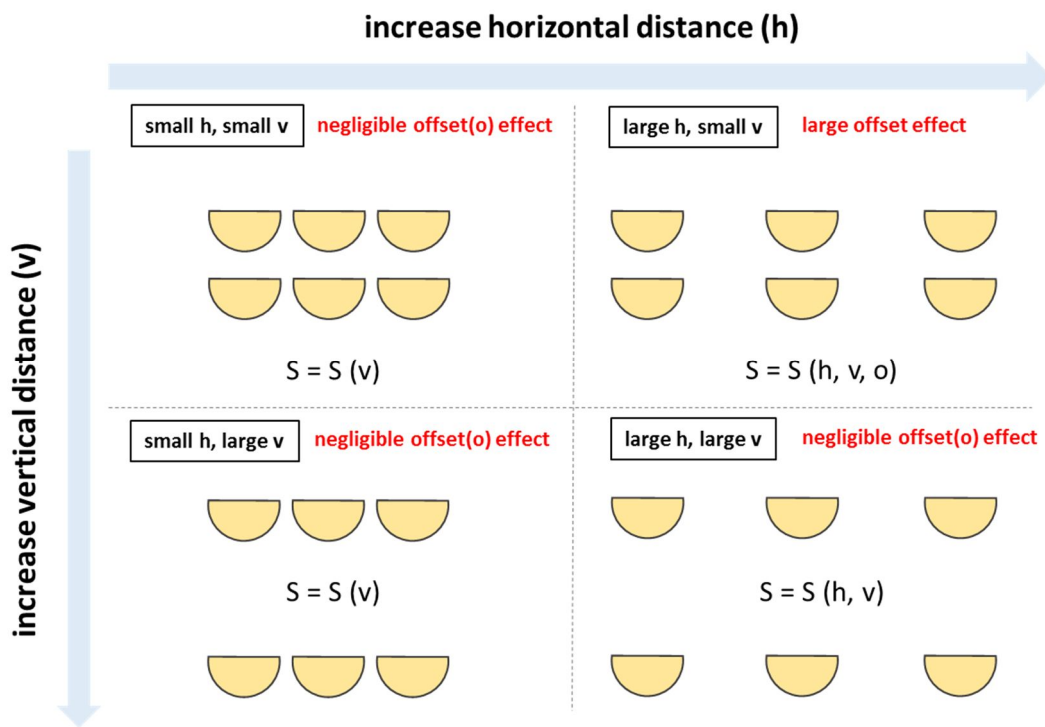
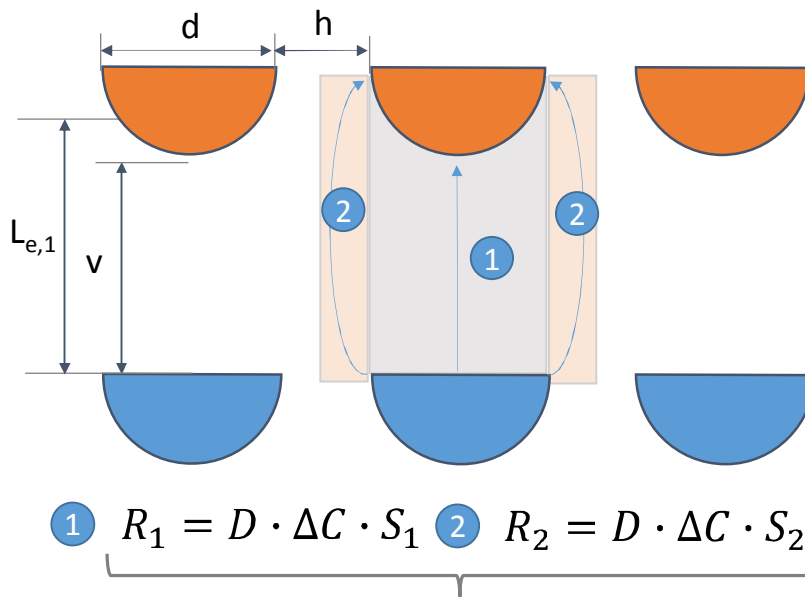


Figure 4. 21 Result summary of 2-D tritium analysis



$$R = R_1 + R_2$$

Figure 4. 22 Tritium permeation path

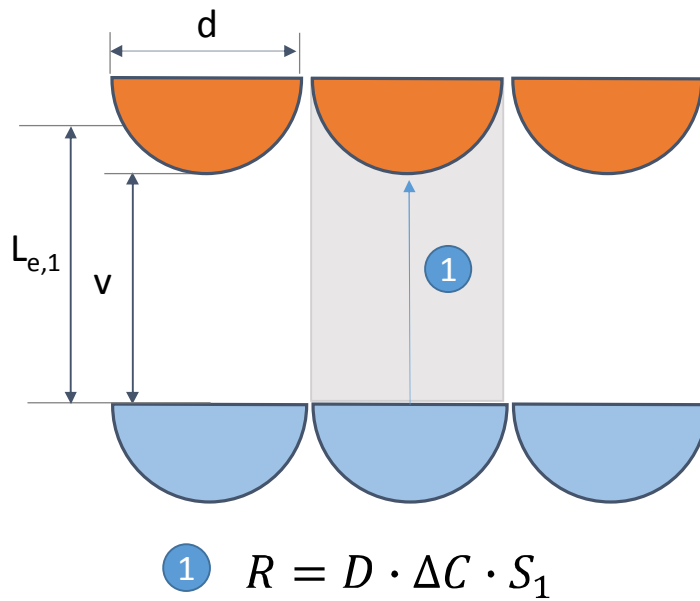


Figure 4. 23 Elimination of tritium path-2

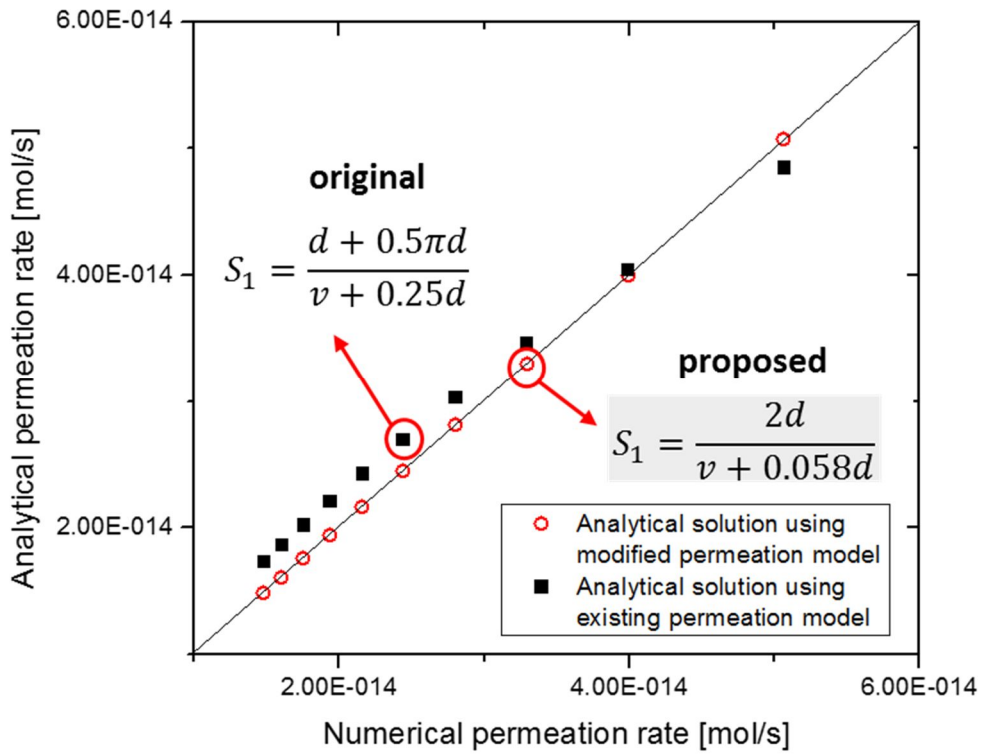


Figure 4. 24 Comparison of analytical and numerical solutions ( $S_1$ )

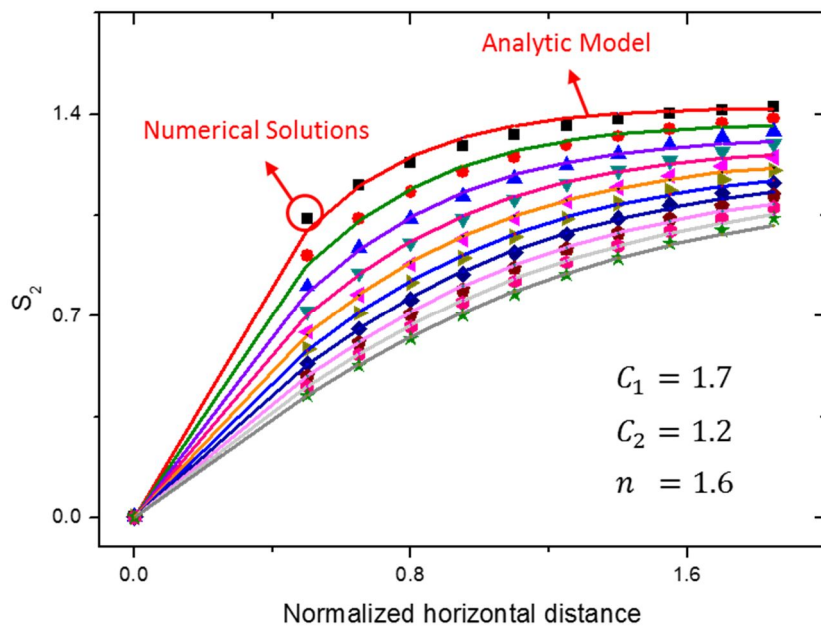


Figure 4. 25 Fitting of shape factor 2

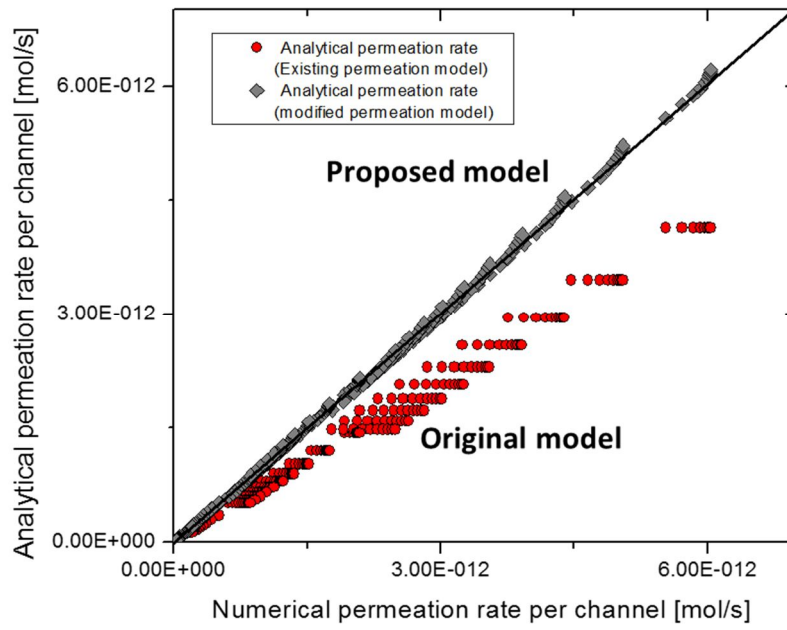


Figure 4. 26 Comparison of analytical and numerical solutions ( $S_1$  and  $S_2$ )

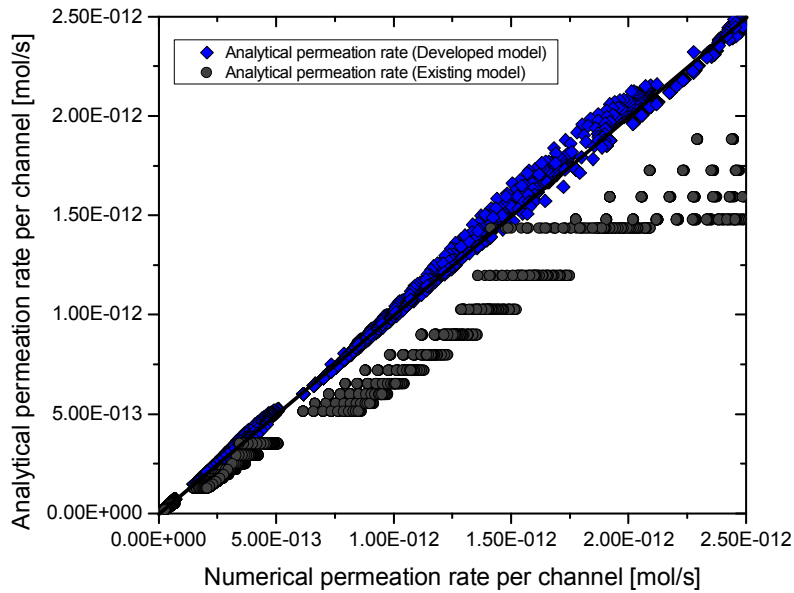


Figure 4. 27 Comparison of analytical and numerical solutions (including effective vertical distance)

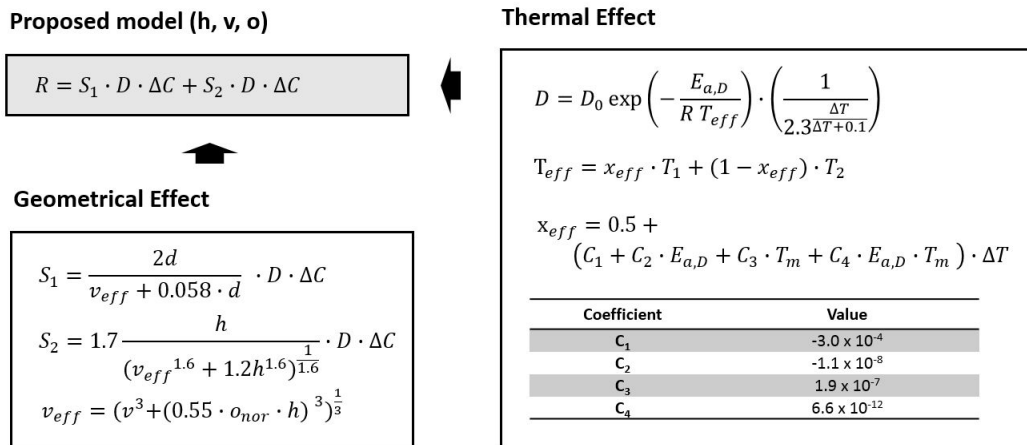


Figure 4. 28 Final form of the developed PCHE tritium permeation model

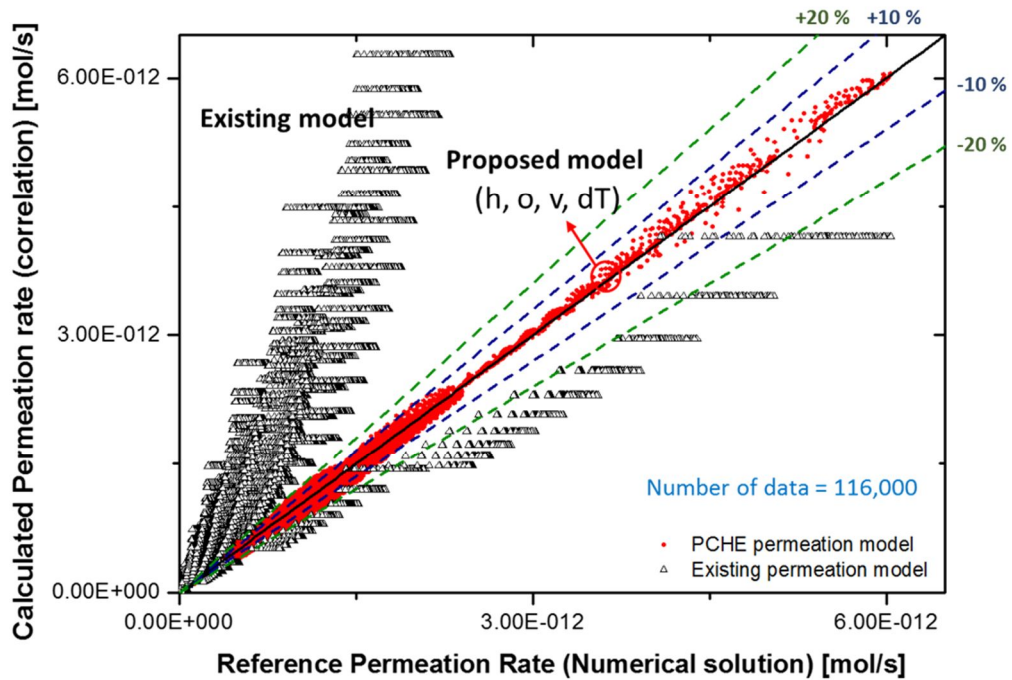


Figure 4. 29 Comparison between the reference solution and the analytical solutions of the existing model and the developed model

## Chapter 5

### Permeability Experiment at Low Temperature

In the case of polycrystalline, basically all the industrial metals, the diffusion mechanism changes over temperature as seen in the figure 5.1. At low temperature, grain boundary diffusion, a diffusion mechanism where diffusion along the grain boundaries of the grains, is dominant. At high temperature, the lattice diffusion, diffusion across the grains, is dominant. As the diffusion mechanism changes over temperature, naturally the slope of the diffusivity changes. Previous hydrogen permeation studies have been focused on high temperature region where the lattice diffusion is dominant as seen in Table 5.1. In other words, there is a lack of permeation data at low temperature region. In this study, lack of grain boundary diffusion data can cause significant under prediction in predicting tritium permeation. Therefore, the hydrogen permeation data at low temperature region is obtained experimentally in this study.

Furthermore, in previous hydrogen permeation studies, out-gassing has been conducted at very high temperatures, around 1000 °C, which can cause changes in the material micro-structure and eventually cause errors. Thus, in this study, the effect of out-gassing is investigated and appropriate out-gassing condition has been established.

## **5.1 Hydrogen Permeation Experiment**

### **5.1.1 Description of the Hydrogen Permeation Facility (HYPER)**

Hydrogen Permeation Facility, HYPER is a hydrogen permeation experiment facility at NFRI (Park, 2013). The facility is constructed in order to investigate hydrogen permeability, diffusivity and solubility for various materials. The overview of HYPER facility and the P&ID of HYPER facility are depicted in Figure 5.2 and 5.3. In the figure, the HYPER facility structure can be observed. The test section module is placed between the two process volumes. And on the right hand side of the process volume 2, the control modules is placed. Below the test section, the QMS, pressure control module and the vacuum pumping module are present. The test section is surrounded by the infra-red heater and inside the test section the test tube can be found as illustrated in Figure 5.4. And the disk type specimen is designed to be inserted inside the test tube as seen in the figure. As described in the P&ID schematic, pressures of the process volumes are measured using 3 CDG sensors. 3 CDG sensors are installed for reliability.

### **5.1.2 Experimental Procedure**

Prior to the permeation measurement, disk type specimen is to be prepared. In this study, S316 disk is prepared for the permeation experiment as it is the material of heat exchanger in the VHTR. The diameter of the specimen is 2 mm and the thickness is decided as 0.7 mm. In order to minimize error due to the

roughness of the specimen, the surface of the specimen is mechanically polished and chemically cleaned using ethanol and acetone.

Hydrogen permeation is measured using the pressure rise method. In other words the permeation rate is measured by recording the rate of pressure rise in the process volume 2. The experimental procedure is as follows. Initially after inserting the test specimen, gases in process volume 1 and 2 and other volumes are purged using the pump until vacuum conditions are established in both process volumes. When the pressures in the process volumes are around  $1\text{E-}7$  Pa, leakage test is conducted. Helium gas is sprayed around the test section, flanges and valves in order to ensure that no leakage exists. If defect exists, the helium gas sprayed on the test facility will result in increase of helium concentration inside the test facility. Once it is ensured that no leakage exists, out-gassing is performed. Out-gassing is conducted by raising the temperature up to  $400\text{ }^{\circ}\text{C}$  and maintaining it for 24 hours.

After performing the out-gassing procedure, the temperature is then set to the test temperature and the permeation experiment is conducted. Hydrogen is inserted in the process volume 1 until the pressure reaches 101 kPa. Once the target pressure is achieved, the valves, PV22 and PV23, are opened and the pressure rise in process volume 2 is measured using the CDG sensors.

The pressure rise rate obtained in the experiment is then converted into permeability. The rate at the start of steady state, where the rate limiting process is diffusion through material rather than the surface reactions, is taken as shown in Figure 5.5. Using the rate obtained in the graph and the parameters obtained in the experiment, the permeability is calculated using the below equation.

$$J = \frac{D \cdot P_h^{1/2}}{l} \quad (5.1)$$

### 5.1.3 Uncertainty Analysis

For the reliability of the permeability data obtained in the HYPER experiment, uncertainty analysis is conducted on the permeability data based on AMSE PTC 19.1 (ASME, 2013). The permeability of hydrogen is calculated using the following equation.

$$D = \left( \frac{V \cdot L}{R \cdot T \cdot P_1^{0.5} \cdot A} \right) \cdot \left( \frac{dP_2}{dt} \right) = \left( \frac{V \cdot L}{R \cdot T \cdot P_1^{0.5} \cdot A} \right) \cdot \dot{P} \quad (5.2)$$

Thus, the systematic uncertainty can be calculated using the below equation.

$$u_s = \frac{dD}{D} = \left[ \left( \frac{\delta V}{V} \right)^2 + \left( \frac{\delta T}{T} \right)^2 + \left( \frac{\delta A}{A} \right)^2 + \left( \frac{\delta L}{L} \right)^2 + \left( \frac{\delta P_1}{2P_1} \right)^2 + \left( \frac{\delta \dot{P}}{\dot{P}} \right)^2 \right]^{1/2} \quad (5.3)$$

The systematic uncertainty is basically root sum square of the uncertainties of each parameter. The uncertainties of each parameter for 150 °C permeability case is obtained as listed in Table 5.2. The uncertainty of the pressure slope is calculated by obtaining the maximum and minimum slopes using the error bound of the pressure data and averaging the two slopes and dividing it by the best fit slope as shown in Figure 5.6. The average of the maximum and minimum slopes is utilized as the error of the pressure slope,  $\dot{P}$ . In the case of permeability at 150 °C the systematic uncertainty is calculated to be 7.8 %. Same procedure is conducted for other temperature cases.

In order to calculate random uncertainty, reasonable number of sample data

are essential. However, permeation experiment duration time is too long for number of repetition. Thus, in this study, a conservative random uncertainty from previous studies (Huang, 2010) is deducted and utilized, 8 %.

Using the calculated and deduced systematic and random uncertainties, the total uncertainty is calculated using the below equation.

$$u_c = \sqrt{(u_s)^2 + (u_r)^2} \quad (5.4)$$

Calculated total uncertainties for permeability for each temperature is listed in Table 5.3. And the permeability data with the error bound is presented in Figure 5.7.

#### 5.1.4 Effective Permeability

The permeability data from HYPER experiment are shown in Figure 5.8 and the permeability data from other studies are plotted as well for comparison. As expected, the permeability slope of hydrogen changes at a certain temperature due to the change in diffusion mechanism. The activation energy and permeability pre-factor are obtained using the slope of the Arrhenius. The obtained parameters are displayed in Table 5.4. Furthermore, the effective permeability is defined and suggested based on the permeability data. It is defined as a sum of lattice diffusion permeability and grain boundary diffusion permeability as shown below.

$$D_{eff} = D_{lattice} + D_{gb} = D_{0,lattice} \cdot \exp\left(\frac{-E_{a,lattice}}{RT}\right) + D_{0,gb} \cdot \exp\left(\frac{-E_{a,gb}}{RT}\right) \quad (5.5)$$

The effective permeability, using the obtained activation energy and permeability pre-factor, is plotted in Figure 5.9. And as seen in the figure, the effective permeability agrees well with the permeability data. Thus, it can be

concluded that an effective permeability is developed for a broad temperature range, even down to low temperature region.

One thing to note is that the permeability from Forcey at 300 °C is much lower than the permeability from HYPER at the same temperature or even at lower temperatures. In order to find out the reason, the experiment procedure and conditions have been revised. As a result, the difference in out-gassing condition is noted.

## 5.2 Grain Size Effect on Hydrogen Permeation

In most of the previous hydrogen permeation studies, out-gassing of the specimen is conducted at very high temperatures, 1000 °C. The change in material due to this high temperature out-gassing procedure is inevitable. The change of S316L properties are shown in Table 5.5. As seen in the table, the change is hardly shown at medium temperatures, however it turns significantly at high temperatures.

### 5.2.1 Effect of Temperature on Grain Size

When assuming normal grain growth, the grain size can be calculated using the below equation (Louat, 1974).

$$d_{grain} = \sqrt{bt + d_0^2} \quad (5.6)$$

$$b = b_0 \exp\left(\frac{-E_{a,grain}}{RT}\right) \quad (5.7)$$

As can be predicted from the equation, the grain growth increases with increasing temperature and time of exposure. In order to investigate the effect of out-gassing temperature, the grain size of S316 is measured. The specimens are prepared by baking at 25 °C, 400 °C and 1000 °C using vacuum oven for 24 hours. After baking the specimens are cooled down to room temperature and then electro polished in order to expose the grain boundaries. Using the SEM images of the etched surface of the specimen in Figure 5.10, the grain sizes are measured using the Average Grain Intercept (AGI) method. As seen in Table 5.6, The grain sizes, after 24 hours of baking at 25 °C and 400 °C, are relatively similar whereas after 1000 °C baking, the grain size increases about 4.5 times the original grain size. Obviously the grain size increase would have affected the physical properties of the material, which could have eventually influenced tritium permeation.

### **5.2.2 Effect of Grain Size on Permeation**

The change in grain size would have definitely affected the permeation rate especially in grain boundary diffusion dominant region. The grain growth would have affected the surface area to volume ratio of the grains meaning that the path of permeation would have significantly decreased which would eventually result in decrease in permeation rate due to decrease in permeation path. This can also be predicted from Hart's equation, the effective diffusion coefficient equation for polycrystalline material is as shown. From the hart's equation (Hart, 1957) and the equation 5.10, the effective permeability for polycrystalline can be deduced as seen in equation 5.11.

*Effective diffusion coefficient for polycrystalline*

$$\phi_{eff} = f \cdot \phi_{gb} + (1-f) \cdot \phi_{lattice} \quad (5.8)$$

$$f = \frac{q_h}{d} \cdot \delta_h \quad (5.9)$$

*Correlation of diffusion coefficient and permeability*

$$D = \phi \cdot K \quad (5.10)$$

*Effective permeability for grain size*

$$D_{eff,g} = f \cdot D_{gb} + (1-f) \cdot D_{lattice} \quad (5.11)$$

Thus, the possibility of the out-gassing temperature, 1000 °C, in previous studies affecting the permeability is very high. In previous studies, the out-gassing procedure would have resulted in grain growth which would have eventually resulted in lower permeability. The difference between permeability of HYPER and the other groups can be explained by this out-gassing condition difference.

Table 5. 1 Previous hydrogen permeation studies

References	Temperature range [°C]
Kishimoto, 1884	600-900
Forcey, 1988	250-600
Changqi, 1991	230-600
Shiraishi, 1999	400-700
Lee & Noh, 2011	400-800
Tamura, 2014	300-500

Table 5. 2 Uncertainties of each parameters

Parameter	Uncertainty	
Volume	0.49 %	Standard volume measurement uncertainty
Temperature	2.2 °C or 0.75 %, whichever larger	K type thermocouple uncertainty
Diameter	5E-6 m	Microscope uncertainty
Area	0.000486	$u_A = \sqrt{2u_D^2}$
Thickness	2.00 %	Sampling error
Pressure	0.15 %	Pressure gauge uncertainty
Pressure slope	0.074	Slope uncertainty measurement

Table 5. 3 Total uncertainties of permeability data at each temperature

Temperature [°C]	Permeability [ $\text{mol m}^{-1} \text{s}^{-1} \text{Pa}^{-0.5}$ ]	Total uncertainty [%]
150	3.37336E-13	11.2
175	3.42711E-13	11.0
200	3.43384E-13	9.5
300	3.79327E-13	10.1
400	1.23170E-12	9.0
500	5.13063E-12	8.6
600	1.26281E-11	8.5

Table 5. 4 Obtained activation energy and permeability pre-factor

Temperature range [°C]	T>350	350>T
Diffusion mechanism	Lattice diffusion	Grain boundary diffusion
Activation energy [ $\text{J mol}^{-1}$ ]	57108	1620
Permeability pre-factor [ $\text{mol m}^{-1} \text{s}^{-1} \text{Pa}^{-0.5}$ ]	3.435E-8	5.288E-13

Table 5. 5 Change in S316L property (Shanghai Stal Precision Stainless Steel Co. LTD, 2013)

<b>Temperature [°C]</b>	<b>Yield strength [MPa]</b>	<b>Ultimate tensile strength [MPa]</b>
20	292	568
93	-	521
204	-	492
316	-	491
427	183	493
538	161	472
649	156	349
760	-	212
871	-	124

Table 5. 6 Measured grain size after 24 hours of baking at different temperatures

<b>Baking temperature [°C]</b>	<b>Grain size [<math>\mu\text{m}</math>]</b>
25	12.3
400	11.0
1000	48.9

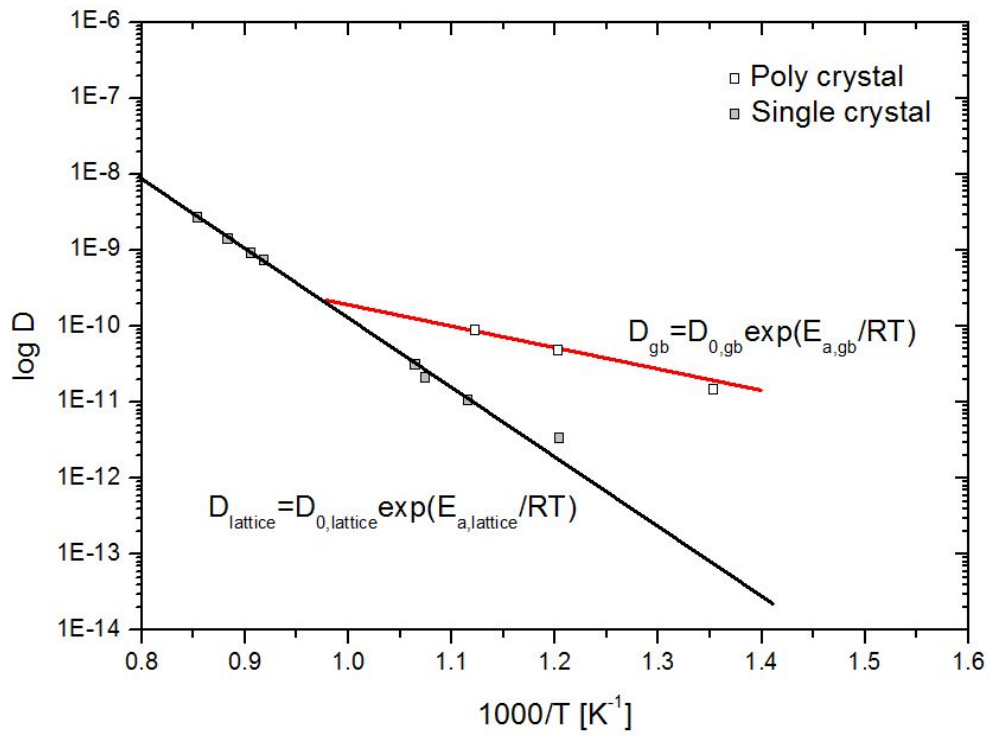


Figure 5. 1 Example of a diffusivity graph

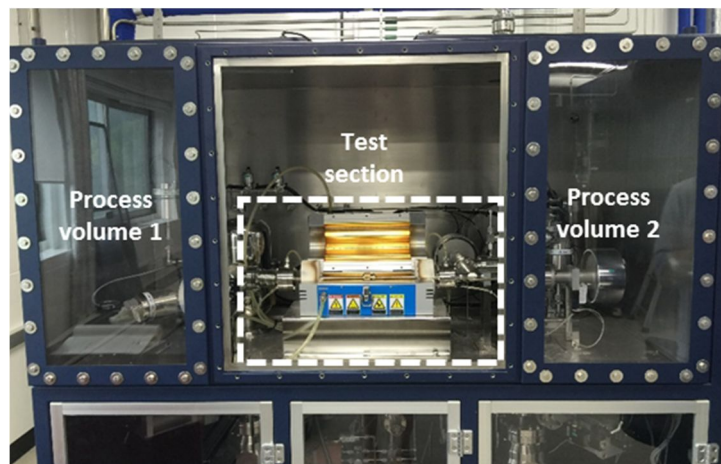


Figure 5. 2 Overview of HYPER facility (Park, 2013)

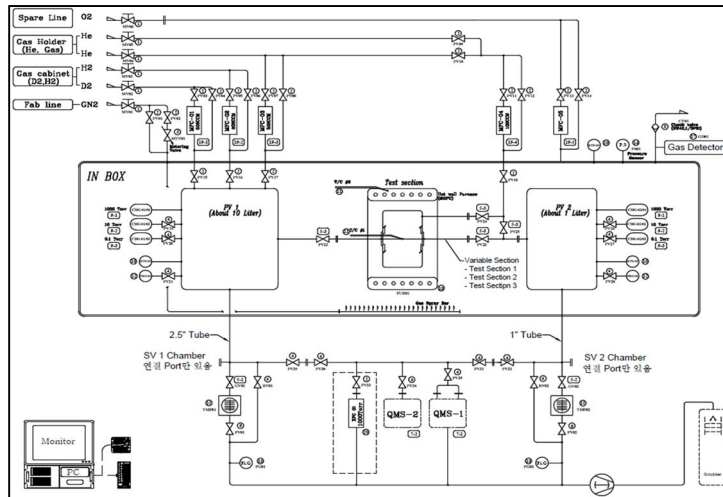


Figure 5. 3 P&ID of HYPER (Park, 2013)

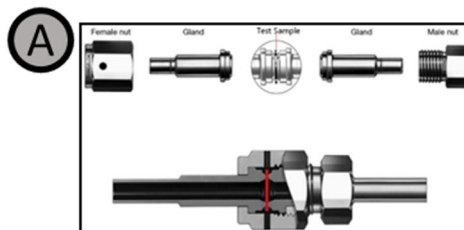
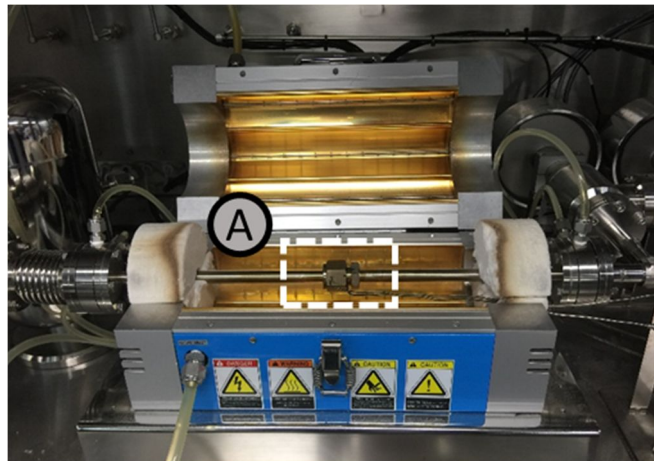


Figure 5. 4 HYPER test section (Lee & Noh, 2011)

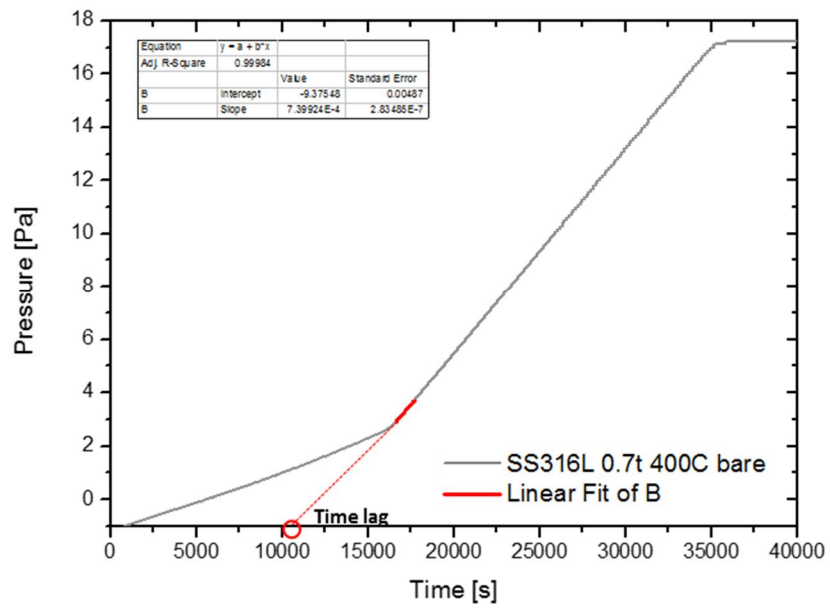


Figure 5. 5 Pressure rise rate in the 2<sup>nd</sup> process volume (0.7t, S316L, 400°C)

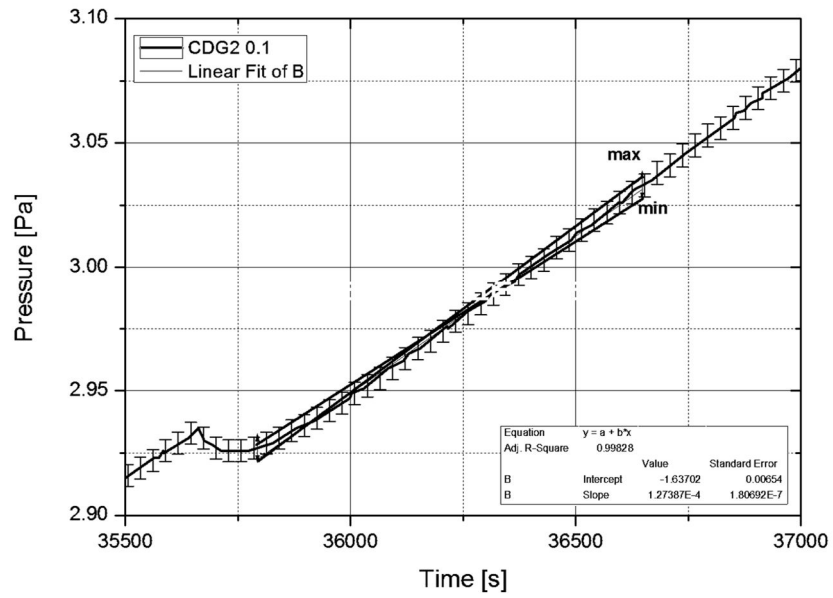


Figure 5. 6 Minimum and maximum pressure slopes (0.7t, S316, 200°C )

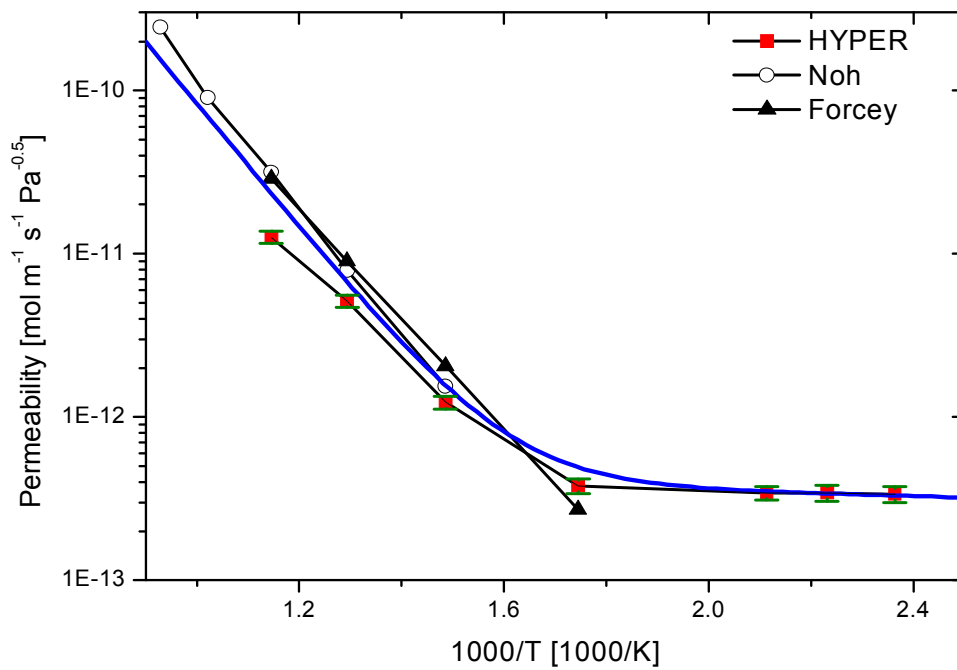


Figure 5. 7 Permeability data with error bars

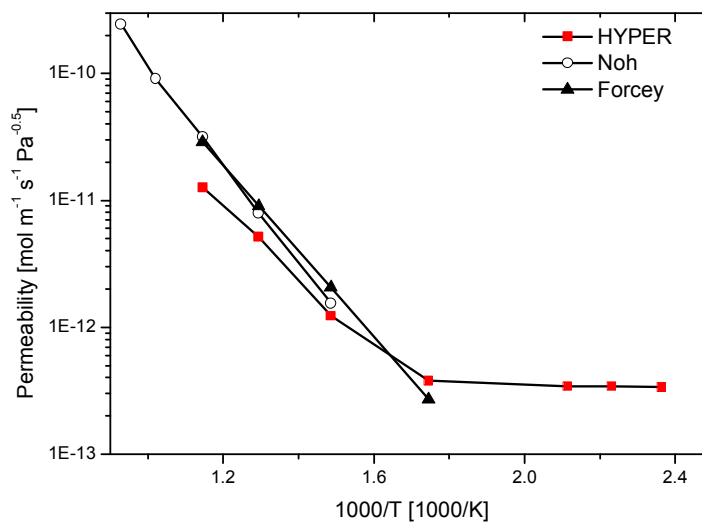


Figure 5. 8 HYPER permeability data with other permeability data

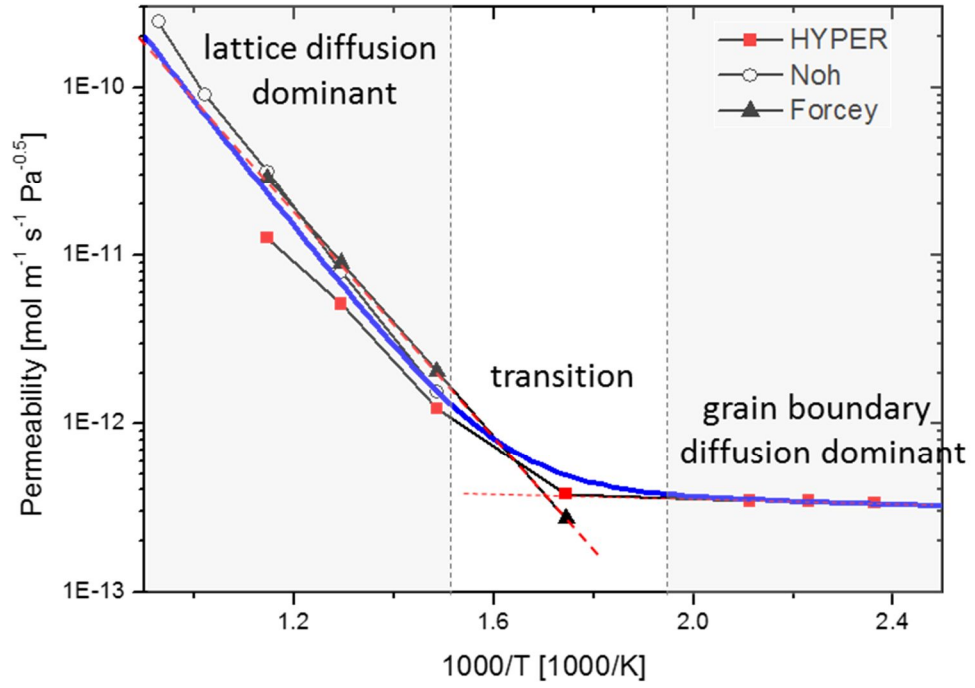


Figure 5. 9 Permeability slope transition and effective permeability

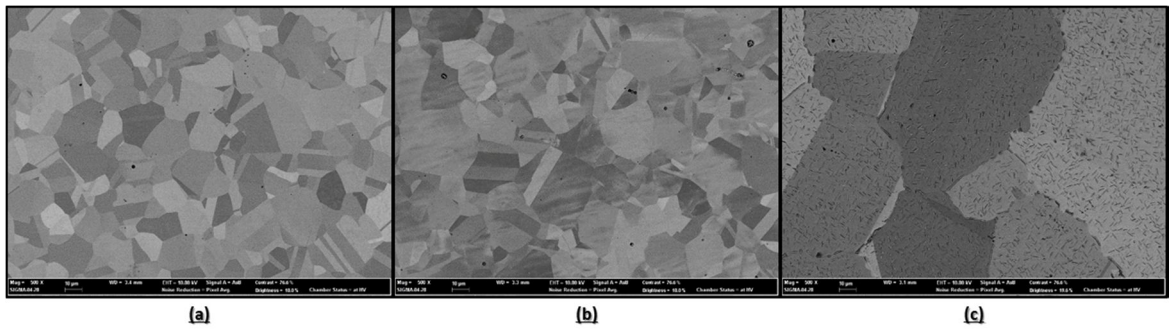


Figure 5. 10 SEM image of electro polished surface of S316L baked at (a) 25 °C (b) 400 °C (c) 1000 °C

## **Chapter 6**

# **Tritium Analysis of VHTR-FO integrated system**

### **6.1 Tritium analysis on the proposed VHTR-FO system**

In the previous section, an effective VHTR-FO integration system has been suggested and the tritium issue associated with the system has been noted. In order to analyze the tritium behavior in the VHTR-FO system following have been developed; (1) BOTANIC tritium code, (2) PCHE tritium permeation model and (3) modified effective permeability. Using the developed tritium tools, the tritium behavior in the VHTR-FO system is analyzed.

The simulated VHTR-FO system using BOTANIC is shown in Figure 6.1. The system consists of primary loop, secondary loop and two process heat loops. PMR 200 reference core design was used for reactor input calculation. The calculated inputs are listed in Table 6.1. The thermal power of the reactor was assumed as 200 MWt and the tritium release rate in the reactor core was assumed as 7.5 % based on the tritium diffusion analysis in TRISO (General Atomics, 2006). The intermediate heat exchanger and the recuperator were assumed to be printed circuit heat exchangers and the other heat exchangers are assumed as shell and

tube heat exchanger. The design parameters of the heat exchangers such as surface area, channel diameter, pipe length, etc., are listed in Table 6.2. The purification efficiency of tritium is assumed to be 100 % and the flow rates to the purification systems 1 and 2 are given as 0.05 %. The FO system is simplified as shown in the figure. The overall efficiency is calculated as 42.2 % which is slightly lower than the VHTR system simulated in chapter 2 due to the presence of the purification system. And in the case of base scenario, the effect of sorption is neglected.

The result of the analysis is depicted in Figure 6.2. The tritium concentration in the final water product of the VHTR-FO system exceeds the regulatory limit as shown in the figure. For the base scenario where one assumes 7.5 % of tritium release fraction, tritium level in the water product is calculated to be  $1.6 \text{ E-4 } \mu\text{Ci/mL}$ , which exceeds the regulatory limit by an order which stresses the necessity of tritium reduction. Not to mention the tritium level when assuming maximum release. Furthermore, when using the original permeability where one neglects the grain boundary diffusion, it significantly under predicts the tritium concentration in product water by about 3 orders.

The tritium distribution in the base scenario is shown in Figure 6.3. As seen in the figure, most of the tritium released into the system migrates down to the secondary and to the FO system. Only about 1.25 % of tritium is removed from the system through purification. This ratio is very different from that obtained in previous studies (Kim, 2010). This is due to the modified effective permeability. When original permeability is applied, similar tritium distribution ratio can be observed as in the previous studies shown in Figure 6.4. In this case, most of the tritium is removed from the system and only 0.2 % of tritium migrates down to the FO system. This is due to the permeability under-estimate in the process heat

exchangers as the original permeability ignores the grain boundary diffusion. This under-predicted permeability result is much slower permeation in the PHX which allows more coolant inventory to enter the purification system due to longer duration time of tritium in the primary and secondary loops. Consequently the tritium level in final water product in FO system satisfies the regulatory limit. This emphasizes the importance of the developed effective permeability and the misguide of the original permeability.

On the other hand, the effect of sorption mechanism has been studied by inserting different sorption area inputs. Figure 6.5 depicts tritium release rate from the reactor into the system. As seen in the figure, the tritium sorption capacity increases with increasing sorption surface area. And once the sorption capacity is saturated, the sorption rate decreases and converges to 0. The tritium distribution at  $1E5$  s when sorption area is given as  $500 \text{ m}^2$  is shown in Figure 6.6. As illustrated in the figure, from the tritium released into the system which is 7.5 %, large portion of tritium is sorbed onto graphite, 78.6 %. However, at  $7E6$  s, after sorption capacity is saturated, the tritium distribution is identical to that of the case where tritium sorption is neglected. The sorption mechanism has been neglected in the base scenario as it is difficult to obtain realistic sorption related inputs.

To conclude, the tritium behavior in VHTR-FO system has been analyzed using the developed BOTANIC code, PCHE tritium permeation model and effective permeability. And as a result, the tritium concentration in the final water product is calculated to exceed the regulatory limit by an order in the case of base scenario.

## **6.2 Sensitivity Study on the VHTR-FO system**

### **6.2.1 Key parameters**

In order to identify the key parameters that affect the tritium migration, and to understand the behavior in the system, sensitivity analysis is conducted. From the number of inputs associated in the VHTR-FO system, 20 parameters have been selected for sensitivity analysis. Those which are considered to be effective in terms of tritium permeation and the level of tritium in the system are selected. Table 6.3 summarizes the list of input parameters and their physical meanings. One factor at a time (OFAT) method is used in this study. The input values of the key parameters are altered  $\pm 20\%$  or  $\pm 25\%$  from the baseline scenario and the according changes in the key output values were observed. The key output parameters are overall efficiency of the VHTR PCS and tritium concentration in the FO system.

### **6.2.2 Results and Discussion**

The results of the sensitivity analysis are summarized in Table 6.4 and 6.5. The cases are summarized based on the associated component models. Tritium release rate from the reactor core is found to be the most influential parameter on tritium concentration in final water product.  $\pm 20\%$  change in the tritium release rate results in  $\pm 19.8\%$  change in tritium concentration in final water product. Purification flow fraction in primary and secondary loops are also effective

parameters in terms reducing tritium concentration in final water product, however there is a tradeoff between tritium concentration and plant overall efficiency. Increase in flowrate to purification system tends to reduce tritium concentration in final water product however also results in the reduction of overall efficiency of VHTR PCS.

Other than the uncontrollable tritium release rate and the parameter with trade off, the parameters associated with process heat exchangers are found to be the most influential parameter in tritium concentration in final product water. The parameters of intermediate heat exchanger and recuperator are found to be less influential than the PHX parameters. This is because permeation in the PHX is the rate limiting process among the permeation processes in the overall system. Furthermore the heat exchanger type of the IHX and recuperator are found to have less influence on the tritium level in the final product. This can be explained using the same logic. The permeation in the IHX and recuperator have relatively small effect on tritium level in final product. Thus, whether shell-and-tube heat exchanger is used or printed circuit heat exchanger in IHX does not govern the tritium behavior in the system.

## **6.3 Tritium Mitigation Approaches**

### **6.3.1 Overview**

Based on the results of the sensitivity analysis, number of mitigation approaches have been suggested. In Figure 6.7, the mitigation concepts associated

with the controllable parameters which have been found effective in reducing tritium concentration in the final water product are summarized. The concepts are mostly associated with the heat exchangers. The concepts include the change in heat exchanger design, tritium barrier, heat exchanger material substitution and pre-heat treatment.

### **6.3.2 Evaluation on the suggested mitigation approaches**

Further evaluation is made on the suggested mitigation concepts. Since the PHX parameters are proven to be the more effective parameters in reducing tritium, evaluation is conducted on the concepts involved in PHX; tritium barrier, Heat exchanger material, and PHX pre-heat-treatment.

#### **A. Tritium Barrier**

Capturing tritium inside the intended volume is one of the most important issues in fusion field. Naturally, tritium barriers have been studied intensively. Various materials have been tested including alumina (Forcey, 1991), chromium oxide (Nakamichi, 2001), silicon oxide (Nakamichi, 2001), titanium oxide (Yao, 2000), etc. The suggested tritium barriers and the tritium reduction factors (TRFs), are listed in Table 6.6. And the change in tritium concentration in product water due to the TRF applied on the PHX have been investigated through parametric study. The result is depicted in Figure 6.8. As expected, the tritium concentration in product water decreases linearly as the TRF increases. The tritium concentration in the final product water meets the regulatory limit when TRF of 500 and above is applied to PHX. TRF of natural oxide of S316L is known to be

around 100 to 1000 meaning that the TRF caused by natural oxide of S316L will be sufficient enough to satisfy the regulatory limit in VHTR-FO final water product.

### **B. Effect of heat exchanger material**

This concept has been evaluated by changing the material of the PHX, the permeability applied in PHX. In total 10 different metals have been evaluated, however, were soon found meaningless due to the lack of grain boundary permeability data for the evaluated metals. Thus, the calculation results are discarded. The ceramic materials such as aluminum oxide and silicon carbide are evaluated as the heat exchanger material. The results are displayed in Table 6.7. As seen in the table, when using ceramic heat exchanger as the PHX, the tritium concentration in the product water is reduced to near  $0 \mu\text{Ci}/\text{mL}$ .

In order to find out the feasibility of the ceramic heat exchanger the thermal properties and physical properties of the suggested materials are compared with the original material, S316L. As seen in Table 6.8, the higher thermal properties such as conductivity and specific heat can be observed for ceramic materials. And the physical properties seem comparable. Furthermore, the operation conditions of the commercial silicon carbide heat exchanger are identified to be  $-40$  to  $240$  °C and  $0$  to  $16$  bar, which is sufficient for PHX operation range; below  $144$  °C and below  $5$  bar. Therefore, it can be said that using ceramic heat exchanger in the process heat exchange loop is a feasible tritium mitigation method.

### **C. PHX pre-heat-treatment**

In Chapter 5, it was found that the heat treatment on metal causes the grain

size growth and the grain size growth decreases the grain boundaries and thus, decreases permeation rate in the grain boundary diffusion dominant region. Thus, the main idea is to utilize this phenomenon to reduce tritium permeation. In order to verify the effect of metal pre-heat-treatment on permeation, additional verification experiment is conducted.

Due to the leakage problem associated with HYPER facility, the hydrogen permeation experiment is conducted in following procedure. The preheat treatment temperature, 871 °C is the maximum operation temperature of S316L.

1. The specimen is preheat treated at 871 °C for 24 hours
2. Before inserting hydrogen in process volume 1, the leakage rate in the process volume 2 is measured.
3. After inserting hydrogen in process volume 1 the leakage rate together with the permeation rate are measured.
4. The permeation rate is obtained by subtracting the leakage rate from the data obtained in step 3.
5. The permeability is calculated using the permeation rate.

As a result, the permeability at 150 °C after pre-heat treatment, is calculated to be  $3.297 \cdot 10^{-14} \text{ mol m}^{-1} \text{ s}^{-1} \text{ Pa}^{-0.5}$  which is about 1 order smaller than the non-heat treated permeability. For comparison the obtained permeability is plotted with the original permeability in Figure 6.9. Thus, it can be said that the heat-treatment on PHX is an effective mitigation concept which is verified.

Table 6. 1 VHTR-FO system base scenario inputs

Parameter	Value	unit
Tritium release rate	7.5	%
Purification efficiency of tritium	100	%
Cross section of $\text{Li}^6$ / $\text{Li}^7$ / $\text{B}^{10}$ / $\text{He}^3$	4.08E-22 / 1.53E-25 / 5.00E-26 / 1.60E-7	
Total mass of helium	1512	kg
Mass of helium in active core	47.95	kg
Volume of concentric pipe	5.66	$\text{m}^3$
Volume of reactor	314	$\text{m}^3$
Total volume of coolant channel in active core	10.16	$\text{m}^3$
Reactor power	200	MWt
Fast neutron flux	2.6E13	$\text{n/cm}^{-2} \text{ s}$
Thermal neutron flux	8E13	$\text{n/cm}^{-2} \text{ s}$
IHX/ Recuperator HX type	PCHE	
IHX/ Recuperator diameter/horizontal pitch/vertical pitch / offset	2 / 1.11 / 0.706 / 0	mm
IHX/ Recuperator number of channels	1607806 / 1960122	
IHX permeation pre-factor / activation energy (Alloy 617)	1.75E-8 / 890180	$\text{kg m}^{-1} \text{ s}^{-1} \text{ Pa}^{-0.5} / \text{J mol}^{-1}$
Recuperator and process HX pre-factor/ activation energy (SS316L)	1.2197E-9 / 1.21E-15 / 68300 / 1620	$\text{kg m}^{-1} \text{ s}^{-1} \text{ Pa}^{-0.5} / \text{kg m}^{-1} \text{ s}^{-1} \text{ Pa}^{-0.5} / \text{J mol}^{-1} / \text{J mol}^{-1}$
Boron atoms	2.09E25	-
Lithium-7 atoms	8.39E23	-

Table 6. 2 Heat exchanger design for base scenario

<b>Parameters</b>	<b>IHX (PCHE)</b>	<b>Recuperator</b>
Surface area	6200 m	7559
Diameter	0.0012 m	0.0012 m
Number of channels	803903	980061
Length	1.5 m	1.5 m
Vertical pitch	0.000706 m	0.000706 m
Horizontal pitch	0.00111 m	0.00111 m
Offset	0 m	0 m
Reynolds, hot side	2177	2795
Reynolds, cold side	2333	2575
Pressure drop hot side	0.6 bar	0.6 bar
Pressure drop cold side	0.5 bar	0.2 bar

Table 6. 3 Sensitivity analysis case summary

	<b>Parameter altered from base scenario</b>
Base scenario	-
Maximum scenario	Tritium release rate 100 %
TR_1/TR_2	Tritium release rate 6 %/Tritium release rate 9 %
SAT1/SAT2	IHX assumed as shell and tube/ Recuperator assumed as shell and tube
PF1_min/PF1_max	Purification system 1 flow fraction 0.04 % / 0.06 %
PF2_min/PF2_max	Purification system 2 flow fraction 0.04 % / 0.06 %
EA_original	SS316L heat exchanger permeation activation energies/pre factors assumed as original (lattice)
IHX_EA1/IHX_EA2	IHX permeation activation energy 71344 J mol <sup>-1</sup> / 107016 J mol <sup>-1</sup>
REC_EA1/REC_EA2	Recuperator permeation activation energy 55120 J mol <sup>-1</sup> / 82680 J mol <sup>-1</sup> (lattice)
PH_EA1/PH_EA2	PHX permeation activation energy 55120 J mol <sup>-1</sup> / 82680 J mol <sup>-1</sup> (lattice)
IHX_V1/IHX_V2	IHX vertical pitch 0.565 mm/ 0.847 mm
IHX_H1/IHX_H2	IHX vertical pitch 0.89 mm/ 1.33 mm
IHX_O/REC_O	IHX offset 0.9 / Recuperator offset 0.9
IHX_D1/IHX_D2	IHX permeation coefficient 9.76E-10 kg m <sup>-1</sup> s <sup>-1</sup> Pa <sup>-0.5</sup> / 1.46 kg m <sup>-1</sup> s <sup>-1</sup> Pa <sup>-0.5</sup>
REC_D1/REC_D2	Recuperator permeation coefficient 1.40E-8 kg m <sup>-1</sup> s <sup>-1</sup> Pa <sup>-0.5</sup> / 2.10E-8 kg m <sup>-1</sup> s <sup>-1</sup> Pa <sup>-0.5</sup>
PH_D1/PH_D2	PHX permeation coefficient 1.40E-8 kg m <sup>-1</sup> s <sup>-1</sup> Pa <sup>-0.5</sup> / 2.10E-8 kg m <sup>-1</sup> s <sup>-1</sup> Pa <sup>-0.5</sup>

Table 6. 4 Results summary of the sensitivity analysis 1

Key parameter	Baseline scenario input value	Change in input parameter	Change in key outputs	
			Tritium concentration change in product water (%)	Plant overall efficiency change (%)
Tritium Source				
Tritium release rate (TR_1/2)	7.5 %	-20 %	-19.8 %	0 %
		+20 %	+19.7 %	0 %
Purification System				
Purification flow fraction in primary (PF1_min/max)	0.05 %	-20 %	+0.11 %	+0.037 %
		+20 %	-0.11 %	-0.037 %
Purification flow fraction in secondary (PF2_min/max)	0.05 %	-20 %	+0.13 %	+0.0057 %
		+20 %	-0.13 %	-0.0057 %
Intermediate Heat Exchanger (IHX)				
IHX Type	PCHE IHX	Shell and Tube IHX	-0.00176 %	0 %
IHX permeability pre-factor (IHX_D1/2)	1.751E-8 [mol m <sup>-1</sup> s <sup>-1</sup> Pa <sup>-0.5</sup> ]	-20 %	-0.003 %	0 %
		+20 %	+0.00024 %	0 %
IHX activation energy (IHX_EA1/2)		-20 %		0 %
		+20 %		0 %
Vertical pitch of IHX (IHX_V1/2)	0.706 [mm]	-20 %	+0.0002 %	0 %
		+20 %	-0.0002 %	0 %
Horizontal pitch of IHX (IHX_H1/2)	1.11 [mm]	-20 %	-0.0002 %	0 %
		+20 %	+0.0002 %	0 %
IHX offset presence (IHX_O)	0	0.9	-0.0002 %	0 %

Table 6. 5 Results summary of the sensitivity analysis 2

Key parameter	Baseline scenario input value	Change in input parameter	Change in key outputs	
			Tritium concentration change in product water (%)	Plant overall efficiency change (%)
Recuperator				
Recuperator permeability pre-factor (REC_D1/2)	LA: 1.22E-09 GB: 1.21E-15 [mol m <sup>-1</sup> s <sup>-1</sup> Pa <sup>-0.5</sup> ]	-20 %	-0.0207 %	0 %
		+20 %	+0.0181 %	0 %
Recuperator permeability activation energy (REC_EA1/2)	LA: 68900 GB: 1620 [J mol <sup>-1</sup> ]	-20 %	0.195527 %	0 %
		+20 %	-0.0629 %	0 %
Vertical pitch of Recuperator (REC_V1/2)	0.706 [mm]	-20 %	+0.0161 %	0 %
		+20 %	-0.0129 %	0 %
Horizontal pitch of Recuperator (REC_H1/2)	1.11 [mm]	-20 %	-0.00133 %	0 %
		+20 %	+0.000922 %	0 %
Offset of Recuperator (REC_O)	0	0.9	-0.00916 %	0 %
PHX (Most effective method for tritium reduction)				
PHX permeability pre-factor (PH_D1/2)	LA: 1.21971E-09 GB: 1.21E-15 [mol m <sup>-1</sup> s <sup>-1</sup> Pa <sup>-0.5</sup> ]	-20 %	-0.627 %	0 %
		+20 %	+0.345 %	0 %
PHX permeability activation energy (PH_EA1/2)	LA: 68900 GB: 1620 [J mol <sup>-1</sup> ]	-20 %	0.250 %	0 %
		+20 %	-0.272 %	0 %
Applying original permeability	-	GB: 0 [mol m <sup>-1</sup> s <sup>-1</sup> Pa <sup>-0.5</sup> ]	-99.842 %	0 %
Inner diameter of PHX (Wall thickness)	0.0206 [m]	-20 %	-3.435 %	0 %
		+20 %	+1.113 %	0 %

Table 6. 6 Tritium reduction factor for S316L coating material  
(Steven & Thad, 2008)

Temperature range [°C]	200-500	500-600
Alumina	$10^2$	$10^3$ - $10^5$
Cr <sub>2</sub> O <sub>3</sub> /SiO <sub>2</sub>	50	
Cr <sub>2</sub> O <sub>3</sub> /SiO <sub>2</sub> with CrPO <sub>4</sub>	$10^3$	
TiN/TiC/TiN	$10^4$ - $10^5$	$10^3$ - $10^4$
TiN/TiC/SiO <sub>2</sub>	$10^4$ - $10^6$	$10^3$ - $10^4$
Natural oxide	$10^2$ - $10^3$	
Pd	10	

Table 6. 7 Effect of ceramic heat exchanger (PHX)

Material (Causey, 2012)		Activation energy [J mol <sup>-1</sup> ]	Permeability pre-factor [mol m <sup>-1</sup> s <sup>-1</sup> Pa <sup>-0.5</sup> ]	Tritium concentration in the product water [ $\mu$ Ci/mL]	Tritium concentration change in product water (%)
S316L	Lattice (Lee & Noh, 2011)	68900	5.25E-7	1.610E-4	0
	Grain boundary	1620	5.288E-13		
Al <sub>2</sub> O <sub>3</sub>		153241	1.308E-13	5.874E-29	-100.0
SiC		122877	4.941E-15	3.573E-27	-100.0

Table 6. 8 Comparison of material properties

	SS316L	Al <sub>2</sub> O <sub>3</sub> (Street, 2016)	SiC (SGL group, 2016)
<b>Thermal conductivity @ 300 K</b> [W m <sup>-1</sup> K <sup>-1</sup> ]	16.2	18	41
<b>Specific Heat</b> [J kg <sup>-1</sup> K]	500	880	750
<b>Coefficient of thermal Expansion</b> [10 <sup>-6</sup> °C <sup>-1</sup> ]	8.9	8.1	4.0
<b>Hardness</b> [HR B]	95	83	158
<b>Tensile strength</b> [MPa]	485	260-300	310
<b>Melting point</b> [°C]	1371-1399	2000	2600
<b>Maximum working temperature</b> [°C]	871	1700	1400
<b>Operating temperature and pressure conditions</b>		N/A	-40 to 230 °C 0 to 16 barg

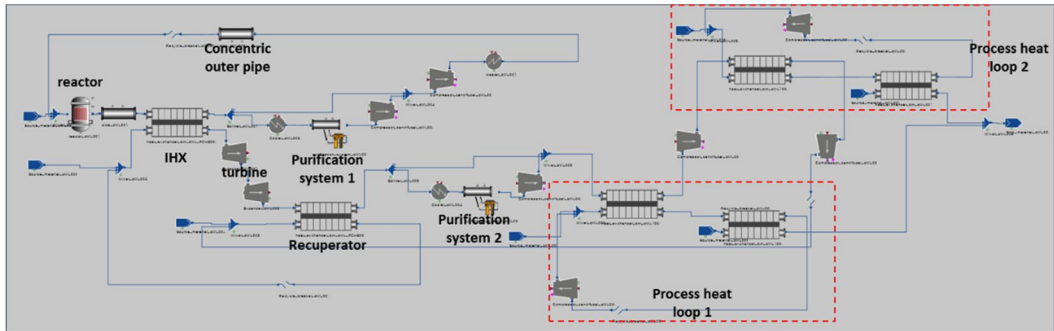


Figure 6. 1 VHTR-FO integration system modelling on BOTANIC

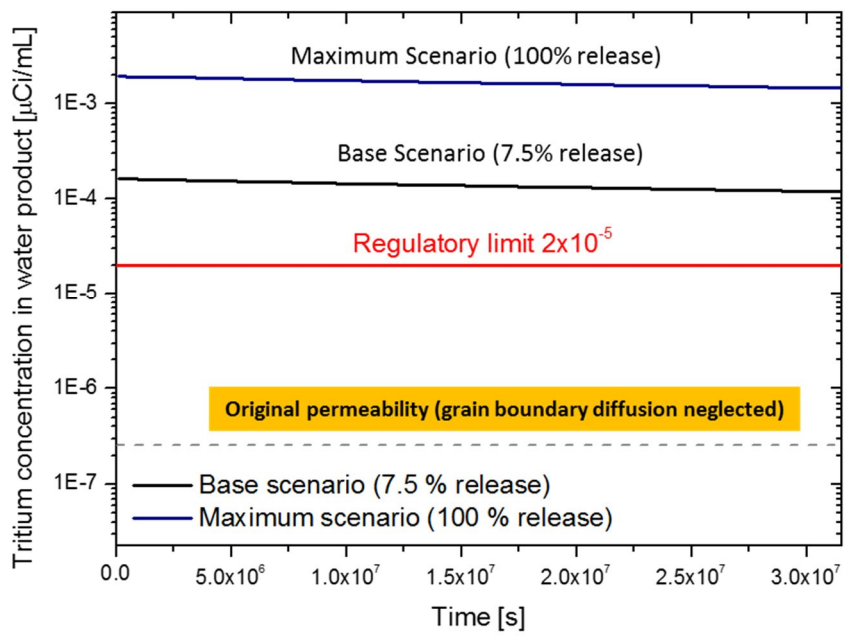


Figure 6. 2 Tritium concentration in the water product of FO-VHTR

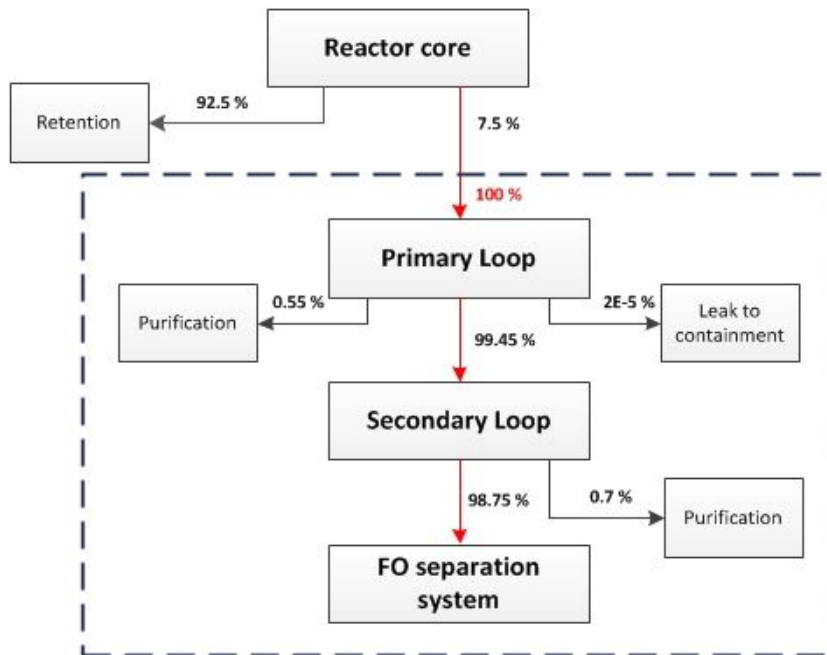


Figure 6. 3 Tritium pathway in VHTR-FO system (base scenario)

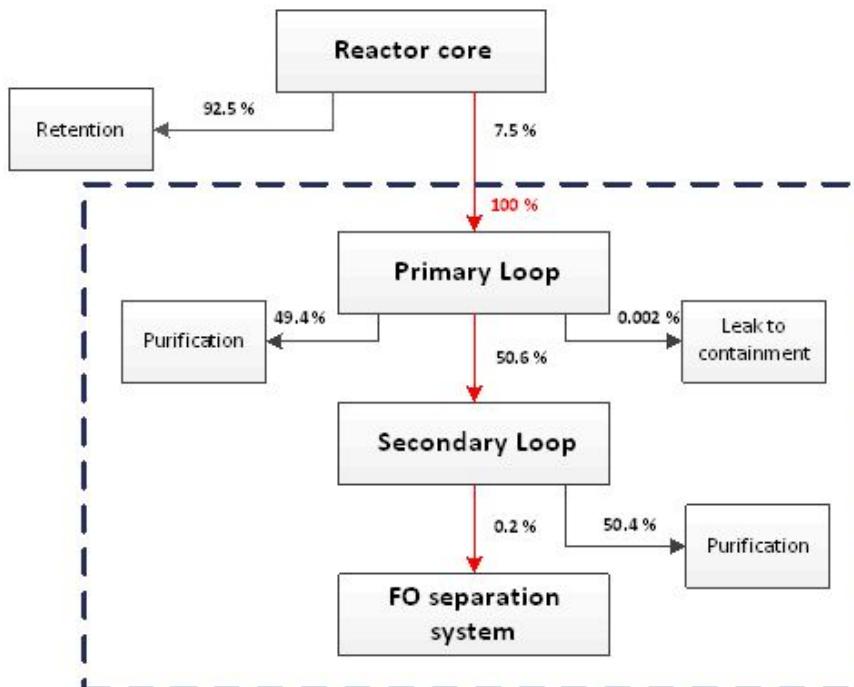


Figure 6. 4 Tritium pathway in VHTR-FO system when using the original permeability (lattice diffusion only)

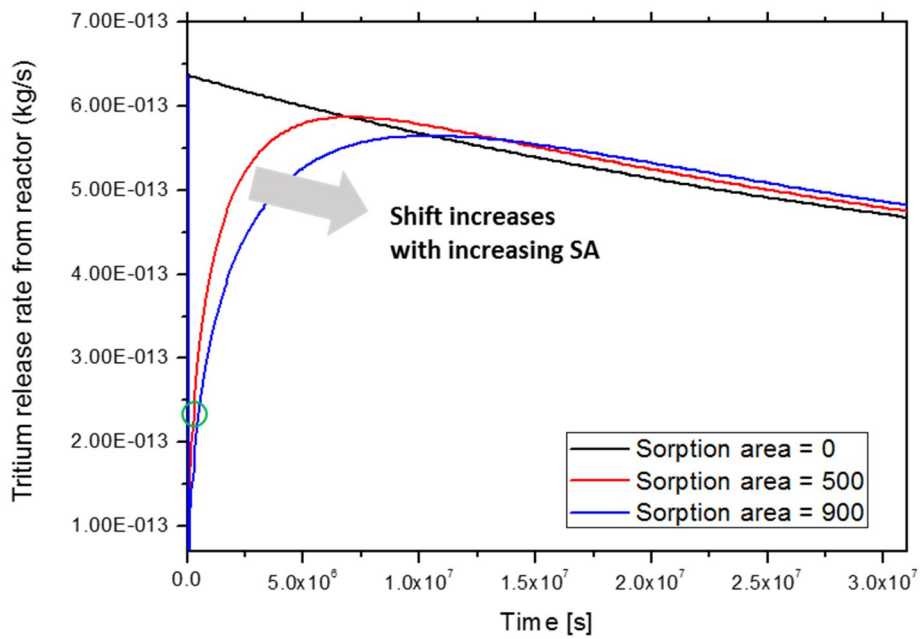


Figure 6. 5 Effect of sorption area on tritium release rate

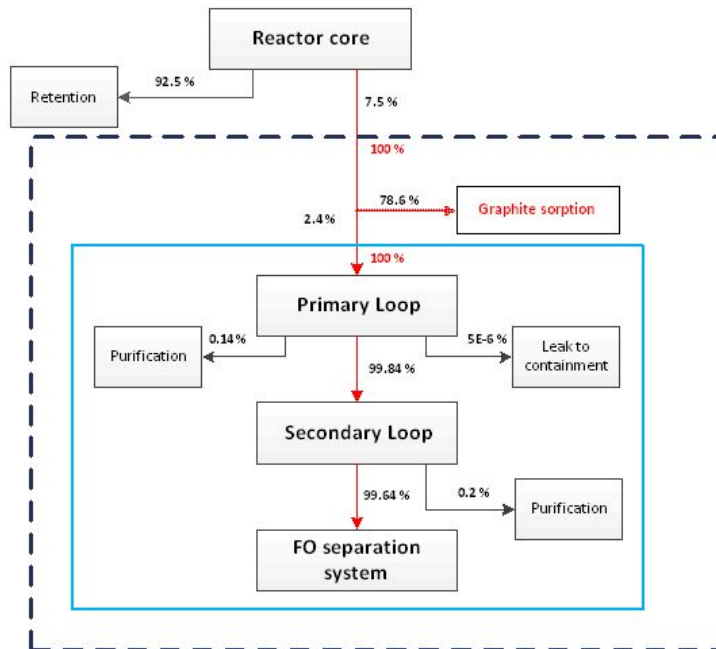


Figure 6. 6 Tritium pathway when sorption area is assumed as 500 m<sup>2</sup>

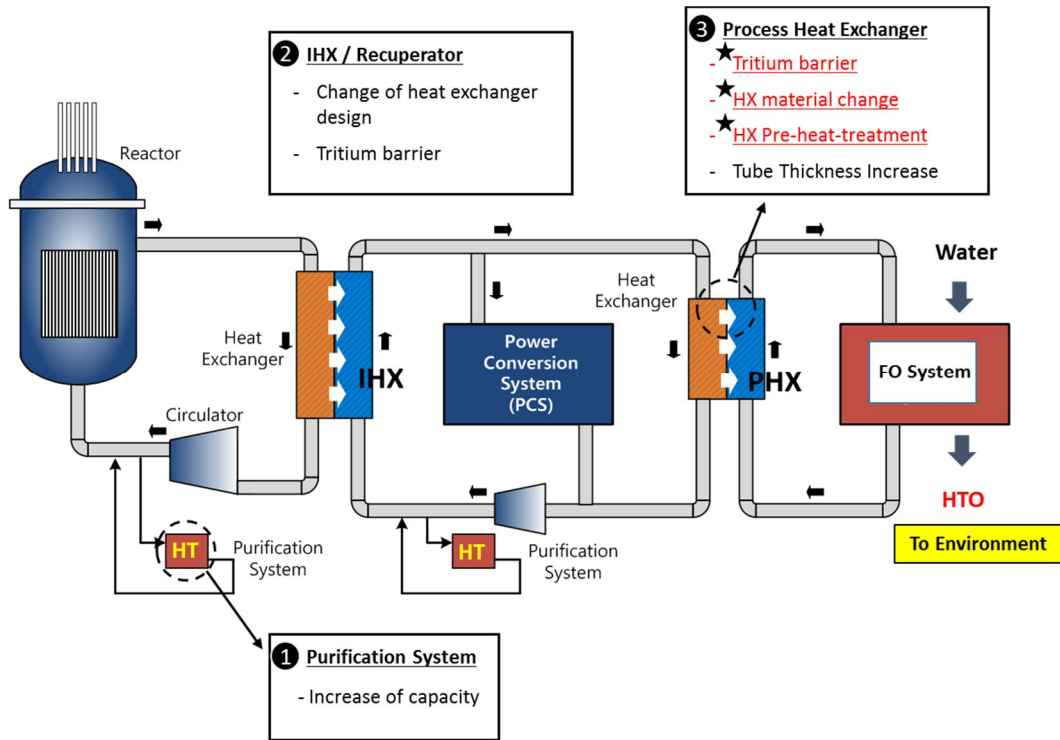


Figure 6. 7 Tritium mitigation concepts

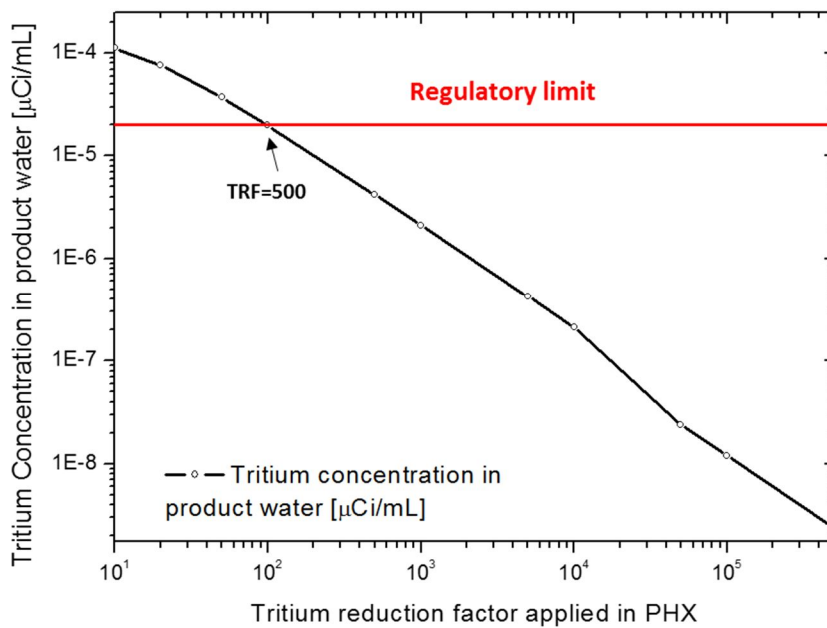


Figure 6. 8 Effect of tritium barrier on tritium concentration in product water

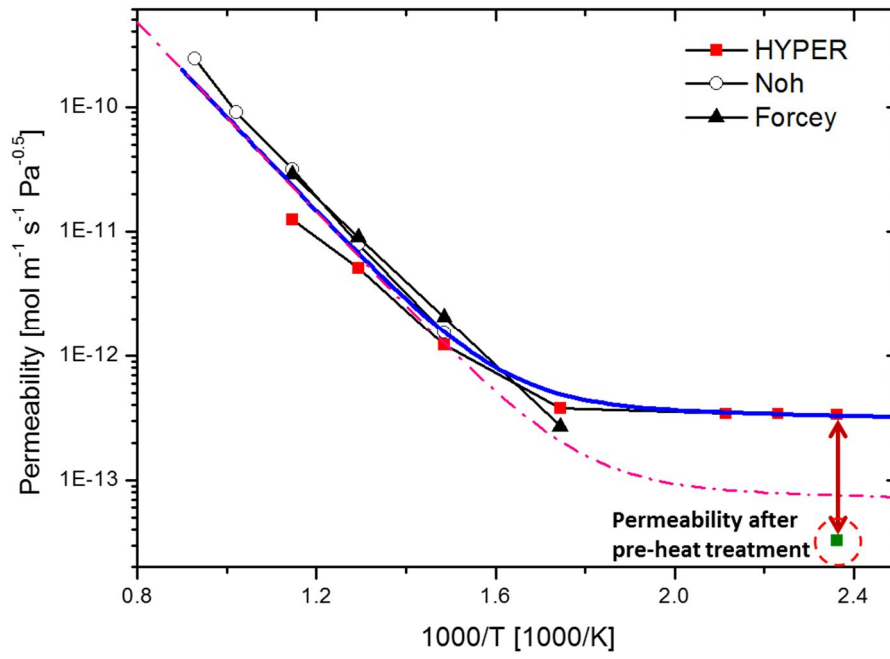


Figure 6. 9 Effect of pre-heat treatment on permeability

## **Chapter 7**

### **Summary and Conclusions**

#### **7.1 Summary**

An effective electricity and water cogeneration system, integration system of VHTR and FO desalination system has been proposed and the feasibility of the concept has been thermodynamically analyzed. As a result, the integrated system of VHTR-FO was found to achieve higher thermal efficiency (GOR) and waste heat utilization rate, 13.8 and 81.9 % than the conventional desalination-VHTR system, 12 and 12.8 %. Accordingly, as the VHTR-FO has an improved thermal efficiency and significantly higher waste heat utilization rate, the proposed integrated system possesses about 6 times higher water production capacity than the conventional desalination integrated system. Therefore, it has been concluded that the proposed integrated system is a novel water and electricity cogeneration nuclear system with an effective waste heat utilization.

VHTR integrated systems such as the suggested VHTR-FO system tend to have effective advantages, however, it possesses a possibility of tritium migration from the VHTR to the integrated industrial process system. In the case of VHTR-FO system, tritium issue is more critical as the final product of FO system is potable water. Therefore it is crucial to understand and analyze tritium behavior in

the proposed integrated system in terms of safety. In this study, following studies have been conducted in order to understand and analyze tritium behavior in the VHTR-FO system; (1) development of a tritium analysis code, BOTANIC, (2) development of tritium permeation model in the PCHE, (3) acquisition of tritium permeation data at low temperature region.

A code intended for analyzing tritium behavior in the nuclear reactor system has been developed using a chemical process code called gPROMS. The tritium code, named as the Behavior of Tritium Analytic Code, BOTANIC, was developed using the Process Model Library (PML) implemented in the gPROMS code. BOTANIC is capable of several functions; (1) system dynamics calculation, (2) chemical process analysis, (3) tritium analysis in component level, (4) tritium analysis in system level. One of the important features of the code is that it is designed to solve detailed diffusion based permeation model which involves the surface phenomena. The developed BOTANIC code was verified in three step approach using the analytical solutions and the benchmark codes: (1) sub-model verification, (2) component model verification, (3) System model verification.

Tritium permeation model for the Printed Circuit Heat Exchanger (PCHE) is developed for improving analysis accuracy. A semi-empirical PCHE tritium permeation model, which considers the PCHE geometry and the temperature gradient, is developed based on 116,000 numerical calculation results. The geometry of the PCHE was reflected through shape factor which considers the effect of the channel size, horizontal pitch, vertical pitch and offset distance. And the temperature gradient effect was reflected by adopting an effective diffusivity which is a function of average temperature and temperature difference between the channels. The developed PCHE permeation model was found to predict the

permeation rate within  $\pm 20\%$  bound whereas the existing permeation model under predicts the permeation rate when there is no temperature difference between channels and significantly over predicts when temperature difference exists. The developed PCHE tritium permeation model was implemented in the BOTANIC code.

Hydrogen permeability data at low temperature were obtained for the VHTR heat exchanger material, SS316L, through experiment. Furthermore, in previous hydrogen permeation experiments out-gassing has been conducted at 1000 °C before conducting the actual experiment, which would have greatly affected the grain size of the steel specimen as the grain growth is proportional to time and temperature. Increase in grain size decreases the volume of diffusion path in the lower temperature region. Thus, for a more accurate analysis, permeability of tritium isotope at low temperature region was obtained, after defining a reasonable out-gassing condition (400 °C), using Hydrogen Permeation Facility (HYPER). Based on the permeability data, an effective permeability is defined.

Tritium analysis on the suggested VHTR-FO integrated system was conducted using BOTANIC code with the developed PCHE permeation model and effective permeability. As a result, tritium concentration in the water product of VHTR-FO,  $1.6\text{E-}4\ \mu\text{Ci/mL}$  was found to exceed the regulatory limit,  $2\text{E-}5\ \mu\text{Ci/mL}$ . Further sensitivity analysis was conducted on the VHTR-FO system tritium analysis. From the sensitivity analysis it was found that the most effective parameter in tritium migration was tritium permeation in the PHX. Based on the results of the sensitivity analysis, several tritium mitigation approaches have been suggested on PHX including tritium barrier, ceramic heat exchanger, and pre-heat treatment.

## 7.2 Recommendations

Through the present study, the following further studies are suggested:

1. In order to reduce modeling uncertainty in tritium source, the tritium release mechanism has to be studied in more detail. Currently the BOTANIC code, and other existing tritium codes assume a release fraction rather than analyzing the tritium behavior inside the fuel and the core structures.
2. It is reported that the amount of tritium capture and retention on graphite and solid structures are quite large. The BOTANIC code implements very simple Myers model for sorption analysis, whereas the sorption mechanism is known to be very complex. If a more accurate model can be implemented with a more accurate input data, uncertainty from the lack of sorption information can be resolved.
3. The BOTANIC code is verified but not validated. There is no available experimental data that can be used to validate tritium code. Experiments on tritium behaviors in integrated system is essential for code validation. Further work on the validation experiment is strongly suggested.
4. The tritium barrier on the PHX is suggested as one of the tritium mitigation approach. Most of the tritium barriers and the TRFs are grounded on very high temperature experiments. Thus, it is necessary to verify the TRFs of the tritium barriers at low temperature region, the integration temperature region. The development of tritium barrier and the test on the tritium barriers at low temperature have been conducted as seen

in Appendix B, however, due to the limitation of the experiment facility the effect of tritium barriers was not able to see. Further work on the tritium barrier at low temperature can be meaningful.

# Nomenclature

$a_m$	Number of atom in molecule
$a_r$	Release rate coefficient for trapped atoms ( $\text{m s}^{-1}$ )
$a_t$	trapping rate coefficient ( $\text{m s}^{-1}$ )
$A$	Cross-sectional area ( $\text{m}^2$ ), surface area ( $\text{m}^2$ )
$A_w$	Water permeability coefficient ( $\text{L m}^3 \text{ h}^{-1} \text{ bar}^{-1}$ )
$A_s$	Amount of tritium sorbed onto graphite per BET surface area ( $\text{cm}^3 \text{ m}^{-2}$ )
$b$	Temperature dependent constant for grain growth
$b_0$	Constant for grain growth
$B$	Salt permeability coefficient ( $\text{m s}^{-1}$ )
$C_p$	Specific heat at constant pressure ( $\text{J kg}^{-1} \text{K}^{-1}$ )
$C$	Concentration ( $\text{mol m}^{-3}$ )
$C_H$	Annealing factor used in Myers isotherm
$C_n$	Coefficient ( $n=1,2,3\dots$ )
$C_s$	Solute concentration ( $\text{g L}^{-1}$ )
$C_{sorp}$	Sorption conversion coefficient
$d$	Diameter (m), grain size (m)
$d_0$	Initial grain diameter (m)
$D$	Diffusivity, Permeability ( $\text{mol m}^{-1} \text{ s}^{-1} \text{ Pa}^{-0.5}$ )
$D_{mutual}$	Mutual diffusion coefficient ( $\text{m}^2 \text{ s}^{-1}$ )
$D_w$	Bulk diffusion coefficient of the draw solute ( $\text{m}^2 \text{ s}^{-1}$ )
$D_0$	Diffusivity pre-factor, Permeability pre-factor ( $\text{mol m}^{-1} \text{ s}^{-1} \text{ Pa}^{-0.5}$ )
$E_a$	Activation energy ( $\text{J mol}^{-1}$ )
$e_a$	Relative error of mesh

$f$	Fractional supply rate of helium coolant ( $s^{-1}$ )
$f_s$	Fast fluence ( $n\ m^{-2}$ )
$F_s$	Body force vector ( $N\ m^{-3}$ )
$F$	Flowrate ( $kg\ s^{-1}$ )
$Fi$	Fission rate per thermal megawatt (fissions $W^{-1}\ s^{-1}$ )
$Fs$	Factor of safety for GCI analysis
$h$	Specific enthalpy ( $J\ kg^{-1}$ ), horizontal distance (m), convection heat transfer coefficient ( $W\ m^{-2}\ K^{-1}$ )
$H_{vapsteam}$	Enthalpy of vaporization of the steam ( $J\ kg^{-1}$ )
$H_{duty}$	Specific energy requirement for water generation ( $J\ m^{-3}$ )
$J_w$	Water flux ( $L\ m^{-2}\ h^{-1}$ )
$J$	Permeation rate ( $Pa\ s^{-1}$ )
$k$	Thermal conductivity ( $W\ m^{-1}\ K^{-1}$ ), Boltzmann constant ( $m^2\ kg\ s^{-2}\ K^{-1}$ )
$k_w$	Mass transfer coefficient of the feed solution ( $m^2\ s^{-1}$ )
$K_{dm}$	Dissociation coefficient of molecule (M)
$K_{rm}$	Recombination coefficient molecule (M)
$K_s$	Sievert's constant ( $mol\ m^{-3}\ Pa^{-0.5}$ )
$L$	Length, Thickness (m)
$L_R$	Leakage rate ( $kg\ s^{-1}$ )
$M$	Mass (kg)
$MW$	Molecular weight ( $kJ\ kg^{-1}$ )
$M_T$	Total mass holdup (kg)
$n$	Number of moles
$N$	Number of atoms
$o$	Offset distance of PCHE channel (m)

$p$	Order of convergence
$P$	Pressure (Pa), Partial Pressure (Pa)
$P_1$	Pressure of process volume 1 of HYPER facility (Pa)
$P_2$	Pressure of process volume 2 of HYPER facility (Pa)
$\dot{P}$	Time derivative of pressure (Pa s <sup>-1</sup> )
$Q$	Heat input (W), heat source (W m <sup>-3</sup> )
$q_h$	Grain shape parameter
$r$	Grid refinement ratio
$R$	Universal gas constant (J mol <sup>-1</sup> K <sup>-1</sup> ), Permeation rate (mol s <sup>-1</sup> )
$S$	Source term (kg s <sup>-1</sup> ), (J s <sup>-1</sup> )
$S_w$	Structural parameter
$S_0$	Sievert's pre-factor
$S_1$	Shape factor 1
$S_2$	Shape factor 2
$t$	Time (s)
$T$	Temperature (K)
$T_0$	Reference temperature (K)
$u$	Velocity (m s <sup>-1</sup> )
$u_c$	Total uncertainty
$u_r$	Random uncertainty
$u_s$	Systematic uncertainty
$U$	Total internal energy (J)
$v$	Vertical distance between PCHE channel (m)
$V$	Volume (m <sup>3</sup> )
$W$	Power, work (W)

$x$	Mass fraction
$x_{mem}$	Thickness of the support layer (m)
$y$	Mole fraction
$Y$	Average yield per fission (fission <sup>-1</sup> )
$z$	Charge

### Greek Letters

$\beta$	Convection coefficient
$\delta$	Reflection coefficient
$\delta_h$	Grain boundary width (m)
$\varepsilon$	Difference between simulation values of different mesh resolutions
$\phi$	Diffusion coefficient (m <sup>2</sup> s <sup>-1</sup> )
$\varphi$	Porosity
$\varphi_f$	Average fast neutron flux (n/cm <sup>2</sup> /s)
$\varphi_{He}$	Average thermal neutron flux experienced by the total primary helium inventory (n/cm <sup>2</sup> /s)
$\varphi_{th}$	Average thermal neutron flux (n/cm <sup>2</sup> /s)
$\eta$	Efficiency
$\lambda$	Tritium decay constant (s <sup>-1</sup> ).
$\mu$	Dynamic viscosity (Pa s)
$\pi$	Osmotic pressure (atm)
$\pi_D$	Osmotic pressure draw solute (atm)

$\pi_F$	Osmotic pressure of the feed (bar)
$\theta_s$	Graphite BET surface area per mass ( $\text{m}^2 \text{g}^{-1}$ )
$\rho$	Density ( $\text{kg m}^{-3}$ )
$\sigma$	Cross section ( $\text{cm}^2$ )
$\tau$	Tortuosity of the membrane

### Subscripts

<i>B10</i>	Boron 10 isotope
<i>D</i>	Diffusivity, permeability
<i>core</i>	helium in core
<i>eff</i>	Effective
<i>eq_s</i>	Equilibrium sorption capacity
<i>grain</i>	Grain
<i>gb</i>	Grain boundary
<i>He3</i>	Helium 3 isotope
<i>i</i>	Chemical species i
<i>inlet</i>	Inlet
<i>lattice</i>	Lattice
<i>Li6</i>	Lithium 6 isotope
<i>Li7</i>	Lithium 7 isotope
<i>nor</i>	Normalized
<i>outlet</i>	Outlet
<i>overall</i>	Plant overall
<i>PCHE</i>	Printed circuit heat exchanger

<i>PF</i>	Purification system
<i>Plate</i>	Plate, slab
<i>s</i>	Sorption
<i>total</i>	Total primary helium
<i>T</i>	Tritium
<i>t</i>	trap
<i>Ter</i>	Ternary fission

#### Superscripts

+	Cation
-	Anion
<i>e</i>	Empty

## References

Adham, S., Oppenheimer, J., Liu, L., Kumer, M., Dewatering Reverse Osmosis concentrate, Water Reuse Foundation Research Report, 2007

Alsvik, I. and Hagg, M., "Pressure retarded osmosis and forward osmosis membranes: materials and methods," *Polymers*, Vol. 5, pp. 303-327, 2013

American Society of Mechanical Engineers, Test uncertainty ASME PTC 19.1-2013, 2013

Batchelder, G.W., "Process for the Demineralization of Water," US Patent 3,171,799, 1965

Bluetec, Forward osmosis, Retrieved from <http://www.blue-technologies.nl/technologies-forwardosmosis>, 2016

Boo, C., Khalil, Y., Elimelech, M., "Performance evaluation of trimethylamine-carbon dioxide thermolytic draw solution for engineered osmosis," *Journal of Membrane Science*, Vol. 473, pp. 302-309, 2015

Bundela, P. S., "Sustainable development through waste heat recovery," *American Journal of Environmental Sciences*, Vol. 6, pp. 83-89, 2010

Causey et al., "Tritium Barriers and Tritium Diffusion in Fusion Reactors," *Comprehensive Nuclear Materials*, 2012.

- CDW, Ammonia in drinking water, Document for Public Consultation, 2013
- Chang, J. et al., "A Study of a Nuclear Hydrogen Production Demonstration Plant," *Nuclear Engineering Technology*, Vol. 39(2), pp. 111-122, 2007
- Changqi, S. Aiju, W., Qingwang, C., "The behavior of diffusion and permeation of tritium through 316L stainless steel," *Journal of Nuclear Materials*, Vol. 179-181, pp. 322-324, 1991
- Cekli, L., Phuntsho, S., Shon, H. K., Vigneswaran, S., Kandasamy, J., Chanan, A., "A review of draw solutes in forward osmosis process and their use in modern applications," *Desalination and Water Treatment*, Vol. 43, pp. 167-184, 2012
- Cussler, E. L., *Diffusion: mass transfer in fluid systems*, 2nd ed., Cambridge University Press, New York, 1997.
- Dostal, V., Driscoll, M. J., Hejzlar, P., "A supercritical carbon dioxide cycle for next generation nuclear reactors," MIT-ANP-TR-100, 2004
- EPA, "Drinking Water Regulations: Radionuclides," *Federal Register*, Vol. 41, No. 133, pp. 28402–28409, July 9, 1976 (1976b).
- Fachinger, J., Lensa, W. von., Podruhzina, T., "Decontamination of nuclear graphite," *Nuclear Engineering and Design*, Vol. 238, pp. 3086–3091, 2008
- Fairlie, I., *Tritium Hazard Report: Pollution and Radiation Risk from Canadian Nuclear Facilities*, Greenpeace, 2007
- Feher, E. G., "Supercritical Thermodynamic Cycles for External and Internal

Combustion Engines,” Astropower, Inc. Engineering Report, May 1962

Forcey, K. S., Ross, D. K., Simpson, J. C. B., “Hydrogen transport and solubility in 316L and 1.4914 steels for fusion reactor applications,” *Journal of Nuclear Materials*, Vol.160 (2-3), pp. 117-124, 1988

Forcey, K. S., Ross, D. K., Wu, C. H., “The formation of hydrogen permeation barriers on steels by aluminising,” *Journal of Nuclear Material*, Vol. 182, pp 36-51, 1991

Frank, B.S., Desalination of sea water, US Patent 3,670,897, 1972

Gainey, B. W., “A Review of Tritium Behavior in HTGR Systems,” GA A13461, General Atomic Company, 1976

General Atomics, "TRITGO Code Description and User's Guide", GA Project 20128, 2006

Ghiu, S. M. S., Carnahan, R. P., Barger, M., “Permeability of electrolytes through a flat RO membrane in a direct osmosis study,” *Desalination*, Vol. 144, pp. 387–392, 2002

Glasstone, S. and Jordan, W. H. *Nuclear Power and Its Environmental Effects*, American Nuclear Society, La Grange Park, Illinois, USA, 1980

Gray, G. T., McCutcheon, J. R., Elimelech, M., “Internal concentration polarization in forward osmosis: role of membrane orientation,” *Desalination*, Vol. 197, pp. 1-8, 2006

Hart, E.W., "On the role of dislocations in bulk diffusion," *Acta metallurgica*, Vol. 5, pp. 597, 1957

Harvego, E.A. and McKellar, M.G., "Evaluation and optimization of a supercritical carbon dioxide power conversion cycle for nuclear applications," *Proceedings of the 19th International Conference on Nuclear Engineering*, 2011

Hong, L., Chen, Y., Chao, F., Binchen, F., "Experimental study on the adsorption and desorption of tritium in the graphite materials for HTR-PM," *Progress in Nuclear Energy*, Vol. 85, pp. 676-681, 2015

Huang, Z. Y. et al., "Measurement of Deuterium Permeation and Diffusion in Several Stainless Steels," *IAEA Fusion Energy Conference*, Vienna, Austria, 2010

IAEA, "Advanced Power Reactor 1400MWe : APR1400," Status Report 83, 2011

IAEA, "Introduction of Nuclear Desalination: a Guidebook," IAEA-TECDOC-400, 2000

IAEA, "Status of nuclear desalination in IAEA member states," IAEA-TECDOC-1524, 2007

Jo, C. K., Lim, H. S., Noh, J. M., "Preconceptual Designs of the 200 MWth Prism and Pebble-bed Type VHTR Cores," *Proceeding of International Conference on the Physics of Reactors*, Interlaken, Switzerland, 2008

Kato, Y., Nitawaki, T., Muto, Y., "Comparison of Cycle Efficiency, Turbine Efficiency, and Recuperator Heat Transfer Surface Area between Direct Cycles of Carbon Dioxide and Helium", *1st International Topical Meeting on High*

*Temperature Reactor Technology (HTR)*, Petten, The Netherlands, April, 2002

Kim, E. and Oh, C., “Study on the Tritium Behaviors in the VHTR System. Part 2: Analyses on the Tritium Behavior in the VHTR/HTSE System,” *Nuclear Engineering and Design*, Vol. 240(7), pp. 1768-1778, 2010

Kim, I. and No, H., “Physical model development and optimal design of PCHE for intermediate heat exchangers in HTGRs,” *Nuclear Engineering and Design*, Vol. 243, pp. 243–250, 2012,

Kim, I., No, H., Lee, J., Jeon, B., “Thermal hydraulic performance analysis of the printed circuit heat exchanger using a helium test facility and CFD simulations,” *Nuclear Engineering and Design*, Vol. 239, pp. 2399–2408, 2009

Kim, T., Kang, J. H., Yang, S. J., Sung, S. J., Kim, Y. S., Park, C. R., “Facile preparation of reduced graphene oxide- based gas barrier films for organic photovoltaic devices,” *Energy & Environmental Science*, Vol. 7, pp. 3403-3411, 2014

Kishimoto, N., Tanabe, T., Suzuki, T., Yoshida, H., “Hydrogen diffusion and solution at high temperatures in 316L stainless steel and nickel base heat resistant alloys,” *Journal of Nuclear Materials*, Vol. 127, pp. 1-9, 1985

Kodochigov, N. et al., “Neutronic features of the GT-MHR reactor,” *Nuclear Engineering and Design*, Vol. 222, pp. 161-171, 2003

Lay, W., Zhang, J., Fane, A., “Factors affecting flux performance of forward osmosis systems,” *Journal of Membrane Science*, Vol. 394-395, pp. 151-168,

2012

Lee, S. K. and Noh, S. J., "Study on experimental system for hydrogen permeation in thin-solid materials for fusion plasma research," *Current applied physics*, Vol. 11 (5), pp. 99-102, 2011

Longhurst, G. R., "TMAP7 User Manual," INEEL/EXT-04-02352, 2004

Louat. N. P., "On the theory of normal grain growth," *Acta metallurgica*, Vol. 22(6), pp. 721-724

McCutcheon, J. R. and Elimelech, M., "Modeling Water Flux in Forward Osmosis: Implications for Improved Membrane Design," *AIChE Journal*, Vol. 53(7), pp. 1736-1744, 2007

McCutcheon, J. R., McGinnis, R. L., Elimelech, M., "A novel ammonia-carbon dioxide forward (direct) osmosis desalination process," *Desalination*, Vol. 174, pp. 1-11, 2005

McGinnis, R. L., Elimelech, M., "Energy requirements of ammonia-carbon dioxide forward osmosis desalination," *Desalination*, Vol. 207, pp. 370-382, 2007

Morin, O. J., "Design and operating comparison of MSF and MED systems," *Desalination*, Vol. 93, pp. 69-109, 1993

Najjar, Y. S. H. and Akhurt, M., "Combined cycles with gas turbine engines," *Heat Recovery Systems & CHP*, Vol. 14, pp. 93-103, 1994

Nakamichi, M., Kawamura, H., Teratani, T., "Characterization of Chemical

Densified Coatings as Tritium Permeation Barrier,” *Journal of Nuclear Science and Technology*, Vol. 38 (11), pp 1007-1013, 2001

NG, H. Y., Tang, W., Wong, W. S., “Performance of forward (direct) osmosis process: membrane structure and transport phenomenon,” *Environmental Science and Technology*, Vol. 40(7), pp. 2408-2413, 2006

Oh, C. and Kim, E., “Development and verification of tritium analyses code for a very high temperature reactor,” INL/EXT-09016465, 2009

Ohashi, H. and Sherman, S., “Tritium movement and accumulation in the NGNP system interface and hydrogen plant,” INL/EXT-07-12746, 2007

OLI Systems, OLI Analyzer studio, 2009

Park, M. and Kim, E. “Thermodynamic evaluation on the integrated system of VHTR and forward osmosis desalination process,” *Desalination*, Vol. 337, pp. 117-126, 2014

Park, M., Kim, B., Kim, E., “Development of semi-empirical model for tritium permeation under non-uniform temperature distribution at heat exchanger tube wall,” *Annals of Nuclear Engineering*, Vol. 75, pp. 413-420, 2015

Park, S., Ahn, M., Cho, S., Park, Y., Kim, C., Lee, Y., Ku, D., “Construction of HYPER facility for hydrogen permeation experiments,” APFA, 2013

Process Systems Enterprise Limited, Model developer guide, 2012

Redmond, J. P. and Walker, P. L., “Hydrogen sorption on graphite at elevated

temperatures,” *Journal of Physical Chemistry*, Vol. 64 (9), pp. 1093–1099, 1960

Roache, P. J., “Quantification of uncertainty in computational fluid dynamics,” *Annal Review of Fluid Mechanics*, Vol. 29, pp.123-160, 1997

Shaffer, D. L. Werber, J. R., Jaramillo, H., Lin, S., Elimelech, M., “Forward osmosis: where are we now?,” *Desalination*, Vol. 356, pp. 271-284, 2015

Shanghai Stal Precision Stainless Steel Co. LTD, Types 316 (S31600), 316L (S31603), 317 (S31700), 317L (S31703), Retrieved from <http://www.stal.com.cn/en/main.asp>, Accessed December 2015

Shiraishi, T., Nishikawa, M., Yamaguchi, T., Kenmotsu, K., “Permeation of multi-component hydrogen isotope through austenitic stainless steel,” *Journal of Nuclear Materials*, Vol. 273 (1), pp. 60-65, 1999

Steven, R. S. and Thad, M. A., “Tritium barrier materials and separation systems for the NGNP,” WSRC-STI-2008-00358, 2008

Street, H., 94 % Alumina properties, Retrieved from <http://accuratus.com/>, 2016

Tamura, M., Noma, M., Yamashita, M., “Characteristic change of hydrogen permeation in stainless steel plate by BN coating,” *Surface & Coating Technology*, Vol. 260, pp. 148-154, 2014

UNISIM design, Simulation Basis Guide, Honeywell, 2010

UNISIM design, User guide, Honeywell, 2010

UNISIM design, User guide, Honeywell, 2010

Vacuum Process Engineering, Diffusion bonded microchannel heat exchanger,  
Retrieved from <http://www.vpei.com/> 2016

Van't Hoff, J. H., "Die Rolle der osmotischen Druckes in der Analogie Zwischen  
Losungen and Gasen," *Z. Phys. Chem*, Vol. 1, pp. 481-508, 1887

WHO, "Guidelines for drinking-water quality," 2011

Wichner, R. P. and Dyer, F. F., "Distribution and Transport of Tritium in the Peach  
Bottom HTGR," ORNL 5497, August Oak Ridge National Laboratory, 1979

Wilson, A. D. and Stewart, F. F., "Deriving osmotic pressures of draw solutes used  
in osmotically driven membrane process," *Journal of Membrane Science*, Vol. 431,  
pp. 205-211, 2013

Yao, Z., Hao, J., Zhou, C., Shan, C., Yu, J., "The permeation of tritium through  
316L stainless steel with multiple coatings," *Journal of Nuclear Materials*, Vol.  
283-287, pp 1287-1291, 2000

# Appendix A

## BOTANIC Interface

The BOTANIC on gPROMS platform provides the gPROMS GUI as shown Figure A.1. On the left hand side the BOTANIC palette consisting of the component models of BOTANIC code. The component models in the BOTANIC code are listed in Table A.1.

The necessary components can be dragged and dropped on the flowsheet model. Once the flowsheet is constructed and the inputs are given for each component, the calculation can be conducted.

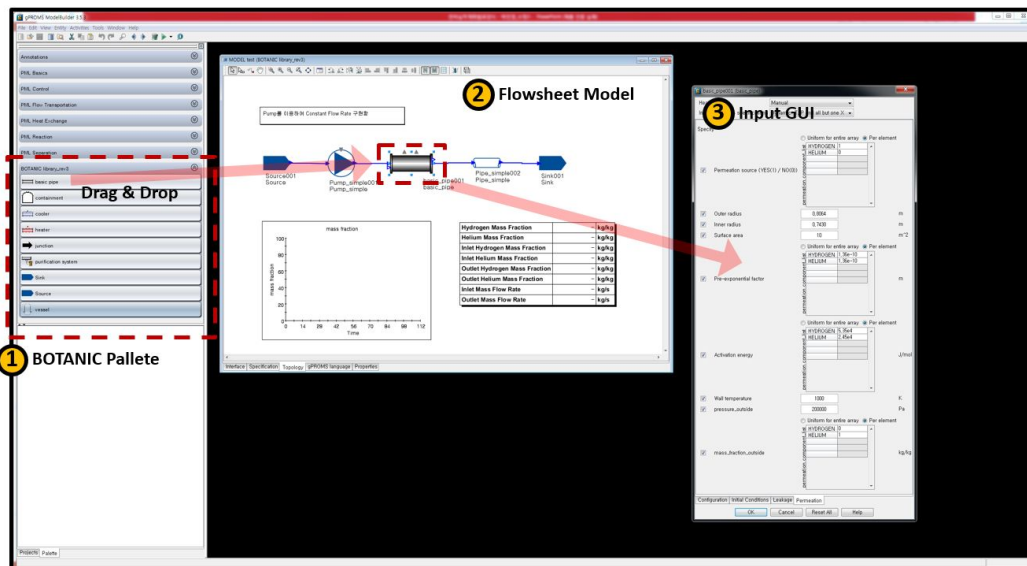
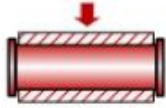
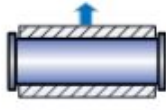
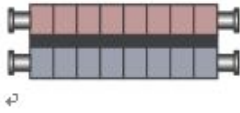


Figure A. 1 BOTANIC code interface

Table A. 1 Component models in BOTANIC code

Component model <sup>↵</sup>	Icon <sup>↵</sup>	Governing equation and model <sup>↵</sup>	Component type <sup>↵</sup>
Pipe <sup>↵</sup>		Component Mass Balance (+ Mass Source) <sup>↵</sup> Energy Balance <sup>↵</sup> Leakage, Permeation, <u>Multiflash</u> (property) <sup>↵</sup>	Lumped <sup>↵</sup>
Heater <sup>↵</sup>		Component Mass Balance (+ Mass Source) <sup>↵</sup> Energy Balance (+ Energy Source) <sup>↵</sup> Leakage, Permeation, <u>Multilash</u> (property) <sup>↵</sup>	Lumped <sup>↵</sup>
Cooler <sup>↵</sup>		Component Mass Balance (+ Mass Source) <sup>↵</sup> Energy Balance (+ Energy Sink) <sup>↵</sup> Leakage, Permeation, <u>Multiflash</u> (property) <sup>↵</sup>	Lumped <sup>↵</sup>
Reactor <sup>↵</sup>		Component Mass Balance (+ Mass Source) <sup>↵</sup> Energy Balance (+ Energy Source) <sup>↵</sup> Tritium Birth, <u>Chemi-sorption</u> <sup>↵</sup> Leakage, Permeation, <u>Multiflash</u> (property) <sup>↵</sup>	Lumped, Distributed <sup>↵</sup>
Vessel <sup>↵</sup>		Component Mass Balance (+ Mass Source) <sup>↵</sup> Energy Balance <sup>↵</sup> Leakage, Permeation, <u>Multiflash</u> (property) <sup>↵</sup>	Lumped <sup>↵</sup>
Heat exchanger <sup>↵</sup>		Component Mass Balance (+ Mass Source) <sup>↵</sup> Energy Balance (+ Energy Source) <sup>↵</sup> Leakage, Purification, <u>Multilash</u> (property) <sup>↵</sup>	Lumped <sup>↵</sup>
Purification system <sup>↵</sup>		Component Mass Balance (+ Mass Source) <sup>↵</sup> Energy Balance (+ Energy Source) <sup>↵</sup> Purification, <u>Multiflash</u> (property) <sup>↵</sup>	Lumped <sup>↵</sup>
Containment <sup>↵</sup>		Component Mass Balance (+ Mass Source) <sup>↵</sup> Energy Balance <sup>↵</sup> Leakage, Permeation, <u>Multiflash</u> (property) <sup>↵</sup>	Lumped <sup>↵</sup>

## Appendix B

### Tritium Barrier

This section presents the experimental investigation on the tritium barrier; graphene and erbium oxide using spin-coating.

Graphene is one of the promising gas barrier material. It is a sheet of carbon atoms arranged in honeycomb lattice. The geometric pore of graphene and the hydrogen diameter are similar, 0.06 nm, meaning that if graphene layer is coated without defect, hydrogen nor any other gas atoms can permeate through graphene. Reduced graphene oxide (rGO) is basically layers of graphene which is produced by reducing graphene oxide. rGO is favored for relatively easy production procedure; spin-coating. Layers of rGO is produced using spin-coating at optimized conditions obtained in previous studies (Kim, 2014). Coating procedure is as follows. The coated surface morphology and the side morphology can be observed in Figure A.2 and A.3. As depicted in the figures the graphene on specimen show no defect at 1E4 magnified view.

1. GO solutions prepared with modified Hummer's method using flake graphite.
2. Pre-heat treatment conducted at 150 for 30 minutes.
3. (a) GO solutions coated on the S316 polished specimen at 2000 rpm.
4. (b) Dried on hot plate (50 C) for 30 minutes
5. (a) and (b) repeated for 15 times
6. Coated specimen heated to 250 C at rate of 0.1 C per minute and treated

for 30 minutes.

Erbium oxide is one of the most promising candidate for tritium barrier material which is suggested recently. It is known for its good thermo-mechanical stability. It was reported that 1  $\mu\text{m}$  of erbium oxide coating results in TRF of 1000. Erbium oxide is typically produced through sputtering or evaporation deposition methods. These procedures have limitations in area, thickness, expensive, toxic byproducts, etc. Thus, in this study, the erbium coating on S316 has been attempted using spin-coating method for flexibility and cost reduction. The erbium oxide solution is produced using sol-gel method as seen in Figure A.4. Optimization on coating conditions are conducted as can be seen in Figure A.5 and Table A.2. As seen in Figure A.6 the surface morphology of erbium oxide coating show significant enhancement after optimization. The XRD patterns of the erbium coating has been obtained and as shown in the figure the erbium oxide peaks can be observed after heat treatment.

Permeation experiment with the coated specimen has been conducted on HYPER facility. However as the test section is designed to insert disk type specimen between glands, during the insertion specimen is strongly pushed by the gland on the point of contact. This causes defects of the coating and defects makes coating effect invalid. It was found that the permeability of the coated specimen are identical to the non-coated specimen. Thus, in order to observe the coating effect of the rGO and erbium oxide at low temperatures, the test section and the specimen type must be improved.

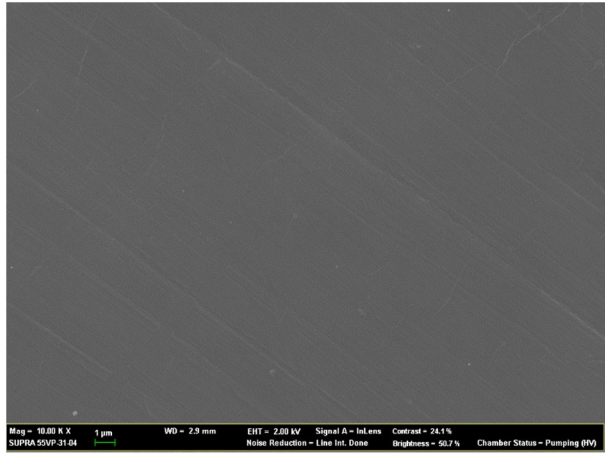


Figure A. 2 rGO surface morphology, SEM image

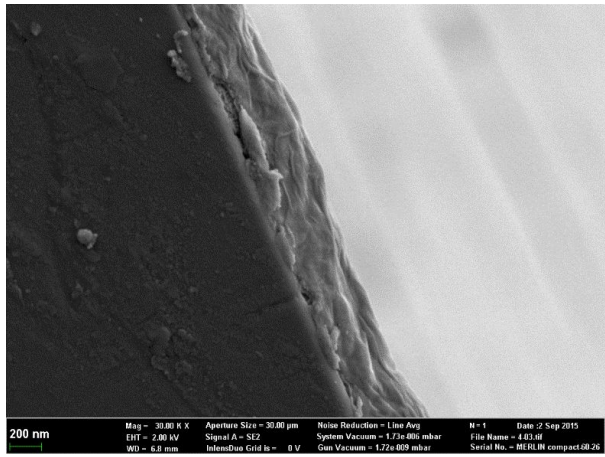


Figure A. 3 rGO side morphology, SEM image

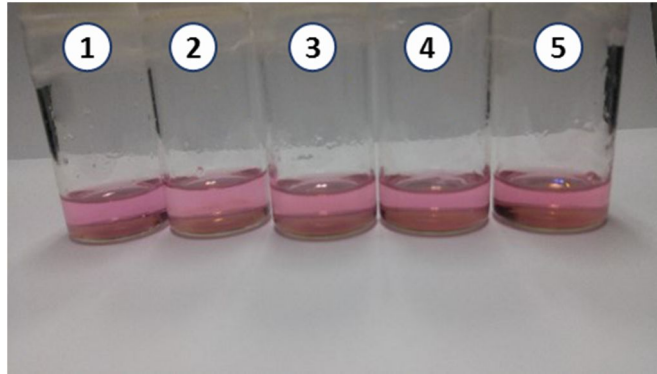


Figure A. 4 Erbium oxide solutions

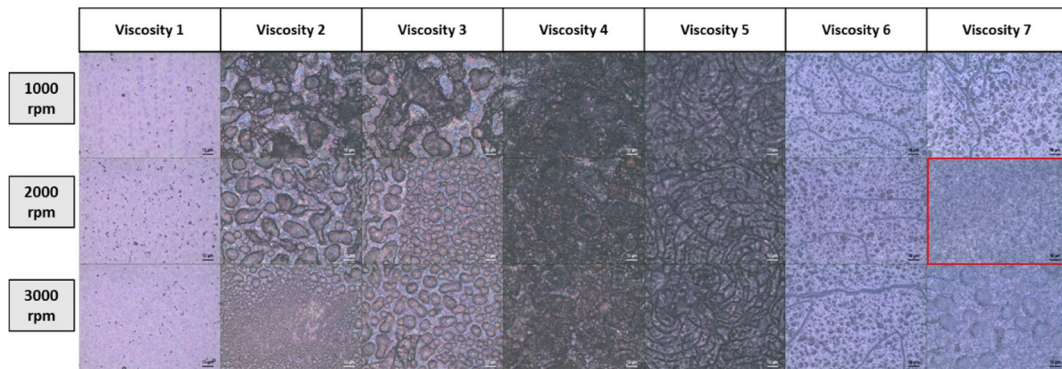


Figure A. 5 Optimization on erbium oxide

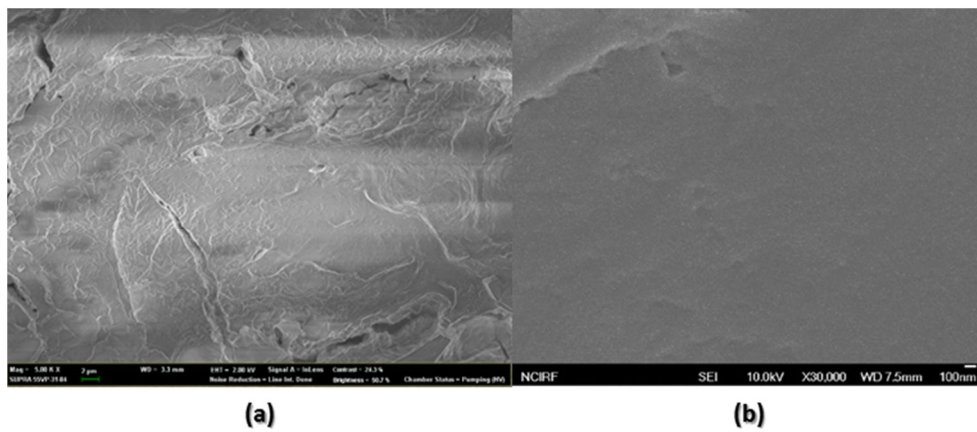


Figure A. 6 Surface morphology of erbium oxide (a) before optimization and (b) after optimization

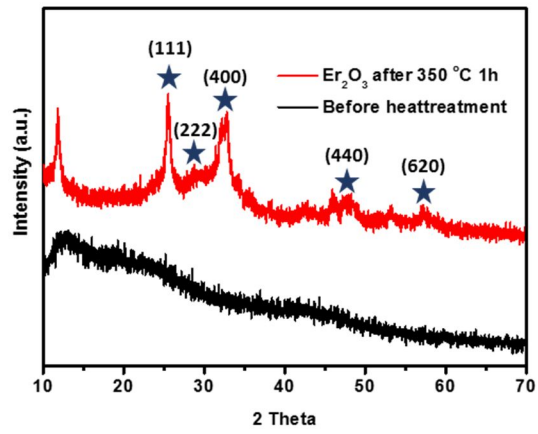


Figure A. 7 XRD pattern of erbium oxide coating

Table A. 2 Optimization solution compositions

	Viscosity 1	Viscosity 2	Viscosity 3	Viscosity 4	Viscosity 5	Viscosity 6	Viscosity 7
<b>Er precursor (g)</b>	3.5						
<b>Collodion (mL)</b>	2	4	6	8	10	12	14
<b>Ethanol (mL)</b>	14	12	10	8	6	4	2

## 국문 초록

고온가스로는 높은 효율, 안정성, 다양한 활용성을 확보한 대표적인 4세대 원자로이며 가스터빈과 통합될 경우 높은 전기생산 효율뿐만 아니라 양질의 폐열 또한 확보할 수 있다. 원자력 발전소의 폐열은 전체 핵분열 에너지 생성량의 60% 이상을 차지하고 있으며 환경에 주는 영향 또한 크기 때문에 이에 대한 효과적인 관리 및 활용은 원자력 에너지의 경쟁력을 확보하는데 크게 기여할 수 있다. 본 연구에서는 이에 대한 방안으로 고온가스로의 폐열을 이용하여 정삼투담수화 시스템과 통합 할 수 있는 개념을 제안하고 해석을 수행하였다. 그 결과 제안한 고온가스로-정삼투담수화 개념은 90% 이상의 에너지 이용율과 기존의 원자력 담수화 시스템에 비하여 5배 이상의 높은 담수 생산능력을 갖출 수 있을 것으로 평가되었다.

삼중수소는 핵분열반응을 통해서 생성되는 방사능 물질로 고온에서 금속을 쉽게 투과하는 성질이 있기 때문에 고온가스로, 용융염원자로 등에서 중요하게 고려하고 있는 수소 동위원소이다. 특히 고온가스로의 경우 노심에서 생산된 삼중수소는 고온의 열교환기를 투과해 2차측 및 고온가스로와 연계된 수소생산 시스템과 공정 시스템으로 쉽게 침투할 가능성이 있다. 또한 본 연구에서 제안한 바와 같이 담수화 시스템과 통합할 경우에도 담수화 시설 내로 침투할 가능성이 높다. 특히 담수화 시스템의 경우 최종 생산물이 음용수이기 때문에 안전 및 인허가에 있어 더 중요하게 고려하고 정확하게 예측 및 평가되어야 한다. 본

연구에서는 고온가스로-정심투 담수화 시스템의 삼중수소 거동을 정확하게 해석 및 예측하기 위해 (1) 삼중수소 해석코드 개발, (2) PCHE 삼중수소 침투모델 개발 및 (3) 실험을 통한 저온 삼중수소 침투율 측정을 수행하였다.

본 연구에서 개발한 삼중수소 해석코드인 BOTANIC 코드는 gPROMS 상용 화학공정해석코드 기반으로 개발되었다. BOTANIC은 삼중수소를 포함한 유체 및 화학 종들의 질량, 에너지 방정식을 풀도록 개발이 되었으며 삼중수소 생성, 누설, 정화, 침투와 관련된 모델을 포함하고 고체내의 삼중수소 확산, 트랩 및 표면에서의 평형/비평형 흡착거동 모델을 포함하여 다양한 삼중수소의 거동을 다룰 수 있도록 하였다. 이를 통해서 삼중수소 거동해석, 시스템 동적 거동해석 및 화학공정 해석을 동시에 수행할 수 있도록 하였다. BOTANIC 코드는 검증은 해석해 및 벤치마크 코드와의 비교를 통해 수행되었다.

본 연구에서는 고온가스로에서 채택하고 있는 PCHE 열교환기를 통한 정확한 삼중수소 침투율 예측을 위해서 수치해석결과를 바탕으로 해석모델을 개발하였다. PCHE의 복잡한 유로 형상을 반영하기 위해서 형상계수 개념을 도입하였으며 삼중수소 침투경로를 2개로 분리하여 각각의 경로에 대하여 형상계수 모델을 개발 하였다. 또한 PCHE 내의 온도분포의 영향을 반영하기 위해서 유효 확산계수 및 유효 온도에 대한 개념을 이용하였다. 이를 통해서 개발한 PCHE 삼중수소 침투 모델은 수치해석을 통해서 계산한 침투율을 20% 이내로 잘 예측하는 것으로 확인되었다.

기존의 삼중수소 침투에 대한 연구는 대부분 고온영역에서 수행이 되었다. 하지만 저온에서 열교환을 하는 담수화시스템의 특성상 저온영역에서의 침투데이터가 요구 되었으며 이에 본 연구에서는 국가핵융합연구소(NFRI)의 수소침투실험장치(HYPER) 를 이용하여 저온 영역의 수소 침투실험을 수행하고 침투율을 측정하였다. 그 결과 약 350°C 부근에서 삼중수소 매커니즘의 변화를 관찰할 수 있었으며 저온에 350 °C 부근까지는 grain boundary diffusion에 의해 350 °C 이상에서는 lattice diffusion에 의해서 지배를 받는 것으로 확인할 수 있었다. 또한 실험으로 측정된 침투율을 기반으로 lattice diffusion과 grain boundary diffusion 의 영향을 모두 고려할 수 있는 유효 침투율 상관식을 개발하였다.

최종적으로 본 연구에서는 개발한 삼중수소 해석코드, 모델, 침투데이터를 이용하여 고온가스-정삼투담수화 시스템 내의 삼중수소 거동을 분석 및 평가해 보았다. 그 결과 본 연구에서 가정된 기본 시나리오 하에서 고온가스-정삼투담수화 시스템에서 생산된 물의 삼중수소 농도가 규제치보다 높을 가능성이 큰 것으로 계산되었다. 본 연구에서는 삼중수소의 농도에 영향을 주는 인자를 파악하기 위해 다양한 파라미터들에 대한 민감도 분석을 수행하였으며 그 결과 공정열교환기(PHX)에서의 삼중수소 침투가 매우 중요한 요인으로 평가 되었다. 이를 바탕으로 공정열교환기에서의 삼중수소 침투를 완화할 수 있는 방안들을 제안하고 평가를 수행하였으며 (1)삼중수소 방지막 (2)세라믹 열교환기 사용 (3)열교환기 예열처리가 삼중수소

완화를 위한 효과적인 방안인 것으로 확인할 수 있었다.

### 주요어

고온가스로, 가스터빈, 정삼투 담수화, 삼중수소, PCHE 열교환기,  
삼중수소 완화, 침투, 침투율

학번: 2011-30992